Revolutionizing MTDC Networks:

Unlocking the Power of FPGA-based MMCs with Grid Forming Control on RSCAD through Model Predictive Control

Rohan R. Kamat Tarcar, 5478227

TU Delft

IEPG Intelligent Electrical Power Grids

Revolutionizing MTDC Networks:

Unlocking the Power of FPGA-based MMCs with Grid Forming Control on RSCAD through Model Predictive Control

by

Rohan R. Kamat Tarcar, 5478227

to obtain the degree of Master of Science
at the Delft University of Technology,
to be defended publicly on Tuesday July 11 , 2023 at 10:00 AM.

Daily Supervisor:	Dr. Ir Aleksandra Lekić
Thesis Advisor:	Prof. Dr. Marjan Popov
PhD Supervisor:	Ir. Ajay Shetgaonkar
External Committee Member:	Dr. Ir. Mohamad Ghaffarian Niasar
Thesis Duration:	December 2022 - July 2023
Faculty:	Faculty of EEMCS, Delft

This thesis is confidential and cannot be made public until August 20, 2024.

An electronic version of this thesis is available at `http://repository.tudelft.nl/`.

Cover: HVDC Light valve hall (ABB, 2016-03-10)
Style: TU Delft Report Style, with modifications by Daan Zwaneveld

TU Delft

Preface

"The only true wisdom is in knowing you know nothing."

-Socrates

Acknowledgements

I would like to express my sincere gratitude and appreciation to all those who have supported and guided me throughout the process of completing this thesis. Their invaluable contributions, encouragement, and unwavering belief in my abilities have been instrumental in shaping this work.
First and foremost, I am deeply indebted to my two professors, Prof. Aleksandra Lekic and Prof. Marjan Popov, for their remarkable expertise and insightful guidance. Their constant encouragement, valuable feedback, and constructive criticism have significantly enriched this thesis. I am truly grateful for the time and effort they invested in nurturing my intellectual growth. I owe a special debt of gratitude to my PhD supervisor, Ir. Ajay Shetgaonkar. His unwavering support, patience, and mentorship have been the cornerstone of my academic journey. Their keen eye for detail and ability to push me beyond my limits have transformed me into a better researcher. I am honoured to have had the privilege to work under their guidance. I would also like to extend my heartfelt appreciation to my friends, whose support kept me going. Your words of encouragement and willingness to lend a helping hand were crucial in maintaining my enthusiasm and determination.
I am eternally grateful to my beloved family for your unconditional love and unwavering support. Your belief in me and your constant encouragement gave me the strength to pursue my dreams. Your patience and understanding throughout this journey will forever be treasured.
I would also like to express my gratitude to the individuals who provided valuable insights, feedback, and assistance during the course of this research. Whether through interviews, surveys, or consultations, their contributions have enriched this study and broadened my perspective. Their willingness to share their expertise and experiences is sincerely appreciated. Completing this thesis would not have been possible without the support and guidance of each and every one of you. Your contributions, both big and small, have impacted my life and academic journey.
Thank you all from the bottom of my heart.

Rohan Kamat Tarcar, July 2023

Abstract

Integrating renewable offshore wind generation into global power grids is a critical issue in the energy industry. Modular Multilevel Converter (MMC)-based High Voltage Direct Current (HVDC) grids are the most effective and promising technical solution for the new offshore wind energy power system connections. These grids offer scalability, controllability, and reliability advantages, but their stable and compliant operation requires implementing MMC control strategies and controllers. This thesis investigates the intricacies of HVDC technologies, focusing on MMC control strategies and controllers. The research explores grid following and grid forming converter control strategies, essential for ensuring stable and compliant operation of MMC-based HVDC grids.

The research elaborates on the Model Predictive Control (MPC), which is a promising control strategy for MMC-based HVDC grids. The MPC controller makes the control strategies respond faster, emphasizing constraints and cost functions. Furthermore, a comparative analysis of Proportional Integral (PI)-based and MPC-based controllers is conducted across various scenarios, highlighting the advantages of MPC-based controllers over PI-based controllers regarding response time and stability.

Lastly, a large stability analysis is conducted using the direct Lyapunov method to evaluate the effectiveness of the control strategies and controllers during transient events. This analysis provides insights into the stability and performance of MMC-based HVDC grids under different operating conditions and disturbances.

This thesis illustrates the capabilities of grid-forming control strategy through Model Predictive controllers for FPGA-based MMC-MTDC networks on RSCAD/RTDS®. The outcomes of this thesis contribute to advancing HVDC technologies and control strategies, with implications for enhancing the stability and efficiency of MMC-based HVDC grids. The findings of this thesis have significant potential in the energy industry, particularly in integrating renewable offshore wind generation into global power grids.

Contents

List of Figures

List of Tables

Nomenclature

Abbreviations

Abbreviation	Definition
PCC	point of Common Coupling
IPC	Integrated Power and Control
OWF	Offshore Wind Farms
MMC	Multi-level Modular Converters
F	Farads
H	Henries
GVA/MVA	Giga/Mega Volt-Ampere
kV	kilo volts
KA	kilo Amperes
HVDC	High Voltage Direct Current
HVAC	High Voltage Alternating Current
OHL	Over Head Line
m/s	metres per second
$Xp - yw$	x poles- y winding (winding configuration in the case of a transformer)
$Y - D$	star Delta configuration
PLL	Phase Locked Loop
X	reactance
R	resistance
SCR	Short Circuit Ratio
XBR	X/R ratio
pu	per unit
VSC	Voltage Source Converter
EMT	Electro-Magntic Transient
MTDC	Multi Terminal Direct Current
IGBT	insulated Gate Bi-polar transistor
TSO	Transmission System Operator
ENTSO-E	European Network of Transmission System Operators for Electricity
VARC	VSC Assisted Resonant Current
PMSM	Permanent Magnet Synchronous Machine
GFM	Grid Forming control strategy
GFL	Grid Following Control strategy
CCSC	Circulating Current Suppression Control
EMTP	Electromagnetic Transients Program
VSM	Virtual Synchronous Machine
PLL	Phase Locked Loop
SRRF	Synchronous Rotating Reference Frame
FPGA	Field Programmable Gate Arrays

1 Introduction

1.1. Background and motivation

In recent years, there has been a significant increase in the consumption of electrical energy, which has been primarily produced using non-renewable resources such as fossil fuels. Rapid electrification has caused a significant increase in global warming due to the carbon dioxide produced by burning these fuels. As a result, many countries have decided to switch to greener energy alternatives to reduce their carbon footprint and mitigate the effects of climate change.
Wind and solar energy are the most commonly used and relatively easy to harness among green energy resources. In Europe, copious amounts of renewable energy are available in remote locations, particularly offshore or near the sea. However, the transmission of enormous quantities of electric power via underground cables using Alternating Current (AC) is technically and economically impossible due to the capacitance of the cable systems. For this reason, High Voltage Direct Current (HVDC) transmission schemes are now becoming increasingly pertinent [1].
ABB first developed HVDC transmission networks in Sweden in the 1950s, with the development of thyristors with high rating capabilities. The technology was mainly used for bulk power transmission over long distances, undersea (cable) connections, and the interconnection of non-synchronous networks. Later, it was used further due to the development of transistor-based components (IGBT) for HVDC, which started in the 90s. Since then, the HVDC technology has continued to grow remarkably.
With the growing integration of renewable energy and increasing demand for long-distance power systems interconnections, HVDC technology has become a significant driver for developing future clean and smart grids as part of regional and transborder interconnections. The use of HVDC transmission technology lends itself perfectly to long cable interconnections, whether underground or submarine since there is no distance limitation, contrary to AC cables, which have high charging currents that need reactive power compensation. The technology is also critical for interconnection non-synchronous networks, such as asynchronous AC networks in France and the UK, 50 to 60 Hz back-to-back as Japan, or Argentina - Brazil [8]. The development of HVDC technology has also made it possible to transmit bulk power over long distances and undersea cable connections.
Moreover, the development of transistor-based components for HVDC has made it possible to transmit renewable energy from remote locations to urban centers. The technology is also useful in transmitting renewable energy from one country to another. For instance, the North Sea Grid Connection Project will connect the offshore wind farms in the North Sea to the onshore grid in Germany, the Netherlands, and Denmark [1].

Multiple AC sub-grids can be interconnected using HVDC transmission to, e.g., integrate the offshore wind, exchange power between different networks to increase reliability and flexibility, and electric transport power over long distances or through submarine cables. Moreover, one may choose to segment existing AC systems into different AC and DC sub-grids and leverage the additional controllability of HVDC transmission to prevent disturbances and faults from spreading across the grid of grids. Integrated Power and Controls (IPCs) ensure a stable power exchange between the interconnected sub-systems and overall system stability whenever a contingency occurs. In particular, IPCs can prevent faults and disturbances from spreading and provide frequency and voltage support from neighboring sub-systems [23].

HVDC grids are the most effective and promising technical solution for connecting renewable onshore and offshore wind generation globally. Many Offshore Wind Farms (OWFs) use HVDC technology, including the BorWin, DolWin, HelWin, and Dogger Bank projects installed in the German

sector of the North Seas, as well as in Dutch, Belgian, German, and United Kingdom (UK) waters [18].

1.2. VSC-based MMCs for HVDC applications

The most common and oldest technology in HVDC is the Line Commutated Converter (LCC) technology. Still, the Voltage Source Converter (VSC) technology is now well-proven in HVDC. It is, in many aspects, complementary to the older structures (mainly the fact that in LCC, the flow of current is unidirectional, and in VSC, it is bidirectional [71]). There are many topologies for the VSC, but three of them are the most widely studied: 2-level, 3-level (e.g., Neutral Point Clamped (NPC) or Flying Capacitor), and Multilevel VSC. The 2-level and 3-level VSC has a high switching frequency (1–2 kHz) for obtaining a low harmonic distortion, leading to higher switching losses according to [71]. VSCs are critical components in HVDC systems, specifically designed for efficient power transmission over long distances. Unlike traditional technologies, VSCs offer independent control of active and reactive power, enabling better grid integration and stability. Using insulated-gate bipolar transistors (IGBTs), VSCs provide smoother power flow, reduced harmonics, and improved fault ride-through capabilities. Their modular and scalable design makes them ideal for integrating renewable energy sources like offshore wind farms. While 2-level and 3-level VSCs have a high switching frequency, resulting in higher switching losses and costs for grid operators, a new Multilevel VSC technology, Modular Multilevel Converters (MMC), has been developed to address these issues. MMCs can work with lower switching frequencies while achieving better harmonic performance than 2-level- and 3-level VSCs. These advancements are helping to improve efficiency and reduce costs for grid operators, as noted in [18]. VSC-based HVDC systems are crucial for reliable and efficient power transmission, ensuring a more sustainable energy future.

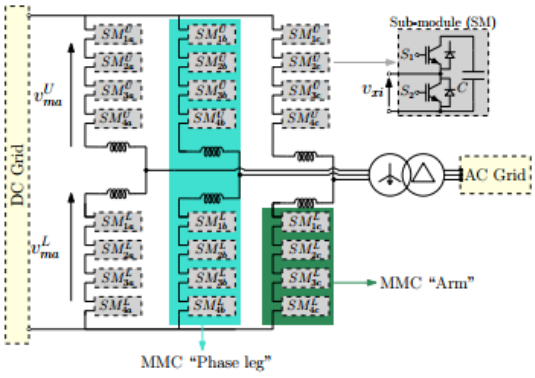

Figure 1.1: MMC: topology [18]

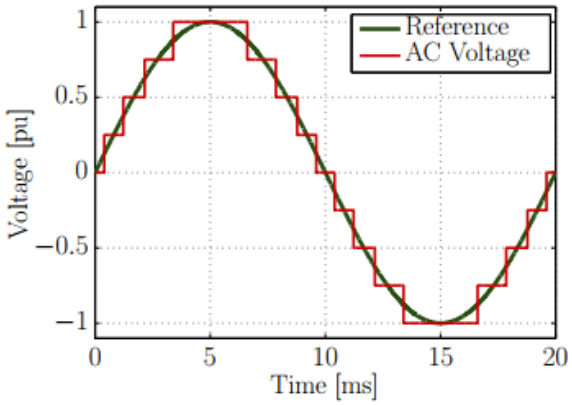

Figure 1.2: MMC: AC voltage waveform [18]

The three-phase Modular Multilevel Converter (MMC) topology, shown in Fig. 1.1, comprises three-phase legs, each consisting of an upper and lower arm. The arms include a stack of Sub-Modules (SMs) with different topologies such as Half-Bridge (HB), Full-bridge, or other topologies. This thesis uses the Half-Bridge topology due to the reduced number of semiconductor devices in the converter and as a more mature, as illustrated in the upper-right corner of Fig. 1.1. Each arm has a series inductance that filters the arm currents and limits inrush currents in case of faults. Unlike the 2-level VSC, there is no capacitor directly connected to the DC bus in the MMC. Instead, each SM has a smaller capacitor inserted or bypassed in the circuit to form the desired voltages, as in Fig.1.2. However, one of the main drawbacks of the MMC is the high complexity of the control system, which requires dedicated controllers to balance the voltage on the submodule's capacitors while ensuring that the output voltages are as expected from the current controllers. Additionally, many currents and voltages inside the converters must be monitored to prevent any possible misbehavior [18].

1.2.1. MMC and network topology

The MMC can be modularized and is highly scalable. It offers flexibility in changing the voltage level of the application by increasing or decreasing the number of series SMs. However, due to its unique

topological structure, the MMC is prone to issues such as unbalanced capacitor voltage and inter-phase circulating current, as noted in [37].
There are multiple configurations in which MMCs can be utilized in an HVDC network converter station. Among these configurations, the two main ones are the monopolar and bipolar configurations. The monopolar HVDC MMC configuration has a return path either through the ground or the sea [78]. Depending on the grounding method and configuration, it can be symmetrical or asymmetrical. This configuration is primarily used for power transmission using cables as it can save the cost of laying one cable. When ground resistance is too high, a metallic return path is preferred instead of using the ground.
The bipolar HVDC MMC configuration consists of two poles, one with a positive polarity and the other with a negative polarity, with their neutral points grounded. During steady-state operation, the current flowing in each pole is equal, and no current flows in the grounded return. Each pole can be operated separately, and if one of the poles malfunctions, the other pole can transmit power by itself with the ground return [52].
Numerous HVDC transmission links based on the point-to-point (P2P) MMC topology have been built or planned in Europe in recent years. Although the P2P topology is the simplest HVDC network, a significant disadvantage is that adding new terminals to the existing network is impossible without constructing a new network. To meet the goals of the European Union (EU), a proposed concept in European research projects is the Mesh Offshore Grid (MOG), as referenced in [56].

1.3. MMC control strategies

In HVDC grids, power flows are determined in advance based on supply and demand, and deviations from the schedule must be regulated according to predefined rules in real-time [55]. Transmission System Operators (TSOs) oversee the management of HVDC grids to ensure stability and compliance with the market schedule, using two layers of controls to manage power flows. The top control layer consists of coordinated controls managed by TSOs to dispatch appropriate converter set points for precise power flow control [17]. In the event of a contingency, the set points automatically adjust to find a new stable operating point. The second control layer consists of local controls in the VSC stations, such as DC voltage droop control, reactive power control loop, and AC voltage control loop, which are used to adjust set points in real-time. These local control loops are grouped under the Grid Following Control strategies [6]. Another control strategy discussed in the study is Grid Forming Control, which is a new concept in HVDC grids. Grid Forming Control establishes a stable AC voltage and frequency reference for the HVDC grid, which is critical for synchronizing AC and DC systems. This control strategy is used to maintain the stability of the HVDC grid during system disturbances, and it is beneficial in weak grid conditions or islanded systems where there is no external AC system reference [73]. Effective control strategies are essential for HVDC grids' safe and reliable operation.

1.4. Controllers

Controllers must be implemented for the previously mentioned strategies to be brought to fruition. Among the several controllers in use today, this thesis delves into PI-based controllers and MPC-based ones.

Currently, most MMCs use cascaded PI controllers to manage their active, reactive power. However, these controllers have slow response times of around 100 ms, which is unsuitable for power systems with high RES. Additionally, they can only control one variable at a time and have limited reach. To address these issues, researchers are exploring nonlinear control methods that can simultaneously control multiple variables within safe limits. One promising approach is MPC, which is a type of nonlinear control used for power electronic converters [12]. The direct and indirect formulations of MPC offer highly desirable options for systems that are predominantly influenced by power electronic converters. These MPC variants have been successfully employed in MMC units to rapidly address frequency deviations resulting from abrupt imbalances in active power within low inertia power systems. With their ability to respond within milliseconds, both direct and indirect MPC formulations prove effective in swiftly mitigating such frequency excursions in MMC-based systems [66].

MPC's MIMO (multi-input multi-output) nature can handle multiple objectives simultaneously. For example, an MPC algorithm block could be used to model the inner current loop of the upper and lower MMCs present in the same Converter station, ensuring that voltage and current constraints are

not violated [46].

1.5. Stability analysis

The stability analysis of dynamic systems is essential to engineering and scientific research. However, carrying this analysis out practically can be challenging, especially for large and complex systems. Solving differential equations in the time domain and analyzing their trajectories is a standard method for determining stability. Still, it can be a very time-consuming and cumbersome process, especially for nonlinear systems [42]. As computing capabilities continue to advance, another approach to assess the stability of a dynamic system is to implement it in software and carry out detailed simulations using numerical methods such as Monte Carlo [41]. However, these methods are often time-consuming and may not provide a definitive conclusion due to the complexity of the system and the exponential number of possibilities and configurations that arise. An alternative solution for determining the stability of a dynamic system without solving its differential equations or resorting to many simulations is to apply the Lyapunov theory [44]. There are two ways of pursuing a Lyapunov-based stability analysis: the indirect method and the direct method. The indirect method involves linearizing the nonlinear system around one operation point and obtaining its eigenvalues. If all of the eigenvalues have negative real parts, then the system is stable in a neighborhood of the chosen operation point for linearization. This approach is called small-signal analysis in the power systems literature because its conclusions are limited to small disturbances that keep the system's trajectory around the chosen operating point. In contrast, the direct method allows for considering nonlinear systems without relying on the linearisation around an operating point. This method is beneficial for analyzing the stability of power systems facing large disturbances, also known as large-signal stability [32]. The system's stability can be asserted by finding a positive Lyapunov function W whose time derivative $\dot{W}$ is negative definite. Using energy functions as Lyapunov candidates is a common approach for analyzing the stability of multi-machine power systems, and power engineers have studied this technique for almost a century. This approach is based on the fact that energy is conserved in physical systems. Therefore, the Direct Lyapunov theory provides a powerful tool for analyzing the stability of dynamic systems. The direct method is advantageous for nonlinear systems and power systems facing large disturbances such as transient phenomena, which is the focus of this thesis.

1.6. Importance of real-time testing and RTDS

Real-time testing is crucial in developing and validating various networks and their control and protection technologies. It involves conducting experiments and simulations in a real-time environment to evaluate the performance, reliability, and functionality of a system or component under realistic operating conditions. Unlike offline or simulation-based testing, real-time testing aims to replicate the tested system's actual dynamics and timing constraints. This allows for an accurate assessment of network behavior, response time, and interactions with external factors. Real-time testing is commonly employed in power systems and control engineering, enabling researchers and engineers to validate designs, identify potential issues, and make informed decisions before deploying networks in real-world scenarios. Real-time testing ensures complex networks' safety, efficiency, and reliability by providing a realistic testing environment. Significant research efforts have been devoted to modeling MMCs in the past decade. To test and validate MMC's external control and protection devices in real time, a real-time simulator (RTDS®) is needed. Furthermore, a detailed model of MMC is crucial for controllability and interaction studies, which is achieved by modeling the MMC in the Field Programmable Gated Arrays (FPGA).

1.7. Thesis motivation

In the pursuit of advancement, the focus has been on making the network more robust (GFM) by enhancing the stability of the network and increasing the speed of responsiveness of the controls. Doing so aimed to generate meaningful insights and foster breakthroughs in HVDC transmission network control and protection.

1.8. Research objectives and contributions of this thesis

The thesis objectives that were completed successfully to the best of my knowledge are:

- Development of DC circulating current suppression control.
- Investigation of (Phase Locked Loop (PLL) less) grid forming control strategies for MMC stations.
- Investigation of Energy-based Circulating Current Suppression Control for the network.
- Investigation of network behavior during weak AC grid[SCR<10] conditions [28].
- Investigation of MPC control and algorithm development.
- Comparison between MPC and PI controls.
- Investigation of large signal stability for the network with grid forming and grid following control strategies with PI and MPC controllers.

This thesis focuses on several research projects on power grid networks. One of the main focus areas has been the development of a DC circulating current suppression control system. Grid forming control strategies for MMC stations explicitly focusing on energy-based circulating current suppression control have also been studied.

Another aspect of this research has been examining the behavior of power networks during weak AC grid conditions, particularly the effects of low short-circuit ratios (SCR) on network performance.

Additionally, various control algorithms for power grids have been explored, including investigating MPC control and algorithm development and comparing the effectiveness of MPC versus PI controllers. Lastly, large signal stability for power networks when using grid forming and grid following control strategies with PI and MPC controllers have been discussed in this thesis. All of this has been implemented in a real-time environment on RSCAD/RTDS®

1.9. Report outline

The thesis report comprises eight chapters that delve into the intricate details of HVDC technologies, control algorithms, and controllers. Chapter 1 provides a succinct overview of the thesis's framework, motivation, and research objectives. Chapter 2 is dedicated to the HVDC network, which was designed and used as a test bench to analyze the control algorithms and controllers. This chapter also includes the specifications of the network and the start-up procedure to energize it. Chapter 3 presents a current suppression control developed for the condition post-DC fault clearance state. The grid following and grid forming converter control strategies are explored and discussed in Chapter 4. Chapter 5 presents an energy-based current suppression control, while Chapter 6 elaborates on the Model Predictive control controller with constraints and cost function for the controller. This chapter also compares the PI-based and MPC-based controllers for various scenarios. Chapter 7 contains the stability analysis for the control strategies and the controllers implemented in this thesis. Finally, Chapter 8 presents the conclusions drawn from the research conducted in this thesis.

1.10. Publication

Part of this work is accepted for publication in:

Rohan Kamat Tarcar, Ajay Shetgaonkar, Marjan Popov, Mart van der Meijden, Wilhelm Winter, Mario Ndreko, Robert Dimitrovski, Matthias Burkhardt, and Aleksandra Lekić, "Post DC Fault Circulating Current Suppression Control," *IEEE Power & Energy Society General Meeting 2023*, 2023.

1.11. Conventions

The sign convention used in this thesis is as follows. When the power is consumed/injected, the sign of active power (P) and reactive power (Q) is positive ($+v_e$), and if the power is generated, the sign of active power (P) and reactive power (Q) is negative ($-v_e$).

To analyze the behavior of the control strategies and the controllers implemented in the network, the protection algorithms are deactivated, as the protection algorithms would have altered the actual behavior of the control. ls making the analysis unclear and convoluted due to the protection algorithms coming into action when its limits were transgressed.

2
The HVDC Network

2.1. MMC models

Various computational models are available for simulating VSCs, which are crucial components of future DC grids. The type of model chosen depends on the time frame of the phenomena being analysed on the DC grid. Different models, such as EMT and phasor models, are available to simulate these phenomena. The different types of computational models available for simulating VSCs, based on the level of detail and complexity, are listed below:

- Type 1: Full Physics-Based Models - too complex and difficult to parameterise for grid models, as switches and diodes are represented by differential equations
- Type 2: Full Detailed Models - based on simplified nonlinear IGBT models, can take into account every conduction mode of a bridge and can only be implemented in EMT tools
- Type 3: Models Based on Simplified Switchable Resistances - IGBT and diodes are represented by two-value resistors and can only be implemented in EMT tools.
- Type 4: Detailed Equivalent Circuit Models - based on Type 3 but with a reduction performed to reduce the number of electrical nodes that describe the converter, including accurate impacts of different capacitors voltages at each module level. This model can only be implemented in EMT tools.
- Type 5: Average Value Models (AVM) Based on Switching Functions - AC and DC side characteristics are modelled as controlled current and voltage sources with harmonic content generated by the conversion process, with a simulation speed advantage over Type 4 models. This model can only be implemented in EMT tools.
- Type 6: Simplified Average Value Models - AC and DC side characteristics are modelled as controlled current and voltage sources that produce waveforms that track their control-function input values without any switching harmonics. It can be implemented in EMT and phasor-domain transient simulation tools.
- Type 7: RMS Load-Flow Models - uses steady-state converter outputs without modelling detailed transients, suitable for load flow simulations of HVDC networks.

The average value models are commonly known as Type 5 models, where the AC and DC sides are modelled as controlled current and voltage sources that generate harmonic content during the conversion process, such as IGBT switching. These models also allow for incorporating non-repetitive behavior during protection operations. However, Type 5 models assume that the SM capacitor voltages are balanced. Compared to Type 4 models, Type 5 models have a faster computing time. These models are useful for studies involving AC and DC transients, high-level control system design, and harmonic studies.
The GTFPGA-based models fall under the category of detailed models (Type 4), which are based on simplified nonlinear IGBT models. These models can consider every conduction mode of a bridge and can model the nonlinear V-I curve of the IGBT/diode using a nonlinear resistor. However, these models could not be used in real-time simulations in the past due to limited processing capabilities. But now, they can be used just like average models. These models are useful in studies involving faults of SMs and validating simplified models. It is important to note that these models can only be implemented in EMT tools[1].

Table 2.1: Comparison between the average value model and the GTFPGA model

	Average value	**Detailed (GTFPGA)**
Type of model	Type 5	Type 4
Computation time	20-50 times faster than detailed model	slower than average model
Application	EMT	EMT
Type of studies	Studies of AC and DC transients – high level control system design-harmonic studies	Detailed studies of faults in SMs; Used to validate simplified models

FPGA-based detailed MMC models

Field Programmable Gate Arrays (FPGAs) to create detailed models of MMCs have proven to be a highly effective method for simulating MMC systems' internal dynamics and control strategies. These models use hardware description languages like Verilog or VHDL to meticulously implement the converter's power circuitry, control algorithms, and switching behavior. By representing the system at a granular level, these models offer a comprehensive and accurate simulation of MMC behavior, including SM capacitors' voltage balancing, charging and discharging, control, and switching strategies.

FPGAs offer significant advantages when it comes to implementing detailed MMC models. They provide the computational power necessary to handle intricate calculations and switching patterns while also allowing for real-time simulation, which is crucial for precise analysis of transient responses, harmonics, and system stability. Additionally, FPGAs offer high parallelism, which can significantly reduce simulation time.

These detailed models are helpful for advanced research, optimisation, and control design. Researchers can use them to investigate the impact of various control strategies and parameter variations on MMC performance. Furthermore, these models facilitate rapid prototyping and design refinement through real-time testing and evaluation of control algorithms. Finally, FPGA-based models enable hardware-in-the-loop simulations, which accurately represent network behavior by allowing the detailed MMC model to interact with physical devices or control systems.

To implement the MMC switching model, a Xilinx VC707 FPGA called GTFPGA is used with firmware for RTDS® connection to meet high computational requirements. The MMC's operation is solved with a small time-step of 1.4 to 3μs. A GTFPGA unit represents each leg of the MMC, and three GTFPGA units are required to designate one MMC unit [45]. Additionally, two GTFPGA units are used to implement the SM capacitor voltage balancing controller, which is required due to the high number of SMs. The connections between RTDS® and GTFPGAs and between GTFPGAs are established using two full-duplex fibre optic cables with the Aurora protocol. To represent each detailed MMC, GTFPGAs are used, with three GTFPGAs for the MMC unit's legs and two GTFPGAs for the SM capacitor voltage balancing controllers for each MMC unit. In contrast to the average model, the switching model of the MMC allows each SM to be controllable and observable. Each valve of the MMC is represented as a surrogate network in RSCAD/RTDS®, consisting of four sections: the Reactor section, Block section, $+ve$ inserted SMs section, and a Bypass section. These sections are connected in series, and depending on the SMs' firing signals, several SMs are added to these sections [67].

2.2. Network background

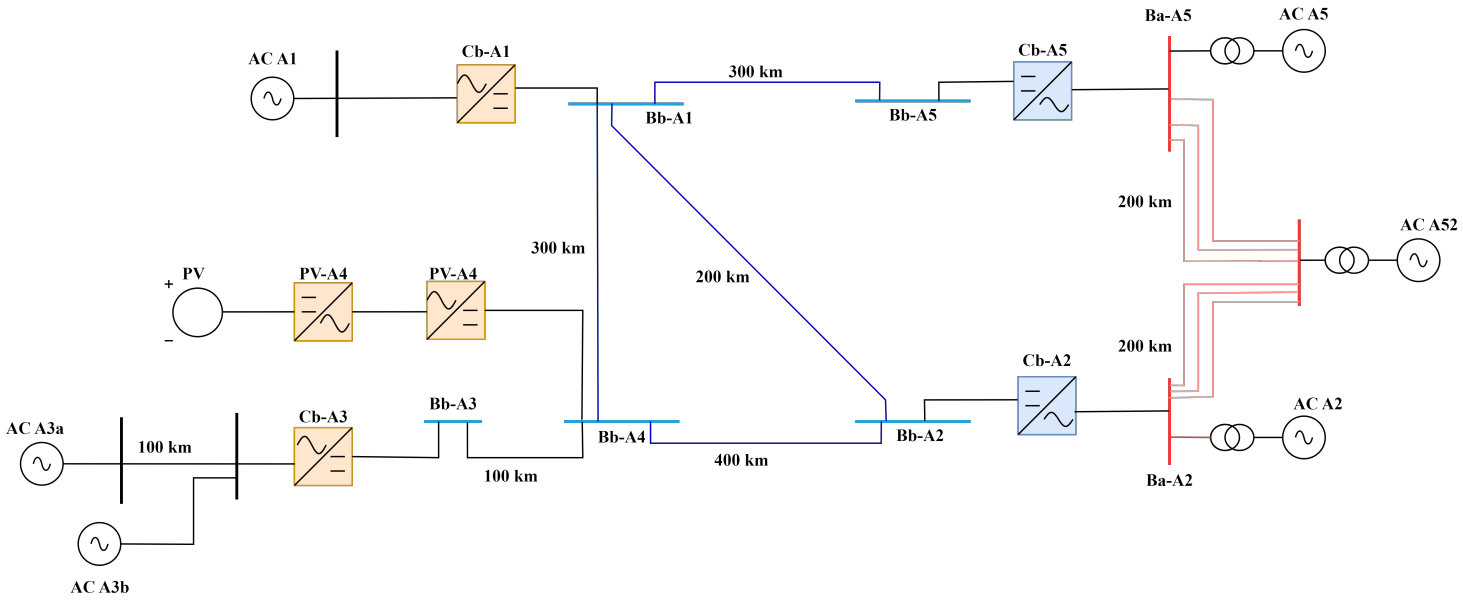

Figure 2.1: Cigre B4 DC grid test network.

The model created for this thesis is derived from the CIGRE B4.72 AT14 BM1, Fig. 2.1,[3]. The modified network, Fig. 2.3, is called the Four terminal ±525 kV bipolar metallic return HVDC network.

2.2.1. The four terminal ± 525 kV bipolar metallic return HVDC network

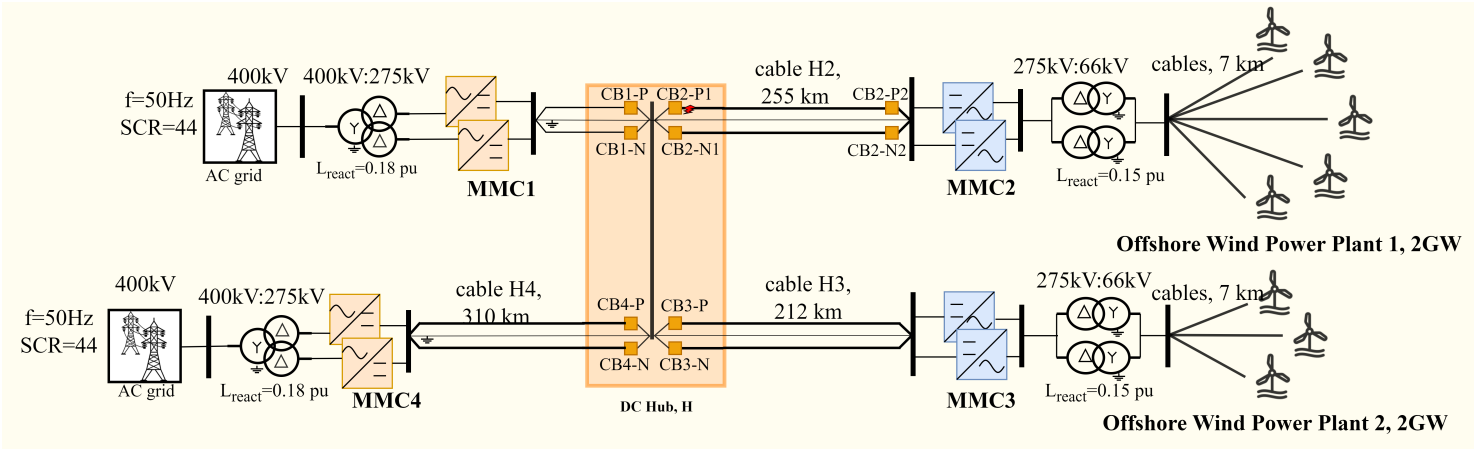

Figure 2.2: The single line diagram of four terminal ±525 kV bipolar metallic return HVDC network.

The network description

The HVDC network, Fig. 2.2 and Fig.2.3, is a 6 GW, ±525 kV bipolar ground return four-terminal HVDC network. The converter is a half-bridge topology. Among the four converter stations, one MMC of the MMC1 converter and both MMCs of MMC4 (i.e., onshore converters) are the average MMC models, and one MMC of the MMC2 converter station is the average model. The remaining MMC models are detailed equivalent models modelled on FPGAs and connected to RTDS® via GTIO ports. The FPGA MMC unit consists of MMC valves and its lower-level control.

This network can also be divided into three sub-systems: the onshore AC network and the DC breaker (DC switchyard), the DC network, and the offshore AC network (offshore wind farms). The onshore AC

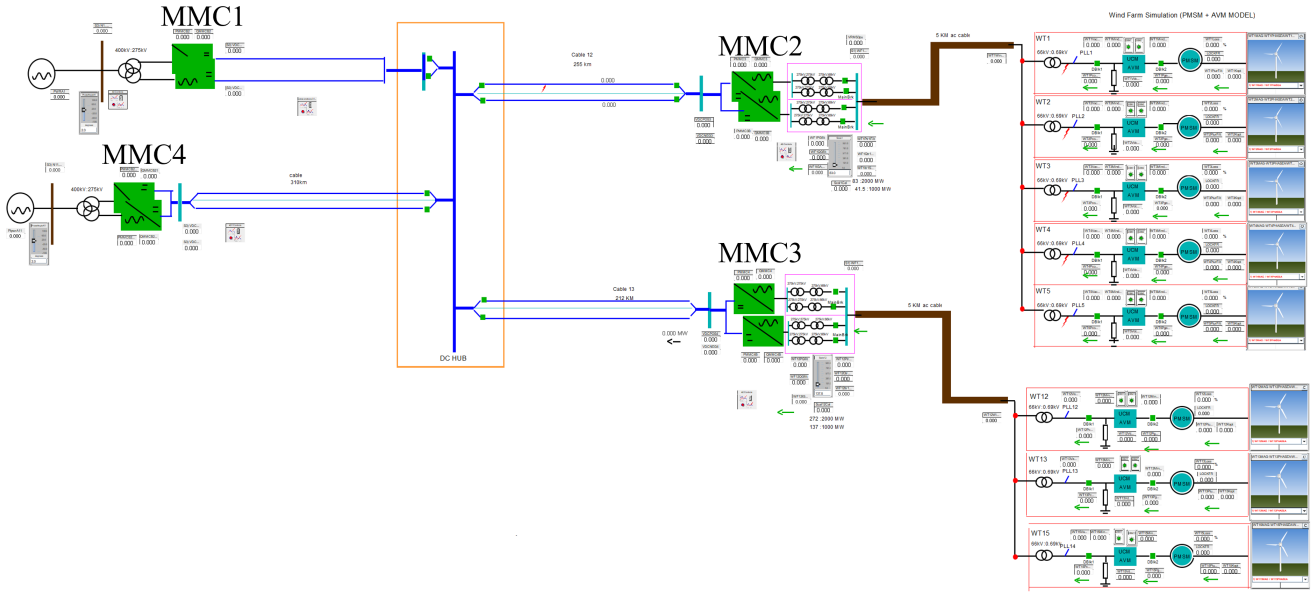

Figure 2.3: The single line diagram of the network in RTDS® Runtime

network consists of two stations, each connected to Thevenin's equivalent circuit of a strong grid. The rated line-to-line (LL) voltage is 400 kV. These stations are connected to a DC breaker (switchyard). Each onshore terminal converter station has$1Y - D$, 1 phase -3 winding$(1ph - 3W)$ transformer with each rating of 6 GVA. The voltage ratio of this transformer is 400 kV/275 kV. The DC network consists of three cable links: cable H2 (cable from DC breaker to MMC2, 255 km), cable H3 (cable from DC breaker to MMC3, 212 km), and an onshore cable (cable H3) between the MMC4 and the DC breaker of 310 km. The cables are modelled as a frequency-phase-dependent model. Further, due to metallic return topology, the cable link consists of 3 cables (i.e. a positive, a negative, metallic return cable per cable link). All stations except MMC1 are connected to the Dc breaker (switch yard) with cables, whereas the MMC1 station is directly connected to the DC breaker, as seen in 2.3. The only difference between MMC1 and MMC4 stations is the control discussed in the coming chapters. The offshore AC network consists of offshore converter stations and aggregated average wind farms. The offshore converter MMC2 is connected to the offshore AC network via two$D - Y$ transformers. The rating of this transformer is $275kV/275kV$, 4.5 GVA. Further, these transformers are connected to another transformer station via OHL. This transformer has a voltage ratio of 275 kV/66kV. This transformer act as a VA scaled-up transformer(to mimic large wind farms of 2 GVA capacity). Thus, choosing the proper scaling factor can achieve a power rating of 4.5 GW. For reliability, two of these transformers are connected in parallel. Further, the lower voltage end of this transformer is connected to the five wind turbines through an AC cable of 7 km to replicate realistic scenarios. Each of these turbines has a rating of 5 MW at a wind speed of 16 m/s. The type 4 wind turbine is used. A similar topology is employed for the AC network connected to converter station MMC3. However, only three wind turbines are connected.

2.2.2. VARC DCCB

All the DC breakers used in this network are of the VSC-Assisted Resonant Current (VARC) type. This newly emerging technology can be used as protection for offshore MTDC grids. Due to the absence of current zeros in a DC network, developing DCCBs is more difficult than ACCBs. High Voltage Direct Current DC Circuit Breakers (HVDC DCCBs) are essential components that are used to clear DC fault currents and isolate faults from HVDC converters, such as half-bridge MMCs. It is crucial to clear the DC faults quickly to prevent MMCs from being blocked. However, fast transients and high short-circuit currents make DC fault interruption challenging. To interrupt the DC fault current, the DCCB must dissipate the energy stored in the inductance in the HVDC lines. Therefore, the DCCB consists of an "energy absorbing branch" containing surge arresters (SAs) connected to the mechanical switch. During

the interruption, the line current is forced to commutate to this branch, and the clamping voltage of the SA determines the transient interruption voltage (TIV) that occurs across the interrupting switch during current suppression. During normal operation, the line current is carried by mechanical contacts in the "main branch." However, switching events temporarily transfers it to a parallel branch. This is the main working principle behind the VARC DCCB models. Fig. 2.4 shows the single-line diagram of the VARC DCCB, and Fig. 2.5 exhibits the artificial zero crossing of the DC breaker and the timeline of the operation of the VARC DCCB and the neutralization of the fault [39, 40, 64].

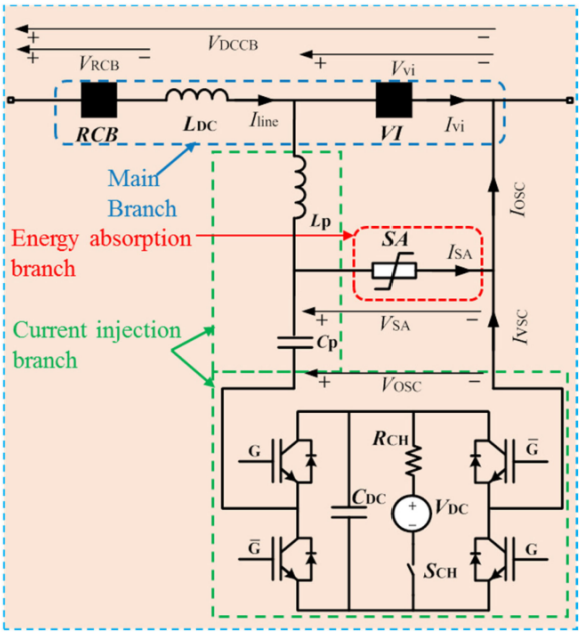

Figure 2.4: VARC DCCB Schematic [40]

2.3. Network specification

2.3.1. MMC parameters

Table 2.2 shows the Onshore MMC parameters, and Table 2.3 shows the Offshore MMC parameters that are used in the Four terminal ±525kV bipolar metallic return HVDC network. The parameters in black are for the entire station, whereas those in grey are for the MMC submodules.

Table 2.2: Onshore MMC parameters (The parameters in black are for the entire station, whereas those in grey are for the MMC submodules.)

Onshore MMC Parameters	
Onshore rating of the converter and transformer	6 GVA
Onshore transformer type	1*P*3*W*
Onshore transformer voltage ratio	400:275kV
Onshore X/R ratio	10
Onshore SCR range	43-45
Transformer leakage reactance	0.18 p.u.
MMC SM Voltage	2.4 kV
MMC SM current	2 kA
SM Capacitance	25 mF
Q factor of the MMC	100-450
No. of SM	240

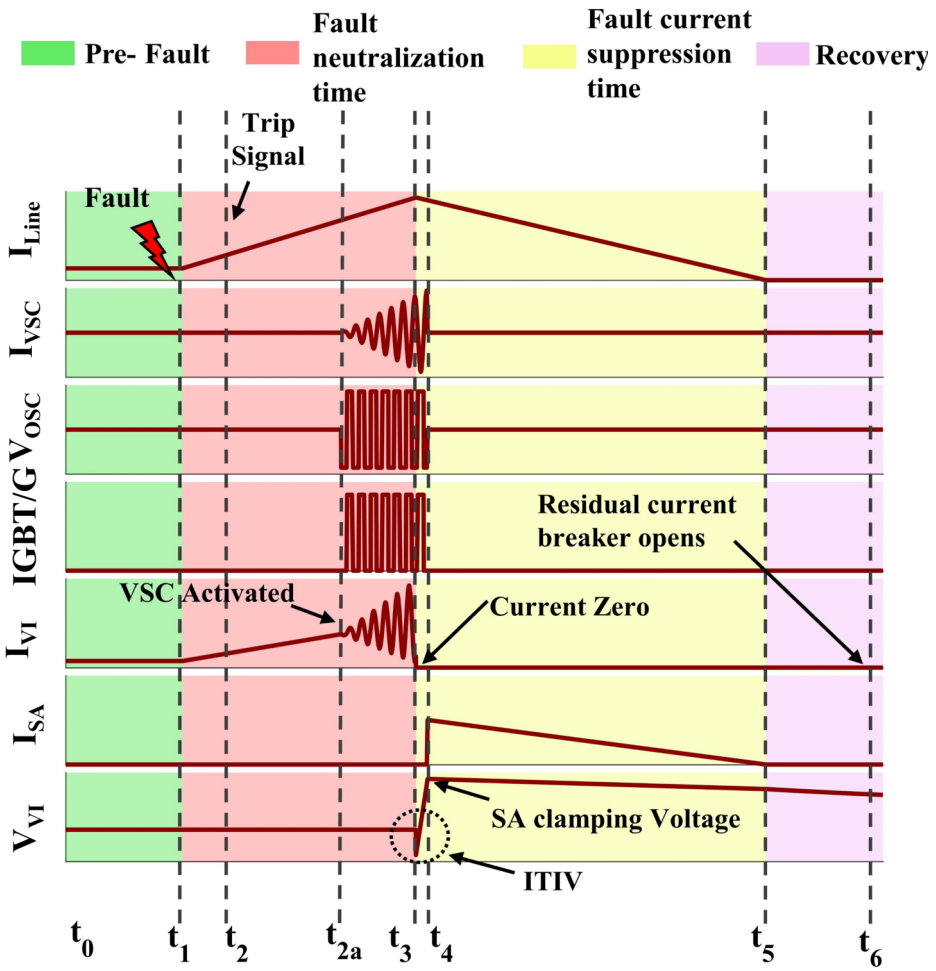

Figure 2.5: Current and Voltage waveforms in VARC DCCB [40]

2.3.2. Onshore DC hub

The DC hub is a block where all the DC cables from the four converter stations terminate at their respective breakers. Making the topology of this entire network a point-to-point network(star network), with the DC Hub acting as the most critical node in the network. Fig.2.2, shows the DC Hub and the connections to the converters.

2.4. Equivalent mathematical model and representation

In this section, a mathematical representation of the MMCs is presented. Fig. 2.6 depicts the single terminal of the network, which is further simplified as Fig. 2.7, to be utilized for deriving the MMC equations. Each MMC has three legs, and each leg consists of two arms. The legs represent the phases, and the arms are the upper and lower arms of the MMCs, which have N SMs each (N_{SM}).

The converter topology is depicted in Fig. 2.7. Variables from Fig. 2.7 are defined for all three phases, i.e. j: a,b,c. SMs (SMs) are considered with their averaged equivalents, R_{arm} and L_{arm} being the resistance and inductance, respectively. Each SM has SM capacitance C_{SM}. The following equations for the voltage and the current can be written for the upper and lower arms:

$$v_{Mj}^{U,L} = m_j^{U,L} v_{Cj}^{U,L}, \tag{2.1}$$

$$i_{Mj}^{U,L} = m_j^{U,L} i_j^{U,L}, \tag{2.2}$$

where $m_j^{U,L}$ are the corresponding upper and lower arm insertion indices. The converter model is developed as in [4]. Using the $\Sigma - \Delta$ nomenclature, the variables in the upper and lower convert arms

Table 2.3: Offshore MMC Parameters (The parameters in black are for the entire station, whereas those in grey are for the MMC submodules.)

Offshore MMC Parameters	
Offshore rating of the converter and transformer	4.5 GVA
Onshore transformer type	$3P2W$
Offshore transformer voltage ratio	275 kV:275 kV, 275 kV:66 kV
Transformer leakage reactance	0.15 p.u.
MMC SM Voltage	2 kV
MMC SM current	1 kA
SM Capacitance	16mF
No. of SMs	240

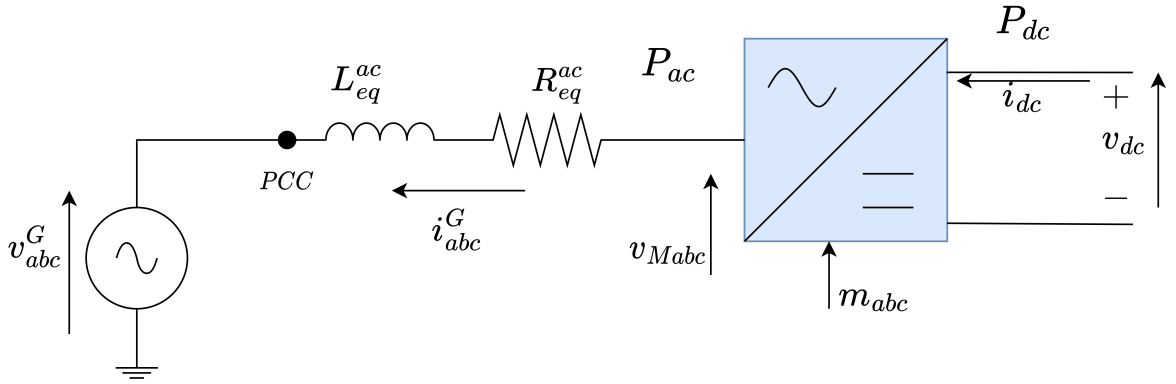

Figure 2.6: Diagram of MMC with AC grid and DC voltage.

can be represented as:

$$i_j^{\Delta} = i_j^U - i_j^L, \quad i_j^{\Sigma} = \frac{i_j^U + i_j^L}{2}, \tag{2.3}$$

$$v_{Cj}^{\Delta} = \frac{v_{Cj}^U - v_{Cj}^L}{2}, \quad v_{Cj}^{\Sigma} = \frac{v_{Cj}^U + v_{Cj}^L}{2}, \tag{2.4}$$

$$m_j^{\Delta} = m_j^U - m_j^L, \quad m_j^{\Sigma} = m_j^U + m_j^L, \tag{2.5}$$

$$v_{Mj}^{\Delta} = \frac{-v_{Mj}^U + v_{Mj}^L}{2} = -\frac{m_j^{\Delta} v_{C_j}^{\Sigma} + m_j^{\Sigma} v_{C_j}}{2}, \tag{2.6}$$

$$v_{Mj}^{\Sigma} = \frac{v_{Mj}^U + v_{Mj}^L}{2} = \frac{m_j^{\Sigma} v_{Cj}^{\Sigma} + m_j^{\Delta} v_{V_j}^{\Delta}}{2} \tag{2.7}$$

$$L_{eq}^{ac} \frac{d\boldsymbol{i}_{abc}^{\boldsymbol{\Delta}}}{dt} = \boldsymbol{v}_{mabc}^{\boldsymbol{\Delta}} - \boldsymbol{v}_{abc}^{G} - R_{eq}^{ac} \boldsymbol{i}_{abc}^{\boldsymbol{\Delta}} \tag{2.8}$$

By making use of the Clarke Park transformation(ABC to dqz frame transformation),[4], the set of differential equations can be written with capacitor voltages and inductor currents in the d-q domain (A.2):

$$\frac{d}{dt}\left(\vec{i}_{dq}^{\Delta}\right) = \frac{\vec{v}_{Mdq}^{\Delta} - \left(\omega L_{eq}^{ac} J_2 + R_{eq}^{ac} I_2\right) \vec{i}_{dq}^{\Delta} - \vec{v}_{dq}^{G}}{L_{eq}^{ac}} \tag{2.9}$$

$$\frac{d}{dt}\left(\vec{i}_{dq}^{\Sigma}\right) = -\frac{\vec{v}_{Mdq}^{\Sigma} + \left(R_{arm} I_2 - 2\omega L_{arm} J_2\right) \vec{i}_{dq}^{\Sigma}}{L_{arm}}, \tag{2.10}$$

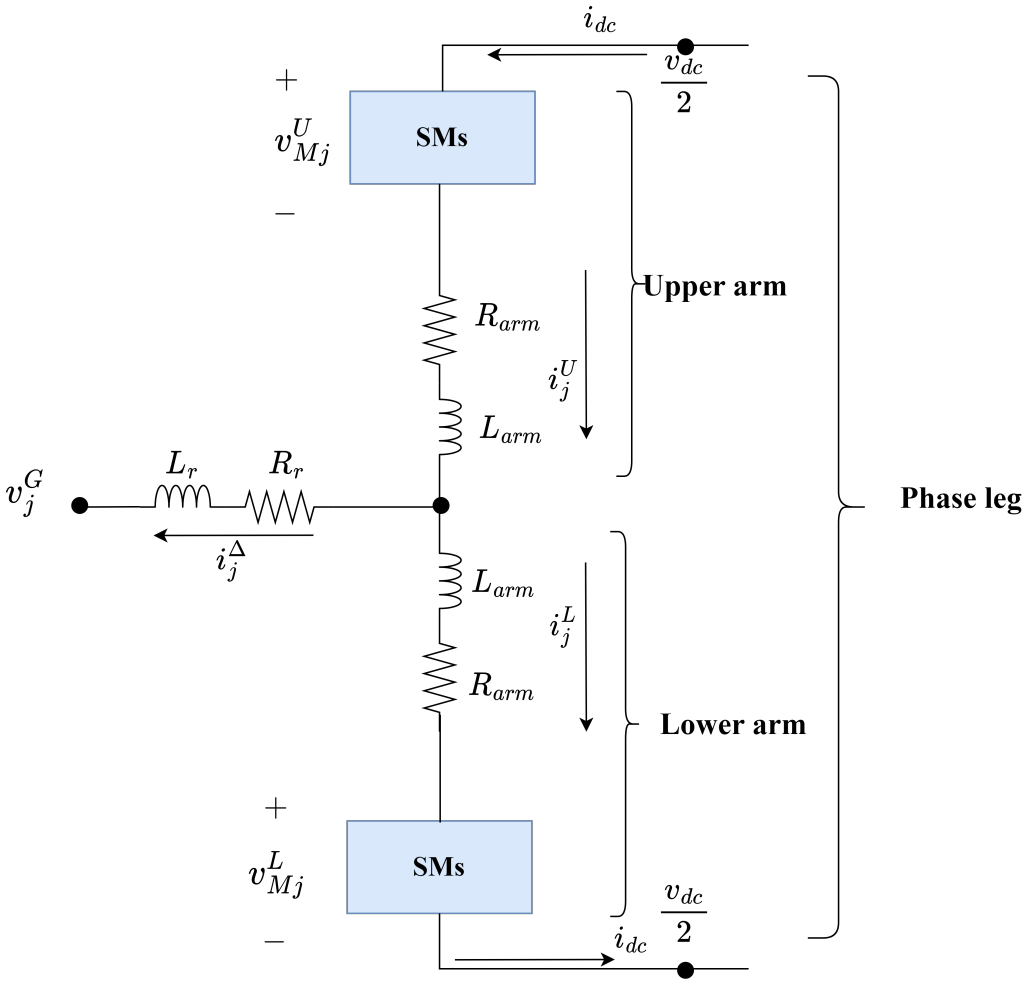

Figure 2.7: Diagram of MMC depicting a single leg for simplicity purposes.

$$\frac{d}{dt}\left(i_z^{\Sigma}\right) = \frac{v_{dc}}{2L_{arm}} - \frac{v_{Mz}^{\Sigma} + R_{arm} i_z^{\Sigma}}{L_{arm}} \tag{2.11}$$

$$\frac{d}{dt}\left(\vec{v}_{dq}\right) = \omega J_2 \vec{v}_{dq} + \frac{N_{SM}}{C_{SM}} \vec{i}_{dq} \tag{2.12}$$

where,

$$L_{eq}^{ac} = L_r + \frac{L_{arm}}{2}, \qquad R_{eq}^{ac} = R_r + \frac{R_{arm}}{2}$$

and

$$J_2 = \begin{bmatrix} 0 & 1 \\ -1 & 0 \end{bmatrix} \text{ and } I_2 = \begin{bmatrix} 1 & 0 \\ 0 & 1 \end{bmatrix}.$$

2.5. Start-up sequence of the HVDC network

This section discusses the start-up sequence of the network. Due to the novel nature of the network configuration, it requires a start sequence that is not exactly listed in the literature but is based on the concept of charging cables, which is indeed mentioned in the literature. Listed below are the steps to be followed for the **starting sequence** of the model in the run-time environment.

Due to its scalability and reliability, the radial topology of the Multi-terminal High Voltage Direct Current (MTDC) power network is a preferred connection for gigawatt-renewable power. However, a radial topology with a metallic return bipolar converter configuration MTDC network possesses

technical challenges regarding DC fault current interruption and grid expansion. Furthermore, such HVDC networks are energized in a specific manner, usually involving a separate energizing controller. This thesis presents a design of DC Hubs with DCCBs along with a network energization sequence without requiring a separate controller.

The start-up sequence proposed in [80] requires a separate control to ensure a safe energization of the networks as the network does not contain DCCBs. The sequence described in [5] involves the insertion of resistors with associated bypass breakers. Implementing the DC-Hub and DCCBs makes it possible to realize an energization sequence without needing a separate black start control. This start-up sequence is addressed in this paper. Furthermore, these start-up sequences apply only to specific scenarios with rigid bipoles or only monopolar configuration of the MMCs in the network or with LCC rather than VSC in the converter stations, in which the zero current or zero voltage modes of a start-up are used, the latter being in which the DC voltage is initially limited to 0.5 pu till the converter reaches its rated value and, vice versa [35].

Note: During the startup sequence, the protection protocols in place are temporarily disabled to avoid spikes in the active power during pole closure. The DC control strategy of MMC1 causes this.

The energization of the MTDC requires a startup sequence to ensure that the network will operate nominally [27]. This sequence is also crucial for pre-charging the MMCs' SM capacitors [80]. The proposed startup sequence considers the control strategies implemented for the network converter stations and the control strategies' settling times. The sequence proposed is as follows:

- Deblocking of the MMCs in MMC1 and closure of the VARC DCCBs (CB1-P and CB1-N) occurs simultaneously, thereby the DC voltage to ±525 kV on the terminals. MMC1 sets the reference voltage for the DC Hub and then the Hub charges all the cables.
- Deblocking of the MMCs in MMC2 and closing VARC DCCBs (CB2-P1,2 and CB2-N1,2) is only done after the terminal DC voltage is stabilized at ±525 kV. This ensures a stable rise in the voltage of MMC2 with minimal disturbances. WPP 1 is then started and deblocked to increase the terminal voltage of MMC2 to 530 kV.
- The energization of MMC3 is the same as that of MMC2, as the control strategy and the power capacities of the MMCs and the WPP connected are the same.
- Since the MMCs in the MMC4 are controlled in *P, Q* control strategy, the active power of the MMCs is set to consume 2 GW. Therefore, this converter is deblocked, and the VARC DCCBs (CB4-P and CB4-N) are closed only after the total production of active power is more than 2 GW. Hence, MMC4 is deblocked after the total production is 4 GW. This ensures that MMC4 gets 2 GW of active power so that the controls can operate as expected.

Table 2.4 also lists the events that occur during the startup sequence chronologically.

Table 2.4: Sequence of events with their time instants during the startup

Time-step	Events
$\mathbf{t_1}$	MMC1 positive pole is deblocked and CB1-P is closed
$\mathbf{t_2}$	MMC1 negative pole is deblocked and CB1-N is closed
$\mathbf{t_3}$	MMC2 positive pole is deblocked; CB2-P1 and CB2-P2 is closed
$\mathbf{t_4}$	MMC2 negative pole is deblocked; CB2-N1 and CB2-N2 is closed
$\mathbf{t_5}$	Offshore WPP 1 is started and deblocked
$\mathbf{t_6}$	MMC3 positive pole is deblocked and CB3-P is closed
$\mathbf{t_7}$	MMC3 negative pole is deblocked and CB3-N is closed
$\mathbf{t_8}$	Offshore WPP 2 is started and deblocked
$\mathbf{t_9}$	CB4-P is closed
$\mathbf{t_{10}}$	CB4-N is closed
$\mathbf{t_{11}}$	MMC4 is deblocked

Fig. 2.8 shows the variation of the DC voltage and the active power during the start-up sequence of the network. Since the rated DC voltage of the network is ±525 kV, the measured DC pole-to-pole voltage is 1050kV, which is used for the per-unit conversion of the DC voltages. Furthermore, according

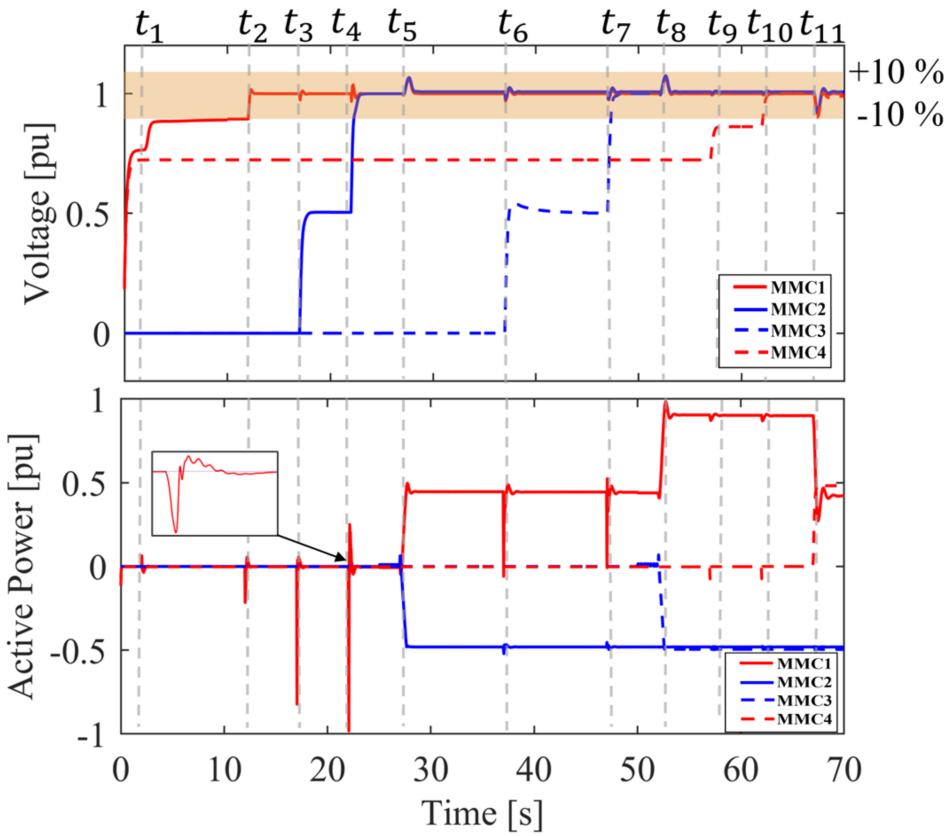

Figure 2.8: behavior of DC voltages and active power during the network's startup.

to the CIGRE and ENTSO-E standards, the over- and under-shoot of the voltages should be within the ±10% margin [16], which can be seen as valid in Fig.2.8. Since the onshore converters (MMC1 and MMC4) are connected to the onshore strong AC grid, the total blocking voltage of the MMCs in the rectifier mode is about 0.6 pu (this is before the DCCBs of the onshore converters are closed and the converters are deblocked). This starting sequence also considers the voltage surges that occur when the VARC DCCBs are closed. Therefore, the breakers on the positive pole are closed first, and only after the positive pole voltage has reached its specified value of +525 kV the DCCB on the negative pole is closed.

Additionally, the spikes observed in the active power curve of MMC1 from Fig. 2.8 are caused by the sudden voltage fluctuation when DCCBs close. Namely, the DC voltage control of MMC1 tries to reach its set point, which causes an unconventional spike in the active power at those instances. The voltage and active power spikes are observed to be in proportion to the distance of the DC cable, i.e. the longer the cable, the bigger the fluctuation spikes. The final dip of the voltages and the active power at t_{11} is caused by deblocking of the MMC4, which is governed by P, Q control.

This unique sequence is only possible because of the presence of VARC DCCBs in the DC Hub, which allows rapid connection and disconnection of the cables in the network.

This novel sequence was also published as a part of a research paper at the IEEE PESGM Conference [1]. The second part of this Conference paper is presented in the next Chapter 3.

[1] Accepted on the 15^{th} of Feb,2023, under the title, Post DC Fault Circulating Current Suppression Control.

3
Post DC fault circulating current suppression control

This Chapter discusses the circulating current suppression on the DC side of the bipolar MMC-based power system after a DC fault interruption. The circulating current in MMCs is usually controlled inside the MMCs by applying a circulating current suppression control (CCSC) [13, 79, 65]. A few more current suppression controllers that use proportional resonant control only work well when the number of SMs is high [84, 85], contrary to the controller discussed in this paper, which is not dependent on the number of SMs. Upon DC fault current interruption in a bipolar metallic configuration, the nominal current flows through the metallic return. Furthermore, after the re-close of the DCCB, a circulating current leaks into the metallic return path of the cable. As a result, the network has a power imbalance during the post-fault period. To our knowledge, evidence has yet to be reported in the literature explaining the mentioned phenomena. Hence, the circulating current is generally left uncontrolled [3]. In this paper, the aforementioned circulating current on the DC side is referred to as the residual metallic return current.

3.1. Post fault DC circulating current imbalance

The metallic ground return implemented with the bipolar configuration of the MMCs provides a return path for the current during and after fault current interruption. A temporary PG fault was implemented on the positive pole of the cable H2 at the point of contact between the DC Hub and the positive pole cable termination. This fault, in reality, could resemble a faulty contact and therefore have real-life inferences. Since this fault is between the DC Hub and MMC2, some major observations were made in MMC2. It was observed that the rapid de-energization and energization of the MMC during and after the fault and the closure of the DCCB pole led to a residual current in the metallic return. This residual circulating DC current causes an imbalance in the DC currents in the poles of the cables. This imbalance further created a magnitude difference in the DC voltages, the active and reactive powers of the MMC2, and the power transferred through the cable H2, as seen in Table 3.1. The metallic return current is also depicted in Fig. 3.3.

Fig. 3.3 shows the current through the dedicated metallic return of cable H2. Before the fault is imposed, the current through the metallic return is observed to be 0 kA, which aligns with the nominal operating conditions. At the time instance t_f, the PG fault is imposed and the transient current rushes through the metallic return. After the fault has cleared, the current through the metallic return is around 3 kA, which is according to the expectation since only one pole (negative) is still in operation. All of the planned 2 GW of power flows through this pole. At t_c, when the CB2-P1 and CB2-P2 are closed, another spike in the metallic return current is observed before reaching a steady state value of 0.32 kA. This residual current is responsible for the imbalance caused in the MMC bipolar converters, the power delivered through cable H2, and the currents in cable H2, as seen in Table 3.1. Fig. 3.3 shows the current through the dedicated metallic return of cable H2. Before the fault is imposed, the current through the metallic return is observed to be 0 kA, which aligns with the nominal operating conditions. At the time instance t_f, the PG fault is imposed and the transient current rushes through the metallic return. After the fault has cleared, the current through the metallic return is around 3 kA, which is according to the expectation since only one pole (negative) is still in operation. All of the planned 2 GW of power flows through this pole. At t_c, when the CB2-P1 and CB2-P2 are closed, another spike in the metallic return current is observed before reaching a steady state value of 0.32 kA. This residual current is responsible for the imbalance caused in the MMC bipolar converters, the power delivered through

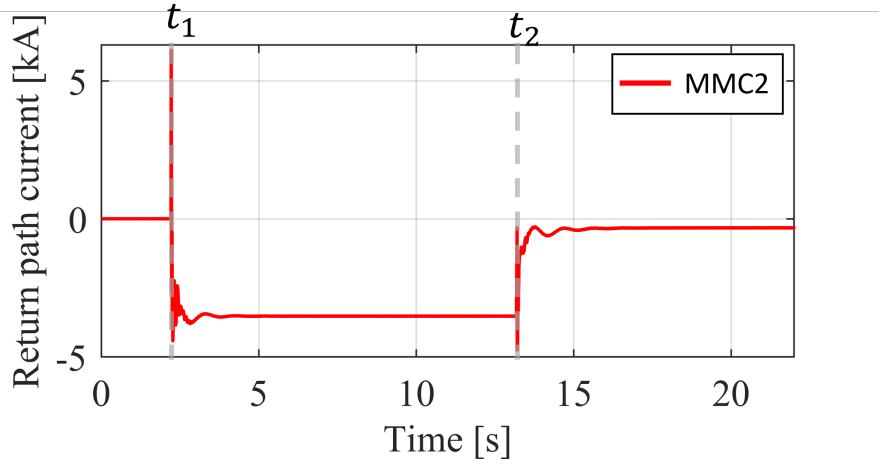

Figure 3.1: The metallic return current before and after the fault.

cable H2, and the currents in cable H2, as seen in Table 3.1.

3.2. DC circulating current suppression control

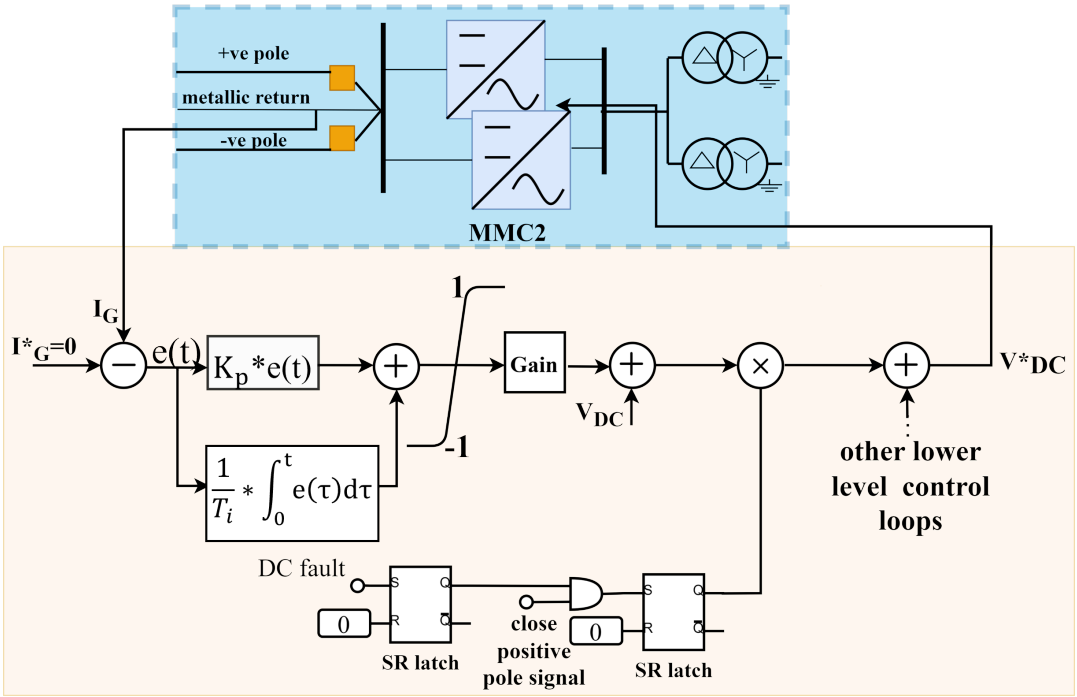

Figure 3.2: Block diagram of the zero-current controller.

As a solution for the post-fault metallic return current imbalance, a PI controller was implemented and tuned to counteract the imbalance observed in Fig. 3.3. Fig. 3.2, shows the block diagram of the controller. The current from the metallic return is fed into the PI control loop, and the output of this loop is fed to V^*_{dc}, i.e. lower-level control of the MMC. The current from the metallic return is compared against the metallic return reference current I^*_G, which is set to be 0 pu. This facilitated the suppression of metallic return current, resulting in the positive and negative pole DC currents being nearly equal in magnitude, thereby balancing all the parameters of the bipolar MMC station. The controller is only activated after the fault has been cleared and the DCCBs have been closed after the fault clearance event, as there is no necessity for this controller during the start-up sequence or during the occurrence of a

Table 3.1: Comparison of MMC2's parameters without and with the controller

MMC2	Without controller			With controller		
	Positive pole	Negative pole	Metallic return	Positive pole	Negative pole	Metallic return
DC currents (kA)	1.645	-1.964	-0.3187	1.821	-1.814	- 0.00705
Power transferred (MW)	871.2	1043	172	960.3	955	5.1
Active Power of MMC (MW)	-1002	-1050	-	-964.4	-960.4	-
Reactive Power of MMC (Mvar)	104.8	-496.8	-	-58.87	-57.74	-
DC voltage (kV)	528.8	-529.5	-	529.1	529.1	-

fault. This controller's function is to suppress the residual metallic return current in the cable after the fault. The activation logic is depicted in Fig. 3.2. For the controller, the integral gain $T_i = 5s$ makes it a slow-type controller, and its proportional gain is $K_p = 1$. The controller is not deactivated as it does not affect the normal operation of the network.

3.3. Verification of the proposed control

As seen in Fig. 3.3, the controller is added to suppress the residual current in the metallic return. It can be seen that up until time instance $t = t_c$, the current signal with the controller retraces the path of the current without the controller. But, after $t = t_c$, the metallic return current with the controller has a steeper slope and reaches a lower current value faster than the one without the controller. The zoomed portion of Fig. 3.3 shows that the second peak of the controlled current (9 A) is much lower than the uncontrolled current (1.2 kA) at the same time instant $t = 13.2$ s. The steady-state amplitude of the metallic return current is found to be 7A, while the magnitude of the metallic return current without the controller was 320 A. From Fig. 3.4 and Table 3.1, it is also observed that with the addition of the current

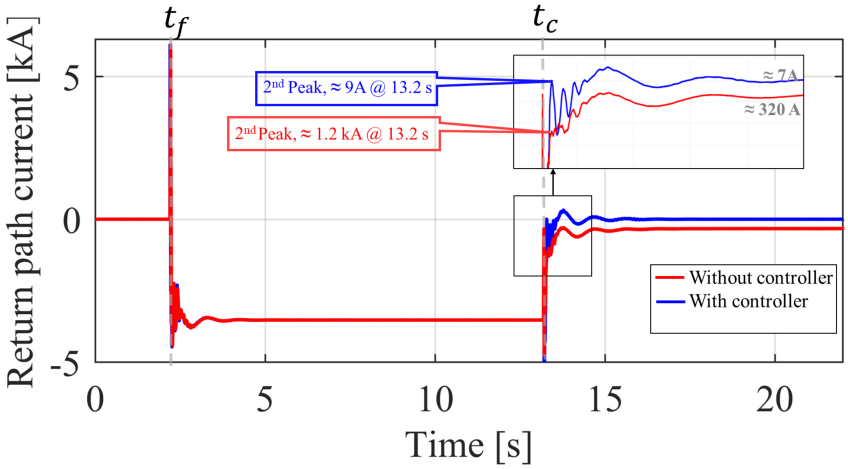

Figure 3.3: Metallic return current behavior with and without the controller.

suppression controller, the MMC2 operates in a steady state. Therefore, the imbalance caused in the DC currents of cable H2 previously is removed. Furthermore, this controller was tested for a positive and negative PG fault for different locations on cable H2. Likewise, the investigation was extended for a capacitive, inductive, and resistive DC fault. Under these scenarios, the controller suppresses the return path current as it does in the case of a positive PG fault. Therefore, these scenarios' return path current plots are similar to Fig. 3.3.

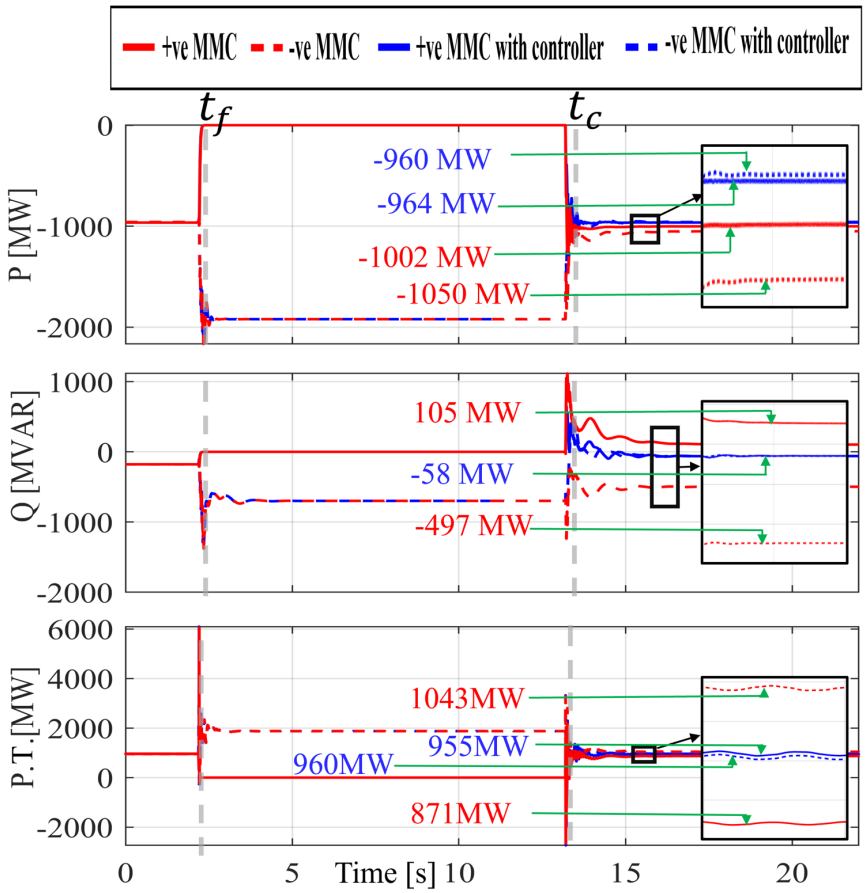

Figure 3.4: MMC2 parameters with and without the controller: (a) MMC2 active power, (b) MMC2 reactive power, and (c) power transferred through cable H2.

4

MMC control strategies: grid forming and grid following controls

After discussing the network and the DC fault current controller for the metallic return(Since this is for the metallic return, the controller is also categorized as a part of the network and not as a part of the controls in the previous chapters, this chapter discusses the control strategies implemented in the network. With the increase in the penetration of renewable energy sources into the power grid, the number of power converters in the electrical grid has increased significantly. Control algorithms/strategies are used to warrant these power converters' proper/regular operation [57]. Depending on the control strategies and their operation in the grid, power converters can be broadly classified into:

- Grid Following converters (GFL), Fig. 4.1a;
- Grid Forming converters (GFM), Fig. 4.1b.

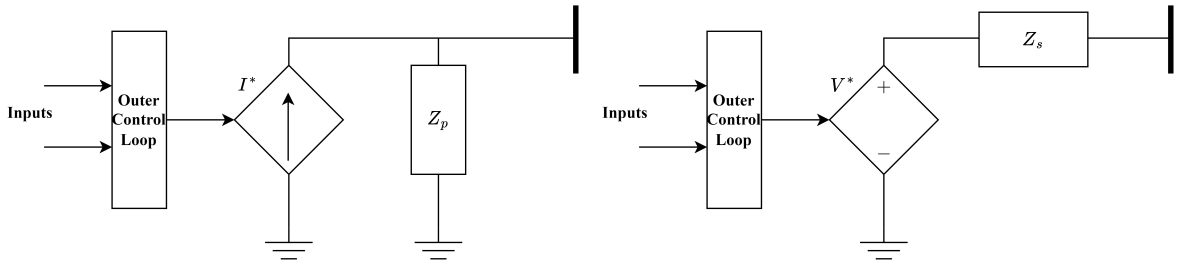

(a) Equivalent of grid following

(b) Equivalent of grid forming

Figure 4.1: Equivalent circuits of the control of power converters.

4.1. Grid following control

Grid-following converters are designed to supply active and reactive power to the grid or loads and can be represented as a current-controlled source with high parallel impedance. However, one of the drawbacks of these converters is that they require perfect synchronization with the AC voltage of the grid at the Point of Common Coupling (PCC) to regulate the exchange of active and reactive power accurately. This is achieved using the Phase-Locked Loop (PLL) to synchronize with the grid frequency. However, this synchronization process can lead to instability problems when the grid weakens. In such cases, the PLL may be unable to maintain synchronization, leading to fluctuations in the exchanged power and affecting the system's stability [47]. To operate correctly, grid-following converters need an external source to form the grid voltage at the PCC, and they cannot function in islanded mode. The operation of the grid following converters is often regulated by a high-level controller (outer control loop) like a Maximum Power Point Tracking (MPPT) controlled or a power plant controller, which sets the reference values of either P^*[1], V^*_{dc}, Q^* and V^*_{ac}. The inner control loop controls and regulates currents injected into the grid by controlling the i_d and i_q currents [57]. A schematic of the control strategy is shown in Fig. 4.2. Grid-following converters depend on the grid's stability and strength with

[1] X^* denotes the reference value (setpoint) of X

which they are connected. With the growing number of renewable energy sources and the decrease in synchronous generators, which are a significant factor in creating a robust grid, these converters may not be suitable for future use [83].To address these issues, various techniques, such as adaptive PLLs, frequency estimation methods, and grid-forming control strategies, have been proposed to enhance the stability of the VSC system under weak grid conditions.

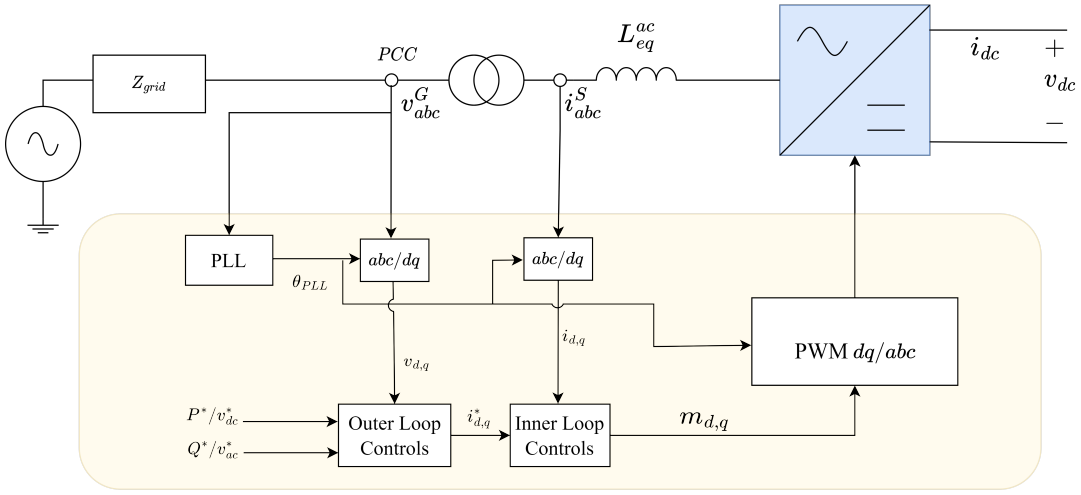

Figure 4.2: Grid following control loop schematic diagram.

4.2. Grid forming control

This control strategy is a relatively new strategy which is not been implemented in real-life transmission networks but will be in the near future. Grid-forming converters can be represented as a voltage-controlled source with low series impedance. They are mainly designed to set the grid voltage and frequency at the PCC. These voltage source converters need not be perfectly synchronized with the AC voltage of the grid as they generate their phase angle and, therefore, can operate in islanded mode. The operation of the grid-forming converters is often regulated by a voltage reference V^*_{AC} (outer loop) and frequency set points. This control strategy usually does not require an inner current($i_{d,q}$) control if additional protection equipment is already present in the network. But, if inherent current limitation (over-current protection) is required, an inner control loop, similar to the one in the grid following control, can be added [57]. Fig. 4.3 gives the grid forming control strategy schematic. Two of the most

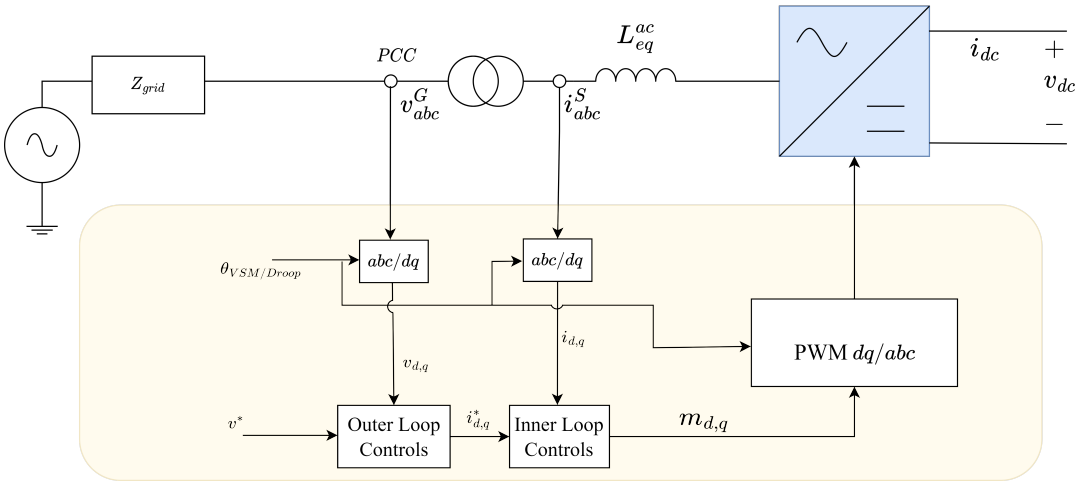

Figure 4.3: Grid forming control loop schematic diagram.

common grid forming control topologies have been implemented and tested[42]; Virtual Synchronous

Table 4.1: A Brief Overview of the Control Strategies that will be discussed

Control Strategy	Mode	Input parameters	Equations
Grid Following	Contant V_{dc}	$V^*_{dc}(t)$	$V_{dc,err}(t) = V^*_{dc}(t) - V_{dc}(t)$
	$V_{dc} - P$ droop	$V^*_{dc}(t), P^*(t)$	$V_{dc,err}(t) = V^*_{dc}(t) - m_k\left(P(t) - P^*(t)\right)$
Grid Forming	VSM	$P^*(t), H, K_d, \omega_{base}$	$2H\frac{d\omega_{VSM}}{dt} = P^*(t) - P(t) + K_d\left(\omega_{VSM} - \omega_{base}\right)$
	GFM Droop	$P^*(t), m_p$	$\frac{d\theta_{Droop}}{dt} = \omega_{Droop} = \omega^* - m_p\left(P(t) - P^*(t)\right)$

Machine (VSM) and Grid forming Droop (GFM Droop) control. Both of these topologies, VSM and GFM Droop, are depicted in the form of schematics in Fig.4.4 and Fig. 4.5. The two aforementioned topologies are primarily responsible for producing the phase angle (θ) imperative for the dq transformation. Additionally, these topologies perform similar functions to a Phase-Locked Loop (PLL) proficiently. The governing equations of both these Grid forming control strategies are listed:

$$\Delta P = P^*(t) - P(t) = \frac{2H}{\omega_b}\frac{d^2\theta_{VSM}}{dt^2} = 2H\frac{d\omega_{VSM}}{dt}, \tag{4.1}$$

where,

$$H = \frac{J\omega^2_{base}}{2S_{base}}, \tag{4.2}$$

and J in Eq. (4.2) is the emulated moment of inertia. To add a damping term to the swing equation (Eq. (4.3)), we need to take the change in angular frequency (ω) into consideration,

$$2H\frac{d\omega_{VSM}}{dt} = P^*(t) - P(t) + K_d\left(\omega_{VSM} - \omega_{base}\right), \tag{4.3}$$

$$\frac{d\theta_{Droop}}{dt} = \omega_{Droop} = \omega^* - m_p\left(P(t) - P^*(t)\right). \tag{4.4}$$

In Eqs.(4.3) and (4.4), θ_{vsm} is the phase angle generated by utilising the VSM (Swing equation) concept, and $P - F_{droop}$ is the phase angle generated by utilising the Active power and frequency droop concept. In Fig.4.4, a modified version of the swing equation is shown, which also takes into account the grid frequency through a PLL. The weighting factor for the frequency contributed by the PLL (ω_{PLL}) is 0. Furthermore, ω_{base} is nothing but $2\pi f$, where f is the base grid frequency (50 Hz), and in per-unit, it is equal to 1.

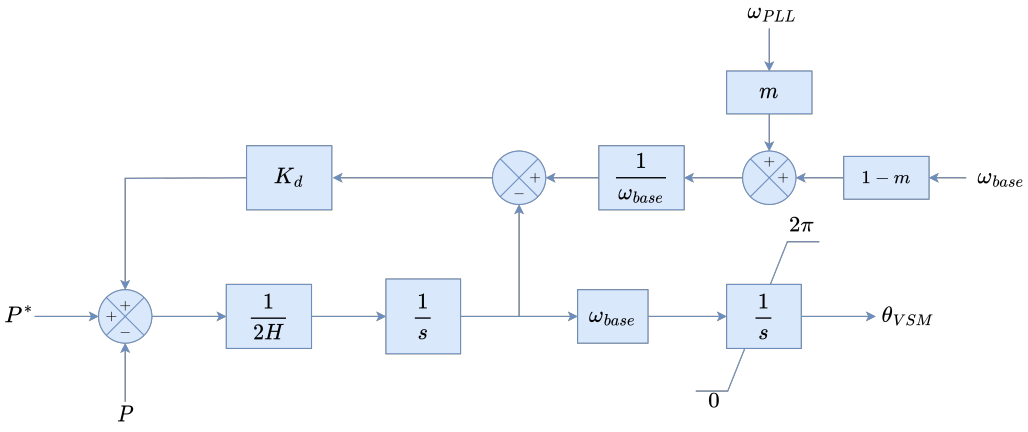

Figure 4.4: Phase angle (θ) generation using VSM.

The following sections discuss the behavior of the four terminal ±525 kV bipolar metallic return HVDC system when the MMC stations in the network are controlled with different control strategies and their combinations. Different control strategies for the converters were implemented and compared to comprehensively grasp the advantages of some control strategies over others.

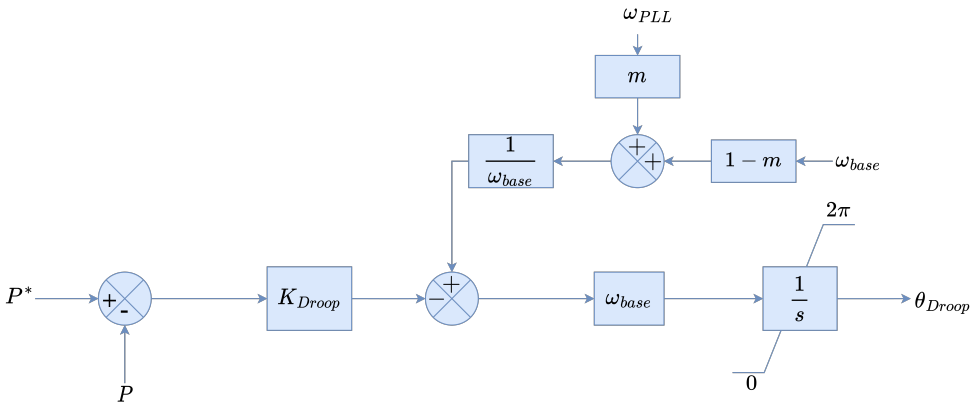

Figure 4.5: Phase angle (θ) generation using GFM Droop.

4.3. Control strategies for OWFs

In this network, the wind farm controls are divided into grid-side control and machine-side control, as is in Type 4 wind farms. The machine-side controller controls the turbine(with the PMSM), and the grid-side controller controls the chopper circuit and the transformer that steps up the voltage from 0.69 kV to 66 kV. The machine side controller (PMSM side) is divided into an inner loop controller, a phase tracking, a Park transformation, and an outer loop controller. The grid side controllers have VSC inner and outer loop controllers as well as PLL and Park Transformation.

Since the primary side voltage of the transformer that connects the MMC station to the windfarm is already being controlled by the grid forming strategy of the offshore converters, making the wind farms grid forming would mean that the secondary side of the same controller would also be controlled making it a rigid (stiff) control on the primary and secondary of the controller, and would be difficult to regulate. Therefore, the decision to leave the wind farm controls in the grid following strategy was made. Also, the wind farms' only purpose in this thesis is to provide the HVDC transmission network with a realistic power flow into the network. Hence, the controls have been left as a grid following, and not much literature study(on my part) has been done on this topic. Furthermore, the d-axis of the grid following control strategy for the grid-side converter, controls the DC link voltage between the machine-side converter and the grid-side converter. The q-axis of the same control strategy controls the reactive power injected into the offshore MMC station connected to the offshore wind farm. As for the grid following control strategy utilized for the machine side converter of the wind farm, the d component is set to 0 while the q-axis controls the torque of the PMSM.Fig.4.6 shows the typical Type 4 wind turbine schematic.

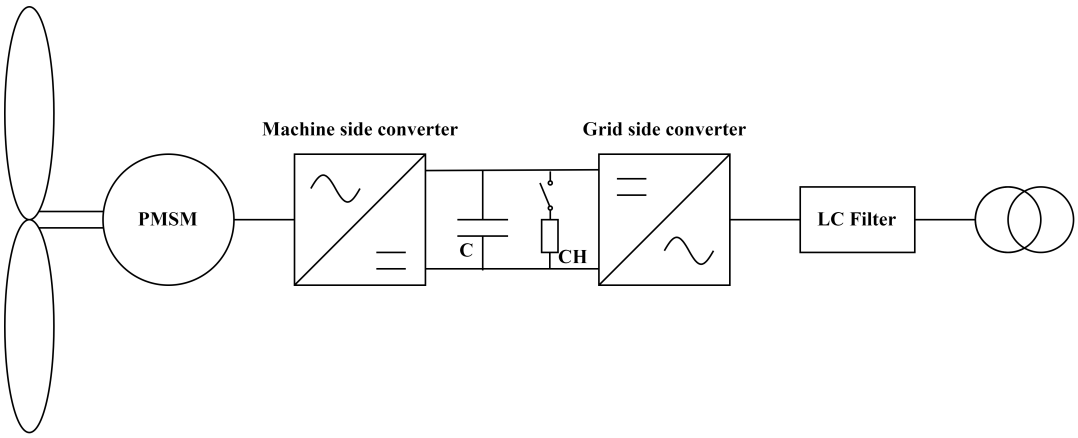

Figure 4.6: Type 4 wind turbine.

Table 4.2: Control Strategy Parameter Values implemented for MMC2 and MMC3

Parameter	Value
P^*	0.444 pu
V^*_{AC}	1
H	590 pu
T_i(outer loop)	0.1 pu
k_{pi} (outer loop)	1 pu

Table 4.3: MMC1

Onshore(MMC1) \ Offshore(MMC2)	peak Over/under shoot (pu)		settling time (s)		settled value (pu)	
	GFM VSM	GFM Droop	GFM VSM	GFM Droop	GFM VSM	GFM Droop
GFL Droop	-0.01714	-0.02286	8.142	8.757	1.002876	1.008571
GFl V_{dc}	-0.02	-0.02262	8.326	8.9436	0.998095	1.006743

4.4. Control strategies for offshore MMC stations

4.4.1. MMC2 and MMC3 control strategies

The two offshore MMC stations, namely, MMC2 and MMC3, have identical operational behavior. The control strategies implemented and tested for these converter stations are VSM and grid-forming Droop control. It was decided to implement grid forming control strategies as the transfer of power keeping the MMC terminal voltage as stable as possible was the priority for these MMC stations, and grid forming converters fulfill the intended purpose. For the test, a positive pole-to-ground fault was used on the cable H2, the cable connecting the converter station, and the DC hub.

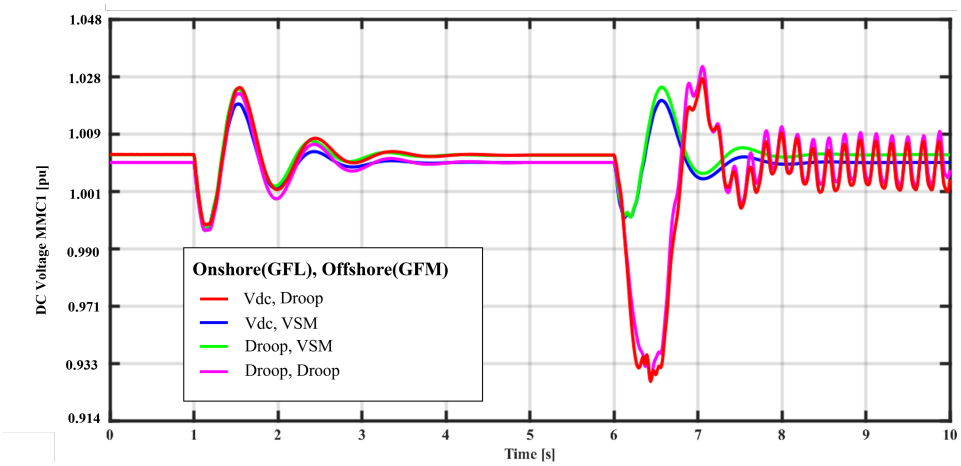

Figure 4.7: DC voltage of MMC1.

Fig.4.7 depicts the plot of the DC voltage pertaining to MMC1, and Fig.4.8 depicts the plot of the DC voltage of MMC2. Additional plots for the cable currents, active power, and reactive power of the MMCs are shown in **Appendix B** under **Section B.1**.

This analysis compared two grid-following control algorithms for the onshore converter MMC1 and two different grid-forming control algorithms for the offshore converter MMC2 and MMC3. However, only MMC2 plots are considered in this analysis for two reasons: the pole-to-ground fault was implemented on cable H2 (connecting MMC2 to the DC hub). Therefore, it would be logical to analyze only MMC2 and not MMC3 to test the control algorithm. Secondly, since the same VSM control algorithms are implemented for both MMC2 and MMC3 converters, they exhibit similar behavior (with the only difference being that the traveling waves would cause a slight disturbance, which would still be within the reasonable amount of deviations allowed but nothing major to have plots and its analysis). Also, in Fig. 4.8, there is a kink in the figure because it took more time for the curves to settle to the point just after the kink, as these are two events stitched together, i.e. the occurrence of a fault and the closure of the breaker post fault clearance. Now that the situation has become evident, the two

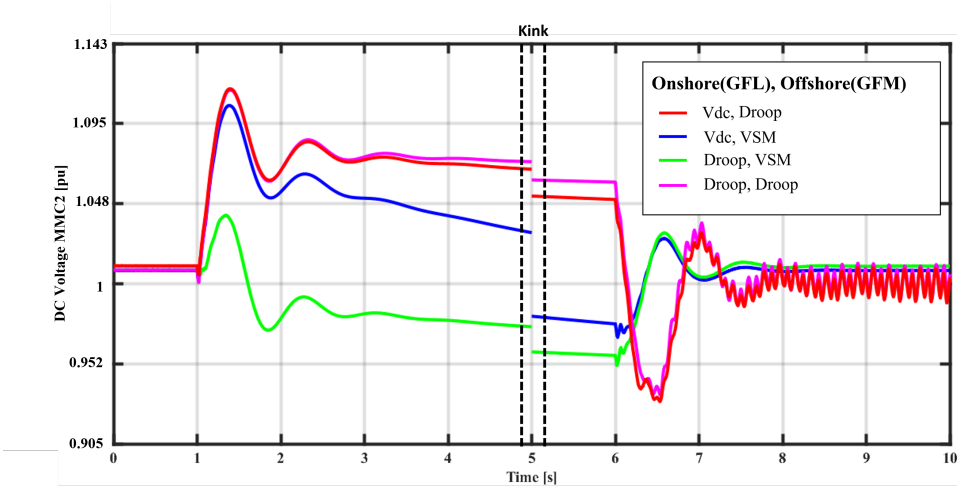

Figure 4.8: DC voltage of MMC2.

Table 4.4: MMC2

Onshore(MMC1) \ Offshore(MMC2)	peak Over/under shoot (pu)		settling time (s)		settled value (pu)	
	GFM VSM	GFM Droop	GFM VSM	GFM Droop	GFM VSM	GFM Droop
GFL Droop	0.039048	0.114286	7.9574	8.524	1.010476	1.005943
GFl V_{dc}	0.104762	0.115933	8.33682	8.654	1.00719	0.990543

grid following controls(this is further discussed in section 4.6.1) mentioned previously are constant V_{dc} and droop control($V_{dc} - P$ droop) and then the two grid forming control strategies are VSM and GFM droop($P - f$ droop),(not to be confused with the droop control mentioned previously). In all the plots in Figs.4.7,B.1,B.3,B.5,4.8,B.2,B.4 and B.6, it can be seen that $V_{dc} - P$ droop for MMC1 (GFL, Eq.(4.5)) and VSM for MMC2 and MMC3 is the best control strategy combination out of the four possible combinations of the controls presented in the figures. The reasons for this are attributed to the fact that the grid following $V_{dc} - P$ droop has a dynamic nature and hence is more compliant with rapid changes. Secondly, the VSM has virtual inertia that damps out the transient oscillations. Furthermore, Table 4.3 and Table 4.4 illustrate the difference between the control strategies and the types and control strategies, along with their combinations. The combinations that fail to settle after the clearance of the fault are indicated in red.

$$V_{dc}(t) = V^*_{dc}(t) - m_k \left(P(t) - P^*(t)\right) \tag{4.5}$$

The advantages of VSM over GFM droop, given in the literature and proved with the aforementioned transient phenomena, are [42]:

- Droop proves to be advantageous when the XBR[2] is large(highly inductive network).
- Droop control cannot achieve the normal operating setpoint after large disturbances (faults).
- For droop to have an inertial characteristic, a filter with an appropriate cutoff frequency needs to be added to the droop coefficient.

4.5. SCR of the onshore AC grid

Before proceeding any further in this thesis, it is paramount to discuss a metric used to gauge the behavior of the implemented controls, SCR. Short Circuit Ratio (SCR) is one of the ways to quantify the strength of the AC grid, which is connected to the HVDC transmission network. This can be very useful to test the ability of the control strategies implemented in onshore converters. SCR values usually range from 45 (strong grid) to 1(very weak grid). The definition of SCR used according to that of IEEE 519-2014 [29], is the ratio of short circuit current to that of load current at the PCC, which is further

[2]the amount of reactance X to the amount of resistance R, in a grid, for the distribution grid, it is high, and for a generation unit it is low

simplified below [61]: **SCR**,

$$X_{pu} = \frac{1}{SCR}$$
$$X = X_{pu} \times Z_{base}$$
$$L = \frac{X}{2\pi(f)}$$
$$R_{pu} = \frac{X_{pu}}{XBR}$$
$$R = R_{pu} \times Z_{base}$$

For all the tests (The entirety of this thesis), the XBR of the system was set to **10**.
Research has shown that the impedance of the grid is considerably high at low Short Circuit Ratios (SCRs). This high impedance significantly impacts the synchronization capabilities of the Phase-Locked Loop (PLL), which is a critical component of the grid following control strategies. As a result, grid-following converters tend to face difficulties in controlling the grid with SCRs lower than 10 [81]. Hence, SCR is utilised as one of the main factors to test the abilities of the control strategies and controllers(Chapter 6).

4.6. Onshore MMC control strategy

The onshore converter control strategy has to take into consideration the strength of the AC grid connected to it so as to not violate the grid code [51].In this section, MMC1 is chosen to utilise the grid following control strategy, and MMC4 is chosen to employ the grid forming control strategy.

4.6.1. MMC1 control strategy

In the context of a multi-terminal HVDC network, the MMC1 station plays a critical role in charging the DC Hub and, consequently, all the DC cables in the network. To maintain the DC voltage at the specified ratings for the DC cables, a grid following control strategy has been chosen to control the MMC1 station. This control strategy also provides inherent current limiting control, which is a crucial requirement for the safe and reliable operation of the network. Therefore, controlling MMC1 using GFL is a strategic decision that ensures the stability and effective management of the HVDC network[48, 59]. In addition to the aforementioned benefits, controlling the MMC1 station using a grid following control algorithm provides a unique opportunity to test the interoperability of different converter control algorithms in the HVDC network[38]. Since the network design comprises of four converter stations, each with its own control algorithm, it is essential to ensure that these control strategies can work together seamlessly to maintain the stability and reliability of the network. The use of a grid following control strategy for MMC1 enables researchers and engineers to evaluate the performance of different control algorithms and assess their compatibility with each other. This testing is critical to ensure the HVDC network's successful operation and identify any potential issues that may arise due to the interaction of different control algorithms. Integrating the latest control strategies in the newly added stations of the MTDC network with the already established stations with traditional control strategies enables grid design engineers to leverage the existing operational stations while implementing advanced control strategies. This approach ensures a seamless transition to modern control strategies without disrupting the existing infrastructure [70].

There must be a fixed reference for the offshore DC cable network, as the DC cables are rated at 525kV. Furthermore, all other network elements, like the transformers, are rated at 400/275 kV. With a buffer margin that is present to account for transient over-voltages during fault conditions. Therefore to maintain the DC voltage, the V_{dc} (direct current Voltage) mode of the Grid following the control strategy is used as it sets the reference voltage for the cables and the DC network. Another advantage of utilizing the grid following control strategy is the inherent current limiting capabilities that this control strategy has over other control strategies [60]. Another grid following topology implemented for the onshore MMC stations is the Vdc-Droop control, which offers a dynamic change in stable operating points during transient phenomena. These control modes are tested using the SCR metric against different transient events.

Table 4.5: Control Strategy Parameter Values implemented for MMC1

Parameter	Value
V_{DC}	1 pu
P^*	-0.4 pu
V^*_{AC}	1
Q^*	0 pu
T_i(outer loop)	0.5 pu
k_{pi} (outer loop)	5 pu
T_v (inner loop)	0.1 pu
k_{pv} (inner loop)	1 pu
k_{Droop} (inner loop)	0.01 (MW/kV)

Table 4.6: Control mode performance for three-phase AC fault, based on the AC grid voltage waveforms of MMC4

SCR	Sag (pu)		settling time (s)		settled value (pu)	
	V_{dc} **droop**	**Constant** V_{dc}	V_{dc} **droop**	**Constant** V_{dc}	V_{dc} **droop**	**Constant** V_{dc}
45	-0.851	-0.85	0.37	0.3819	1.00125	1.0013
35	-0.8752	-0.874	0.385371	0.3977	1.00171	1.0006
20	-0.9265	-0.94	0.4195	0.42698	1.0032	1.00006
10	-0.9586	-0.962	0.44226	0.461727	1.00632	1.00082

The three transient phenomena while, at the same time, varying the SCR of the AC grid (i.e., the strength of the AC grid will be varied to observe the impact of the transient phenomena on the dynamic behavior of the control strategy and, in turn, the network as a whole) [2]. The three transient phenomena are:

- Three-phase AC fault on the PCC between the AC grid and the converter station.
- a positive pole to ground fault on cable H2 (cable connecting the DC Hub to MMC2).
- a phase jump of 20° in the AC voltage to exhibit the strange behavior of the AC grid.

As mentioned earlier, the analysis of the grid following converters was only done till SCR 10 because of the loss of synchronicity of the PLL. The Voltage curve is also less stable and goes beyond the 10% margin set by the grid code. Also, during these transient events, the q-axis of the control was assigned to the reactive power (Q) control, and the reactive power set point was set to 0.

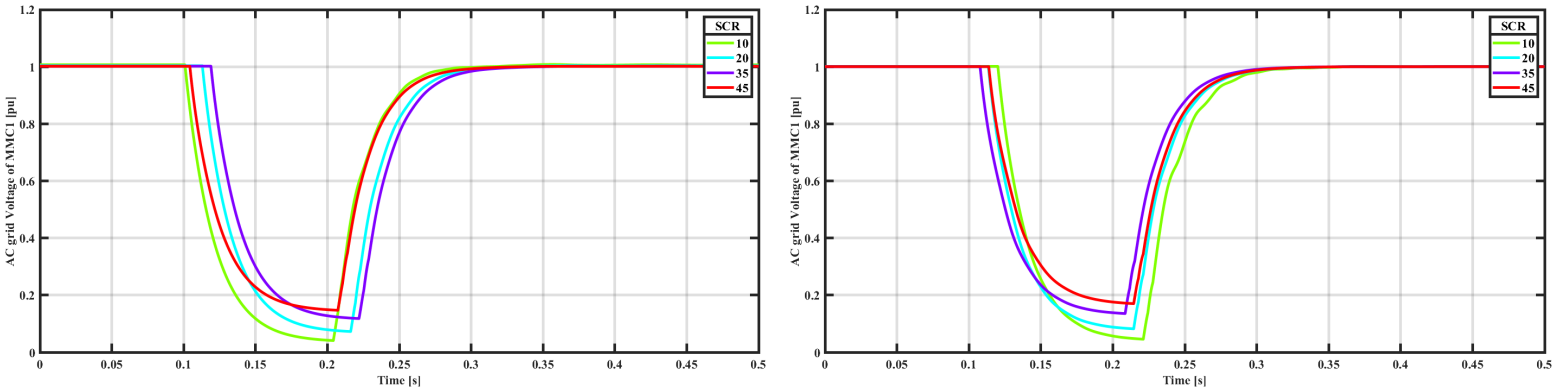

(a) V_{DC} droop GFL control strategy

(b) constant V_{DC} GFL control strategy

Figure 4.9: AC voltage of MMC1 for three-phase fault. (a) shows the V_{DC} droop GFL control strategy, and (b) shows the constant V_{DC} GFL control strategy.

As it is seen from Fig. 4.9a, when the three-phase fault occurs at 0.1 s, it is cleared in 150 ms, and as the SCR decreases, the V_rms voltage drops to a lower value though it manages to come back to its original value of 1 pu after the fault is cleared. Similar behavior is also observed in Fig.4.9b. The event of a three-phase fault yielded similar results for both control modes. Table 4.6 also indicates that both

Table 4.7: Control mode performance for pole-to-ground DC fault, based on the AC grid voltage waveforms of MMC4

SCR	peak Over/undershoot (pu)		settling time (s)		settled value (pu)	
	V_{dc} droop	Constant V_{dc}	V_{dc} droop	Constant V_{dc}	V_{dc} droop	Constant V_{dc}
45	0.00047	0.0017	0.28854	0.32016	1.0004	1.00138
35	0.00059	0.00219	0.29599	0.3362	1.00036	1.00193
20	0.00099	0.00384	0.315	0.36078	1.00051	1.00335
10	0.00192	0.00757	0.3793	0.3844	1.00113	1.00624

Table 4.8: Control mode performance for phase jump in AC grid voltage, based on the AC grid voltage waveforms of MMC4

SCR	peak Over/undershoot (pu)		settling time (s)		settled value (pu)	
	V_{dc} droop	Constant V_{dc}	V_{dc} droop	Constant V_{dc}	V_{dc} droop	Constant V_{dc}
45	0.00163	0.00285	0.230832	0.252126	1.00115	1.00157
35	0.00208	0.0036	0.248472	0.269451	1.00069	1.00193
20	0.00357	0.00636	0.2629	0.2834	1.00042	1.00336
10	0.00689	0.01233	0.288	0.3	1.00029	1.006

the control modes react in a similar manner for three-phase AC faults.
The effect of SCR Variation is more apparent in Fig. 4.10a when a pole-to-ground fault is imposed on

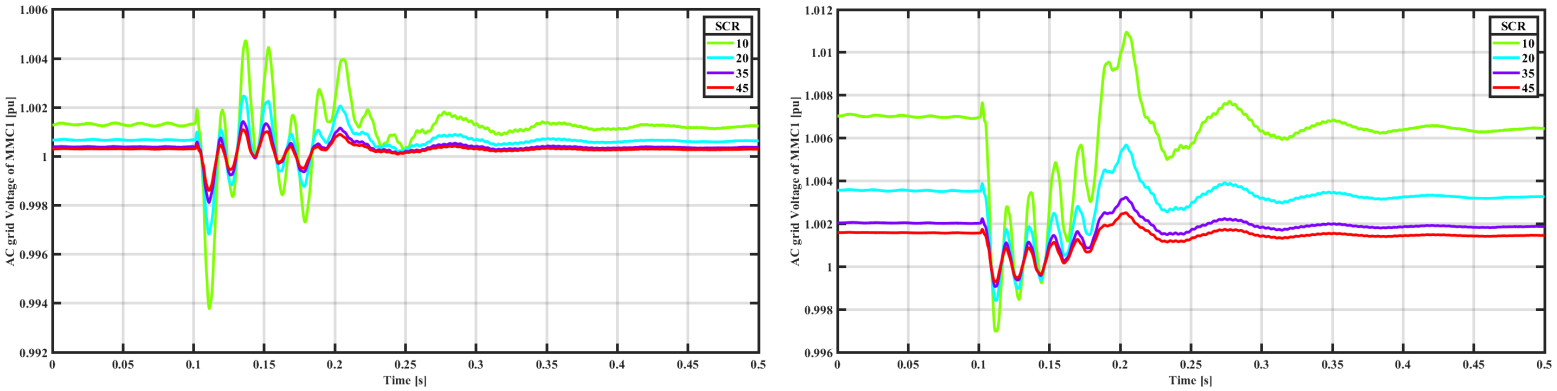

(a) V_{DC} droop GFL control strategy

(b) constant V_{DC} GFL control strategy

Figure 4.10: AC voltage of MMC1 for pole-to-ground DC fault. (a) shows the V_{DC} droop GFL control strategy, and (b) shows the constant V_{DC} GFL control strategy.

the midpoint of cable H2. This plot clearly shows that the V_{rms} deviates from its set point as the SCR decreases. Even though the deviations are still within the 10% voltage buffer. It deviates further when the SCR is further reduced. Here too, it is seen that the fault occurs at 0.1s and is cleared in 100ms.This plot also shows that when the SCR reduces, the Voltage drops to an even lower value, and the voltage overshoots on the fault's clearance becomes higher. Similar phenomena can also be seen in Fig. 4.10b, but in this control mode, the transient peaks are higher than that of V_{DC} droop control mode(Fig. 4.10a). The post-transient value is also different from the set point for the case of the constant V_dc control mode. The lower peaks can be attributed to the dynamic nature of the V_{DC} droop control mode. Table 4.7 corroborates the information discussed, providing a visual representation that reinforces the previously mentioned points.

Similar phenomena are realized in Fig. 4.11a, the V_rms values deviate from the setpoint on the reduction of the SCR, and the voltage peaks(spikes) increase height in the event of a phase jump of 20° at 0.1s.In this case, during the oscillation, Fig. 4.11a has a much lower peak than that in Fig. 4.11b. It can also be seen that the post-transient values in Fig. fig:psfgflconvdc are not similar to their set points. This analysis shows that the V_{DC} droop control mode performs much better than the constant V_{DC} control mode. Table 4.8 corroborates the information discussed, providing a visual representation that reinforces the previously mentioned points.

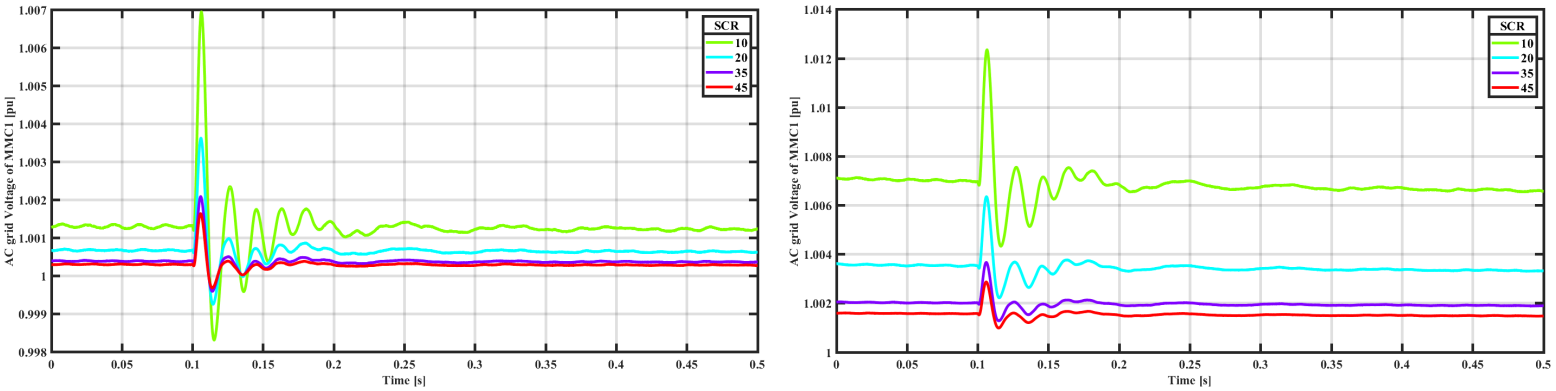

(a) V_{DC} droop GFL control strategy

(b) constant V_{DC} GFL control strategy

Figure 4.11: AC voltage of MMC1 for phase jump in AC grid voltage. (a) shows the V_{DC} droop GFL control strategy, and (b) shows the constant V_{DC} GFL control strategy.

Table 4.9: Control Strategy Parameter Values implemented for MMC4

Parameter	Value
V_{DC}	1 pu
P^*	-0.68 pu
V^*_{AC}	1
Q^*	0 pu
H	5 pu
k_d	700 pu
T_i(outer loop)	0.2 pu
k_{pi} (outer loop)	10 pu
T_v (inner loop)	0.25 pu
k_{pv} (inner loop)	0 pu

4.6.2. MMC4 control strategy

The control strategy implemented for MMC4 is a grid forming control in the form of a modified VSM to test its operation in onshore converter stations. For the converter station to achieve the transfer of power from cable H4 to the AC grid connected to MMC4, the normal VSM control strategy needs to be modified before it can be implemented. This is done so that there can be a limit on the current injected into the grid and also to improve the power factor of the MMC station. This modification is derived from [20, 54], which exhibits current limiting control(a drawback of grid-forming control algorithms). This modification involves using a virtual filter capacitor C_f to decouple the voltage control loop and implement a current limiting algorithm similar to that in a grid following a control strategy. Among these additions to the existing grid forming control, a transient current damper is also implemented to dampen the transient oscillation in the current during faults or other transient phenomena. the schematic of the control loop is shown in Figs.4.12, 4.13 and 4.14.

As seen from Figs.4.15b and 4.15d, the grid-forming strategy's performance is exemplary compared to that of the grid-following strategy seen in Figs. 4.15a and 4.15c.It is seen that the modified VSM is optimal in damping the oscillations in the V_rms plots even at Lower SCRs. The V_rms waveforms at lower SCRs revert back to their set points after the fault is cleared without many oscillations or perturbations. As seen previously, the voltage dip gets deeper as the SCR reduces. Table4.10 corroborates the information discussed, providing a visual representation that reinforces the previously mentioned points. As seen from Figs.4.16b and 4.16d, the behavior of the RMS voltage with the grid-forming strategy is exemplary compared to that seen in Figs. 4.16a and 4.16c.Once again, It can be seen that the modified VSM is optimal in damping the oscillations in the V_rms plots even at Lower SCRs. The V_rms waveform has consistently lower overshoot peaks at all the SCRs testes against that of the waveforms plotted for the grid following strategy. Table 4.11 corroborates the information discussed, providing a

[3]Still oscillating, therefore first peak after clearance of fault

Table 4.10: Control strategy performance for three-phase AC fault, based on the AC grid voltage waveforms of MMC4

SCR	Sag (pu)		settling time (s)		settled value (pu)	
	GFL	GFM	GFL	GFM	GFL	GFM
35	-0.86	-0.85	0.31	0.34	1.005	0.994
20	-0.92	-0.915	0.315	0.35	1.02177	0.99
10	-0.95	-0.948	0.32	0.38	1.02177	1.03
9	-0.957	-0.953	0.36	0.384	1.023	1.023
8	-0.96	-0.958	0.36	0.384	1.026	1.029
7	-0.964	-0.963	0.37	0.385	1.0305	1.033
6	-0.968	-0.965	0.39	0.387	1.03571	1.05
5	-0.97	-0.9721	0.41	0.387	1.041	1.056
4	-0.975	-0.973	0.429	0.39	1.049	1.064
3	-0.98	-0.977	0.429	0.39	1.051	1.067
2	-0.983	-0.98	-	0.39	1.13[3]	1.11

Table 4.11: Control strategy performance for pole-to-ground DC fault, based on the AC grid voltage waveforms of MMC4

SCR	peak Over/undershoot (pu)		settling time (s)		settled value (pu)	
	GFL	GFM	GFL	GFM	GFL	GFM
45	0.00032	0.00012	0.1866	0.245	1.00012	1.00026
35	0.00038	0.0002	0.1856	0.25	1.0002	1.00072
20	0.00047	0.0003	0.248031	0.253	1.0054	1.0002
10	0.00067	0.00039	0.257418	0.26	1.00014	1.0001
9	0.00067	0.00056	0.315063	0.2706	1.00022	1.0006
8	0.00069	0.0006	0.317016	0.2777	1.0002	1.0004
7	0.0072	0.00066	0.318591	0.284	1.00017	1.0008
6	0.00075	0.00068	0.318553	0.296	1.00018	0.999
5	0.0008	0.00072	0.319788	0.303	1.00015	0.9999
4	0.0008	0.00082	0.37774	0.31	0.99999	1.00019
3	0.00104	0.001	0.385	0.431	0.9999	0.999
2	0.00139	0.0012	0.457	0.482	1.001	1

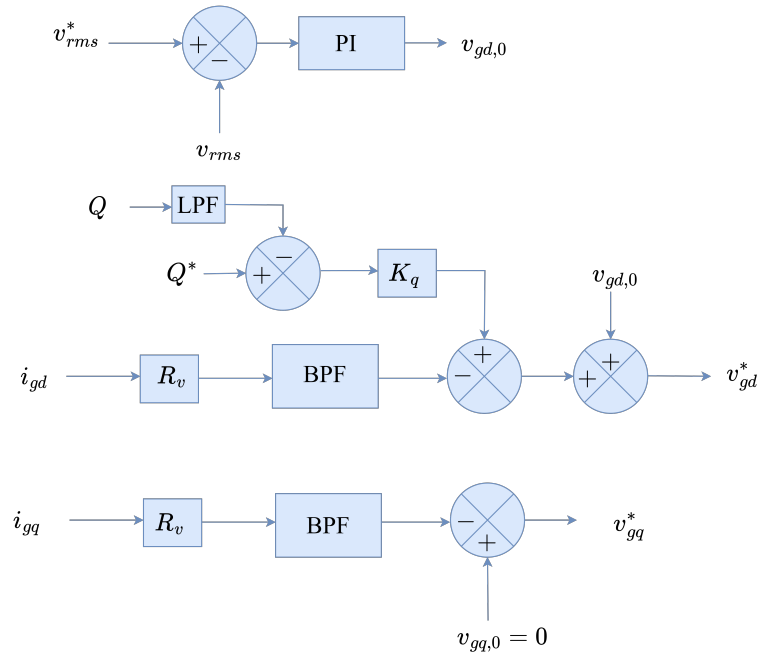

Figure 4.12: Outer loop of the modified grid forming control strategy used in MMC4.

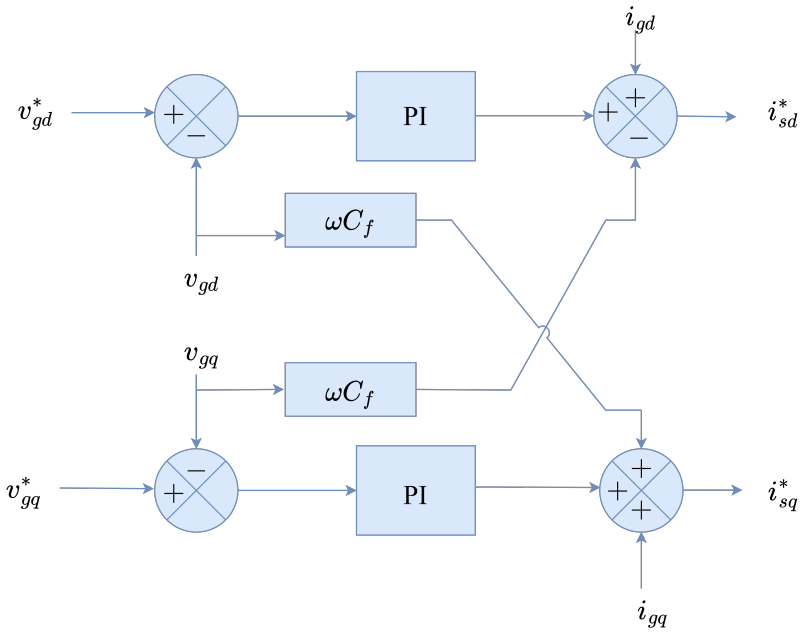

Figure 4.13: Intermediate loop of the modified grid forming control strategy used in MMC4.

visual representation that reinforces the previously mentioned points.

As seen from Figs. 4.17b and 4.17d, the behavior of the V_rms with the grid-forming control strategy is much superior to that seen in Figs. 4.17a and 4.17c. The peaks in these figures during the phase jump are much smaller than Grid following control. The Lower SCR Figs.4.17d and 4.17c show that after the event subsides, the V_rms values revert to 1pu in the case of grid forming while in the case of the grid-following control, the V_rms values settle to a value that is lower than its set point value. As can be seen, the damping capabilities of the VSM also allow the V_rms to return to their original value by

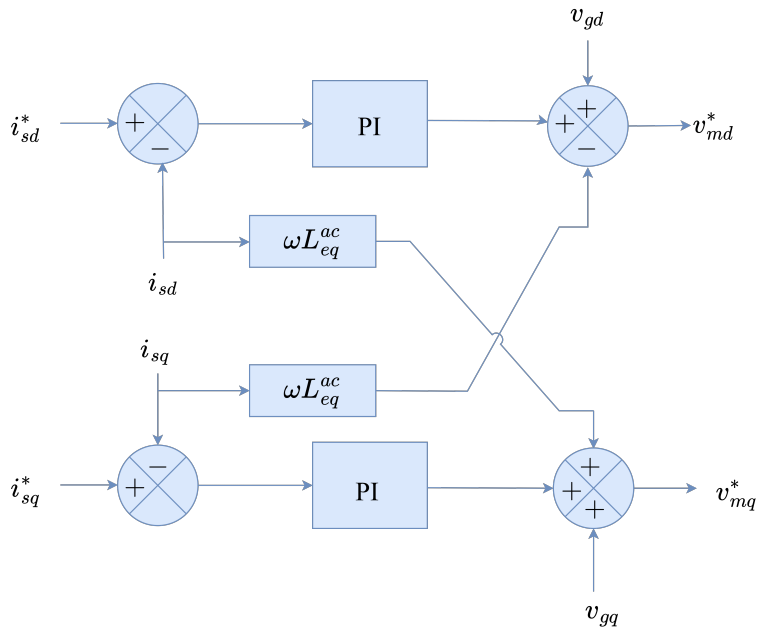

Figure 4.14: Inner loop of the modified grid forming control strategy used in MMC4.

damping the oscillations thoroughly. Table 4.12corroborates the information discussed, providing a visual representation that reinforces the previously mentioned points.

Table 4.12: Control strategy performance for phase jump in AC grid voltage, based on the AC grid voltage waveforms of MMC4

SCR	peak Over/under shoot (pu)		settling time (s)		settled value (pu)	
	GFL	GFM	GFL	GFM	GFL	GFM
45	0.0027	0.00137	0.1498	0.212	1.0007	1.00022
35	0.003	0.00165	0.15624	0.2158	1.0008	1.00021
20	0.063	0.00263	0.157878	0.243	1.00126	1.0012
10	0.063	0.005	0.245	0.2457	1.00006	1.00017
9	0.063	0.00549	0.272	0.2509	1.0003	1.0016
8	0.063	0.0061	0.273	0.2568	1.004	1.0006
7	0.063	0.00672	0.274	0.279	1.00003	1.00002
6	0.063	0.0077	0.275	0.292	1.0002	1.0002
5	0.063	0.009	0.274	0.2949	1.0001	0.9999
4	0.063	0.0108	0.277	0.3069	1.0007	0.9999
3	0.063	0.01339	0.2903	0.323	1.00167	0.9999
2	0.063	0.0177	0.38	0.415	0.9951	0.9999

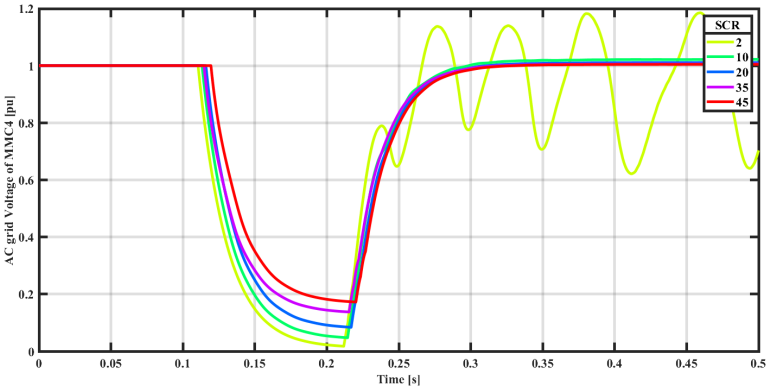

(a) GFL

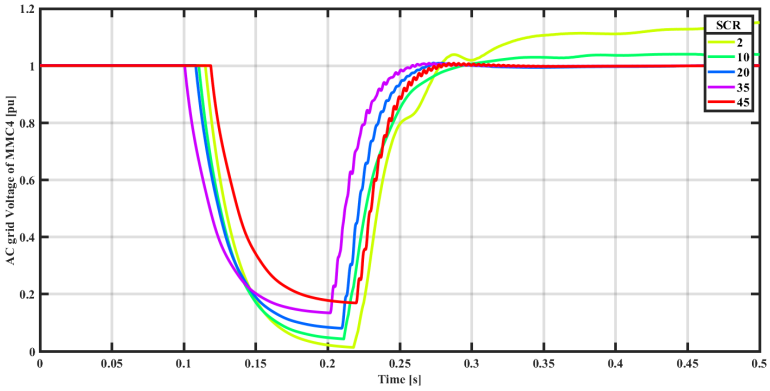

(b) GFM

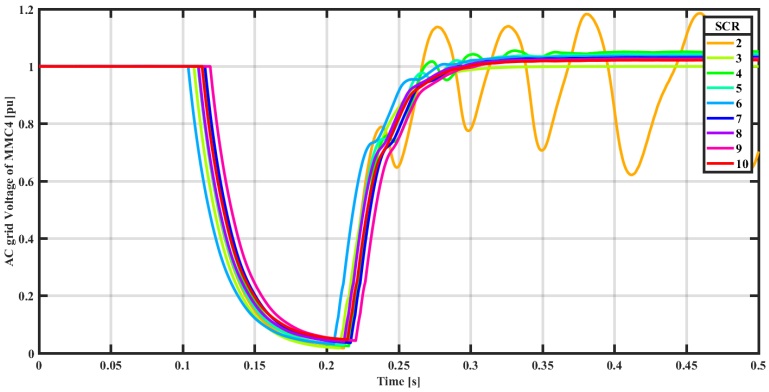

(c) GFL, for low SCRs

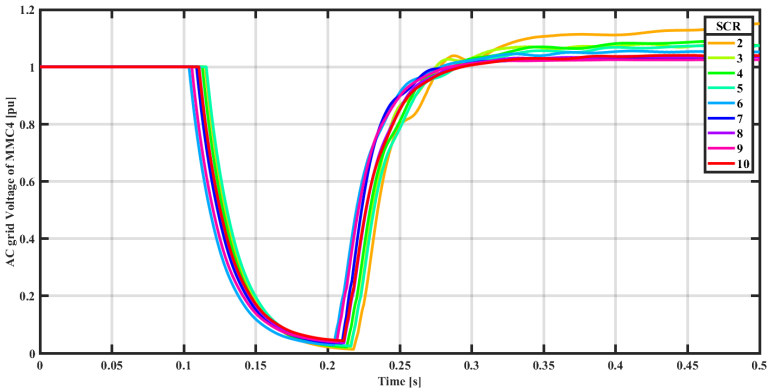

(d) GFM, for low SCRs

Figure 4.15: AC voltage behavior during a three-phase AC fault. (a) GFL for average SCRs, (b) GFM for average SCRs, (c) GFL for low SCRs, (d) GFM for low SCRs.

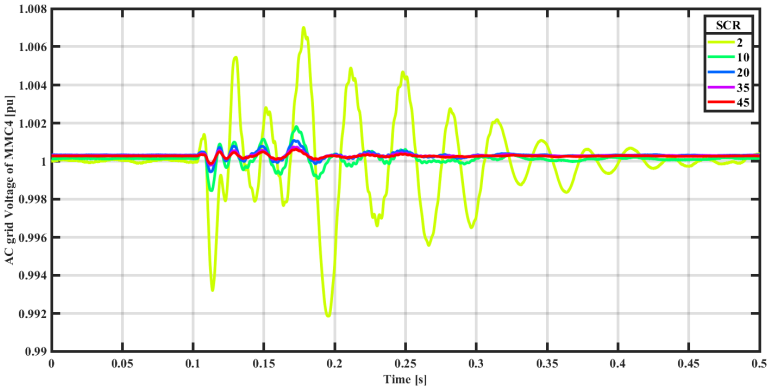

(a) GFL

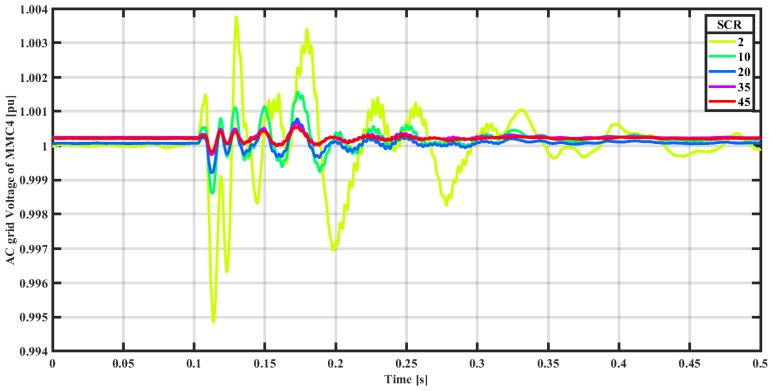

(b) GFM

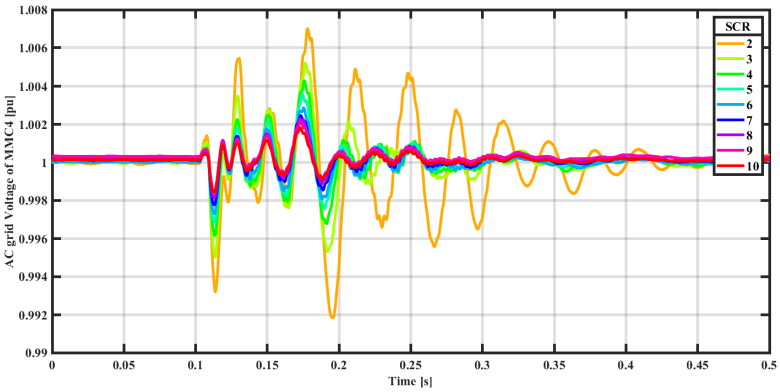

(c) GFL, for low SCRs

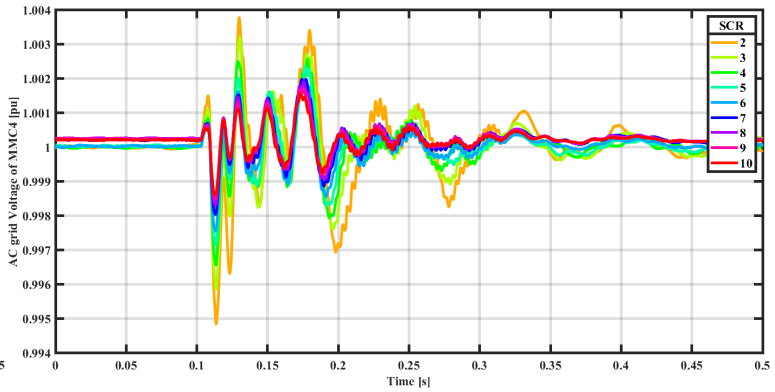

(d) GFM, for low SCRs

Figure 4.16: AC voltage behavior during a pole-to-ground DC fault. (a) GFL for average SCRs, (b) GFM for average SCRs, (c) GFL for low SCRs, (d) GFM for low SCRs.

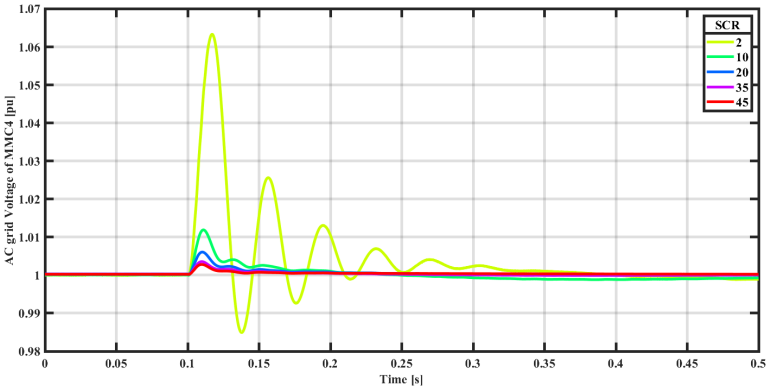

(a) GFL

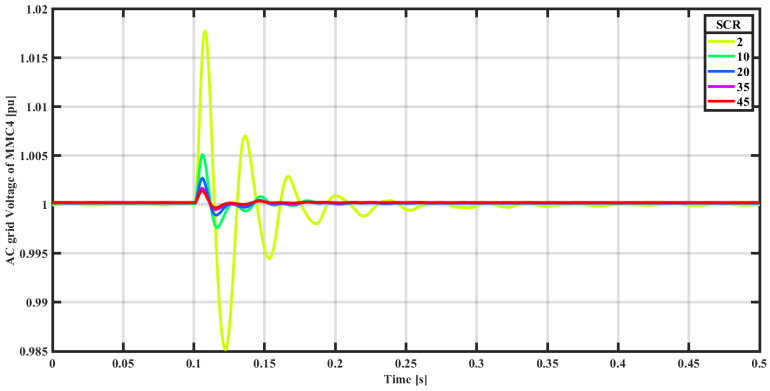

(b) GFM

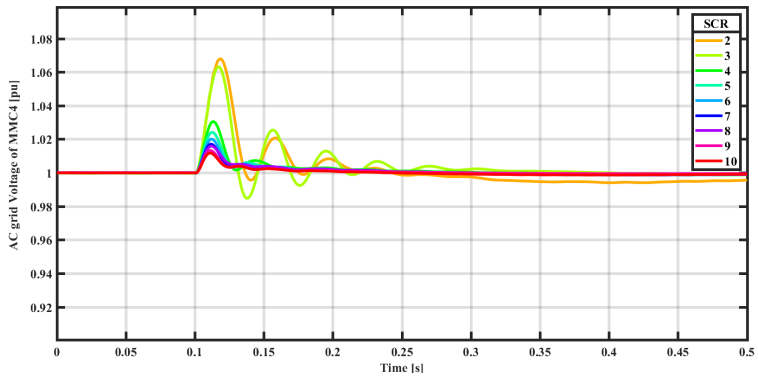

(c) GFL, for low SCRs

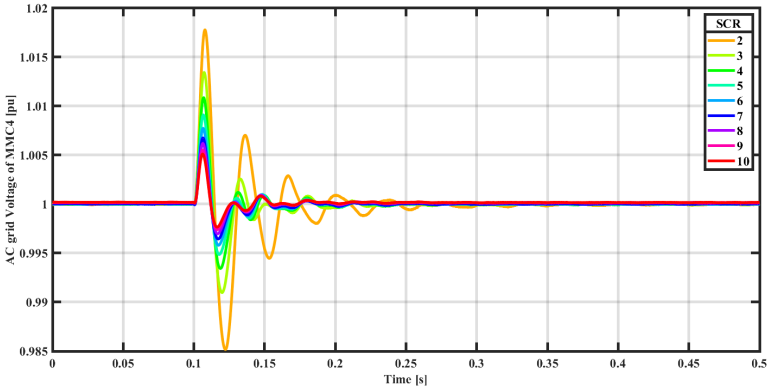

(d) GFM, for low SCRs

Figure 4.17: AC voltage behavior during a phase jump in AC grid Voltage. (a) GFL for average SCRs, (b) GFM for average SCRs, (c) GFL for low SCRs, (d) GFM for low SCRs.

5
Circulating current suppression control (CCSC)

The circulating current of the MMC is an internal characteristic of the converter which circulates in the arms and is a result of variations in the total SM capacitor voltage in each arm of the converter legs [49]. This current does not leave the converter but causes a lot of unwanted disturbances in the normal working of the converter and, at times, may even lead to instabilities. .The dynamics of the supposed Circulating current in the MMCs are governed by (5.1),

$$L\frac{\mathrm{d}i_{\mathrm{c}}}{\mathrm{d}t} = \frac{V_{\mathrm{dc}}}{2} - V^{*} - Ri_{\mathrm{c}} \Rightarrow i_{\mathrm{c}} = \frac{1}{sL_{\mathrm{arm}} + R_{\mathrm{arm}}}\left(\frac{V_{\mathrm{dc}}}{2} - V^{*}\right), \tag{5.1}$$

where V^{*} is the voltage reference, which is usually set to 1 pu to fix the value, but in reality, it is given by an exponential term and a parasitic delta term. As can be seen from (5.1), the amplitude of this current depends on the Arm impedances. As the arm inductance increases, the amplitude of the circulating currents decreases. However, despite the increase in arm inductance, circulating currents are not completely reduced, which is inefficient in terms of the cost-benefit analysis. Thus, a control method for circulating currents is necessary [49]. MMCs commonly use a circulating current suppression control (CCSC) to minimize this. This circulating current consists of the negative sequence of the second harmonic (-2ω).A component of the circulating current is also related to the DC current of the MMCs, making the control of the same very crucial to transfer the guaranteed active power[18].

The converter arms possess a distinctive current, predominantly governed by the second-harmonic, due to a specialized control system for circulating current. This system guarantees the continuous regulation of arm currents to prevent any breach of semiconductor specifications.

5.1. Importance of circulating current suppression control

Arm balancing control of the MMCs encompasses regulating circulating current. This control technique is employed within voltage control strategies to determine the insertion indices for the Pulse Width Modulation (PWM) schemes of the MMCs [74]. The unique topological structure of an MMC can cause issues such as unbalanced capacitor voltage and interphase circulating current. The inner current control loop typically uses an AC current feedback control method to address this. However, this method cannot fully represent the information about the internal circulating current in the MMC, so an additional circulating current controller must be designed. The alternating circulating current in the MMC results in the bridge arms' current distortion, worsens the SM voltage fluctuations, and increases system loss[37]. Additionally, it can lead to electromagnetic interference. [14]. The following are a few more limitations of the circulating current in the MMC:

- Reducing losses: In an MMC, circulating currents can lead to additional losses and reduce the overall efficiency of the converter. The losses can be minimized by suppressing these circulating currents, leading to a more efficient converter [15].
- Improving reliability: Circulating currents can also cause unbalanced voltage and current distributions among the SMs in the MMC, increasing stress on the capacitors and switching devices. Suppressing these circulating currents can help to reduce this stress and improve the reliability of the converter [14].

- Meeting grid codes: Many grid codes require that the voltage and current harmonics injected by power converters be kept within specified limits. Circulating currents can contribute to these harmonics, and suppressing them can help ensure grid code compliance.
- Enhancing dynamic performance: Circulating currents can also lead to the suboptimal dynamic performance of the MMC, including slow voltage regulation and poor response to faults. Suppressing these circulating currents can help improve the converter's dynamic performance.

In [24], it was shown that by eliminating the circulating current, the energy of each arm naturally converges to a stable state.

5.2. Classical circulating current suppression control

The conventional CCSC utilizes a control method where the circulating currents are transformed from the abc domain to the dq domain at double the line frequency. These currents are then fed into PI controllers, which aim to control the circulating currents in the arms of the MMCs to 0. This approach is taken because oscillations and disturbances at the double-the-line frequency are canceled out in a steady state. [18].There is no closed-loop control for the third-current component (i_z^{Σ}). A unique aspect of this control strategy is that the modulation index, m_z^{Σ}, remains constant. This is due to the fact that $v_{mz}^{\Sigma *}$ is set to $v_{dc}/2$, and when obtaining m_z^{Σ} with the converters, results in $m_z^{\Sigma} = (v_{dc}/2)/(2/v_{dc}) = 1$ [63]. The output DC current of the converter is left uncontrolled with this strategy, and it is naturally adjusted to balance the AC and DC power flow [24]. Furthermore, a linear decoupling method improves the control accuracy in a two-phase rotating coordinate system [22].DC components can be obtained with a double line-frequency negative-sequence rotational reference frame based on the three-phase second-order harmonic circulating current and suppressed by proportional-integral (PI) controllers [14].

The CCSC mainly suppresses additive currents in the traditional control [68]. The currents i_{dq}^{Σ} are controlled to zero (meaning no oscillations in abc frame) [18]. For the schematic of the classical controller shown in Fig.5.1, given in Eq.(5.2) are the governing equations for the controllers.

$$\frac{d}{dt}\left(\vec{i}_{dq}^{\Sigma}\right) = -\frac{\vec{v}_{Mdq}^{\Sigma} + \left(R_{arm}I_2 - 2\omega L_{arm}J_2\right)\vec{i}_{dq}^{\Sigma}}{L_{arm}} \tag{5.2}$$

where,

$$L_{eq}^{ac} = L_r + \frac{L_{arm}}{2}, R_{eq}^{ac} = R_r + \frac{R_{arm}}{2}, J_2 = \begin{bmatrix} 0 & 1 \\ -1 & 0 \end{bmatrix}, I_2 = \begin{bmatrix} 1 & 0 \\ 0 & 1 \end{bmatrix},$$

$$i_{d,q,z}^{\Sigma} = \frac{i_{d,q,z}^{U} + i_{d,q,z}^{L}}{2},$$

$$v_{Md,q,z}^{\Sigma} = \frac{v_{Md,q,z}^{U} + v_{Md,q,z}^{L}}{2}.$$

The proposed control method transforms the abc sequence with a double line frequency(-2ω) into dq components in the rotational reference frame to determine the controlled circulating currents in each arm. However, this approach has limitations, as it cannot fully eliminate circulating currents under unbalanced voltage conditions. This is because circulating currents have negative-sequence components as well as positive-sequence and zero-sequence components. These findings suggest a need for further research to develop more effective control strategies to address all circulating current components[49].

5.3. Zero sequence circulating current.

The uncontrolled zero-sequence component of i^{Σ} may cause interactions with the DC bus and the internal capacitor voltages, potentially making the system unstable. To improve the stability of the studied system, it is proposed to add a DC current(i_z^{Σ}) control loop [18].

$$\frac{d}{dt}\left(i_z^{\Sigma}\right) = \frac{v_{dc}}{2L_{arm}} - \frac{v_{Mz}^{\Sigma} + R_{arm}i_z^{\Sigma}}{L_{arm}} \tag{5.3}$$

The reference for i_z^{Σ} is given by utilizing the change in energy(between AC power and DC power). Here ac power represents the power injected/supplied into/from the MMC station, and DC power represents the power injected into or supplied by the DC cables.

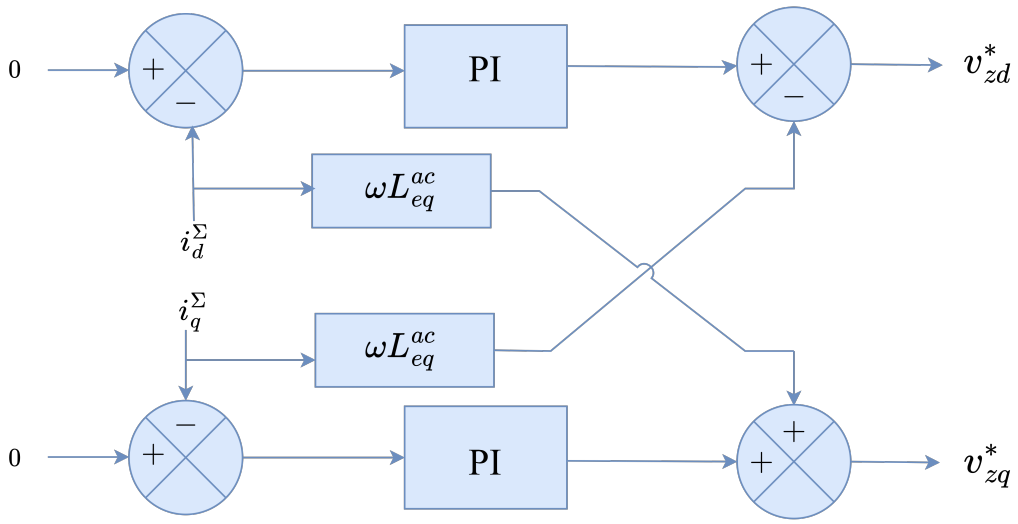

Figure 5.1: Schematic of the classical CCSC.

5.3.1. Energy based control

The outer loop used for generating this reference for i_z^{Σ} is an energy control loop. This explicit control of the total stored energy W_z^{Σ} in the MMC capacitors C_{arm} given by the power balance between AC and DC sides [62]. This strategy involves analyzing the energy change in each arm under unbalanced voltage conditions by calculating the difference between the power supplied from the DC cables and the power injected into the grid. Based on this analysis, a control algorithm is proposed to reduce circulating currents and minimize DC-link voltage ripples. [77]. This balances the power between the DC and the AC side of the MMC. The governing equations of this energy-based Circulating Current Suppression Control are given in Eqs. (5.4) and (5.6).The Eq. (5.4) gives the formula for the calculation of the Energy of the SM capacitance, which is a modified version of $C = 0.5CV^2$ but taking into account the sigma (Σ) and the delta(Δ) components in the dqz domain.

$$W_z^{\Sigma} \approx C_{arm}\left(\frac{\left(v_{Cd}^{\Sigma}\right)^2}{2}+\frac{\left(v_{Cq}^{\Sigma}\right)^2}{2}+\left(v_{Cz}^{\Sigma}\right)^2\right)+C_{arm}\left(\sum_{k=d,q,Z_d,Z_q}\frac{\left(v_{Ck}^{\Delta}\right)^2}{2}\right) \tag{5.4}$$

$$C_{arm} = \frac{6C_{SM}}{N_{SM}} \tag{5.5}$$

where N_{SM} is the number of SMs in one arm of the MMC and C_{SM} is the SM capacitance of each SM in the MMC. Furthermore, $V^{\Delta}_{CZ_d,CZq}$ are obtained using the third harmonic frequency (3ω) from 1.5 times the V^{Δ}_{CZ}:

$$\frac{dW_z^{\Sigma}}{dt} \approx P_{dc} - P_{ac} \approx \left(v_{dc}\underbrace{3i_z^{\Sigma}}_{i_{dc}}\right) - P^*_{ac}. \tag{5.6}$$

The reference of $W_z^{*\Sigma}$ is set to 1pu to maintain the MMC capacitive energy as constant. The internal energy of the MMC participates in the dynamics of the DC voltage regulation by discharging its internal capacitors into the DC bus during the transients, as seen in the voltage V_{Cz}^{Σ}. The behavior V_{Cz}^{Σ} is similar to V_{dc} as expected from the discussion in [19]. Figs.5.4, 5.5, 5.6, 5.7,5.8 and 5.9 illustrate the results for the energy-based CCSC in comparison with the classical CCSC.

As seen from Fig.5.4, the energy-based controller implemented works as expected by minimizing the circulating phase current much more effectively than the classical CCSC. The energy-based controller also keeps the sinusoidal nature of the waveform between ±0.05 pu compared to the ±0.15 pu of the classical controller. The Figs. 5.5, 5.6 and 5.7, show the dq0 components of the circulating arm current.These plots show the behavior of the currents when a pole-to-ground fault is imposed on the

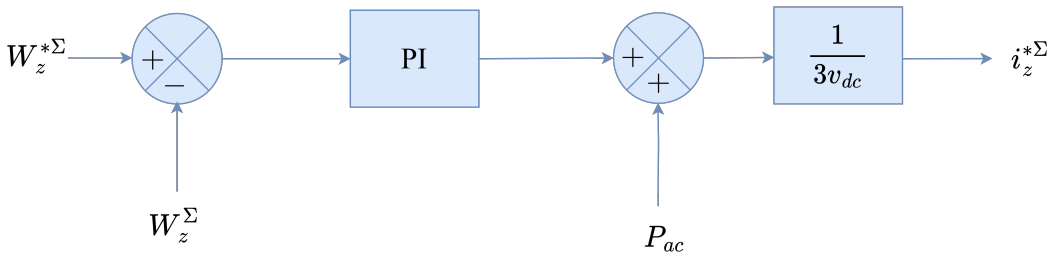

Figure 5.2: Schematic of the outer energy-based control loop.

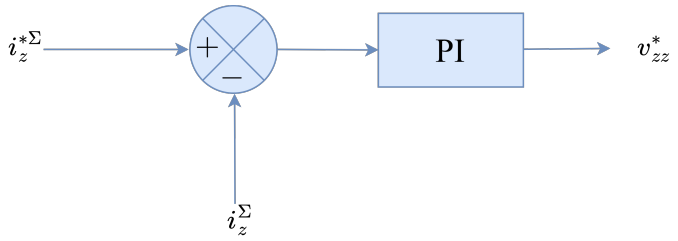

Figure 5.3: Schematic of the inner energy-based control loop.

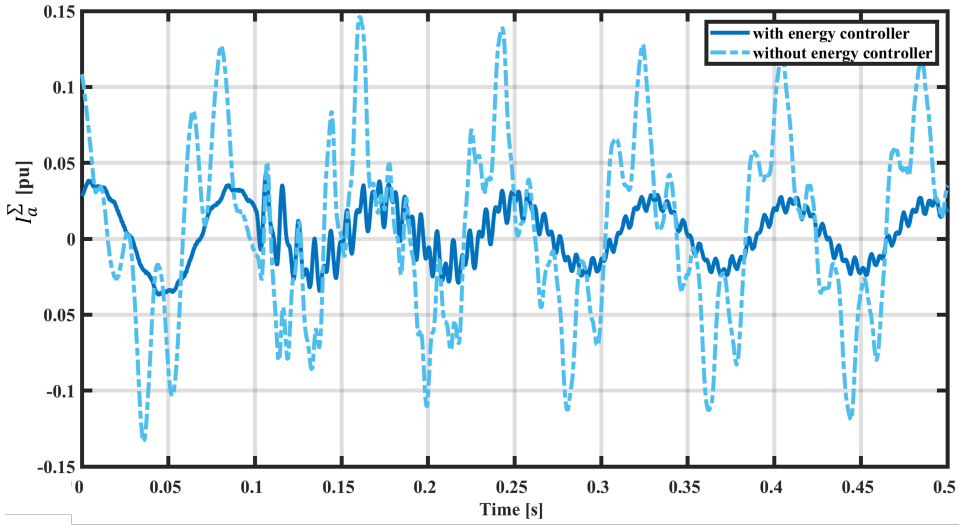

Figure 5.4: Single phase circulating current.

network at $0.1s$.These plots show that even before the fault is imposed, there are some oscillations in the waveforms of the currents with the classical CCSC, whereas, in the waveforms with the energy-based controller, the oscillations are not noticeable at all. During the fault, the behavior of both controllers is similar, but the energy-based controller waveforms illustrate superior control by minimizing the oscillations. The residual trace amounts of oscillations in the waveforms with the energy-based controller are due to the injection of the third harmonic to obtain the $V^{\Delta}_{CZ_d,CZq}$ for the formulation of the Energy

Table 5.1: Energy-based CCSC Parameter Values implemented

Parameter	Value
T_w (Energy loop)	0.1 pu
K_{pw} (Energy loop)	0.2
T_{iz}(i_z loop)	0.1 pu
k_{piz} (i_z loop)	0.2 pu

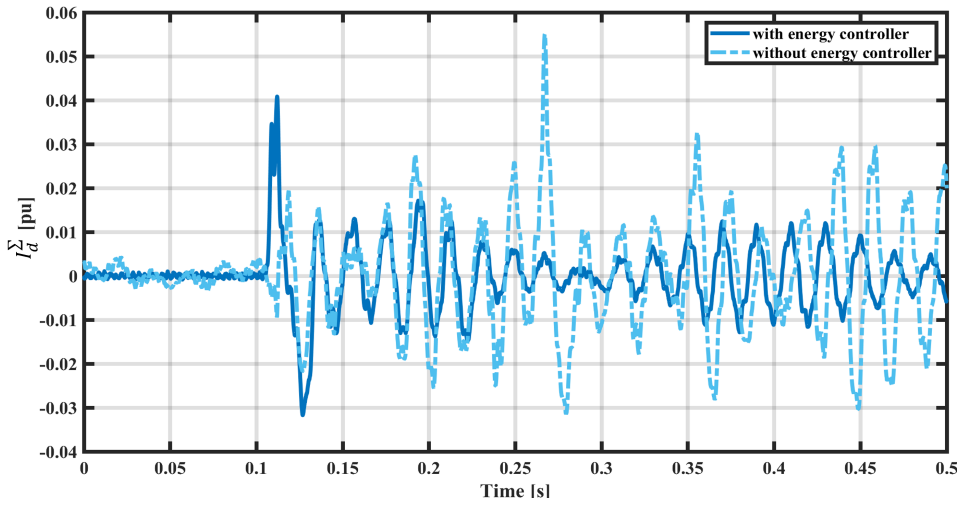

Figure 5.5: d-component of the circulating current.

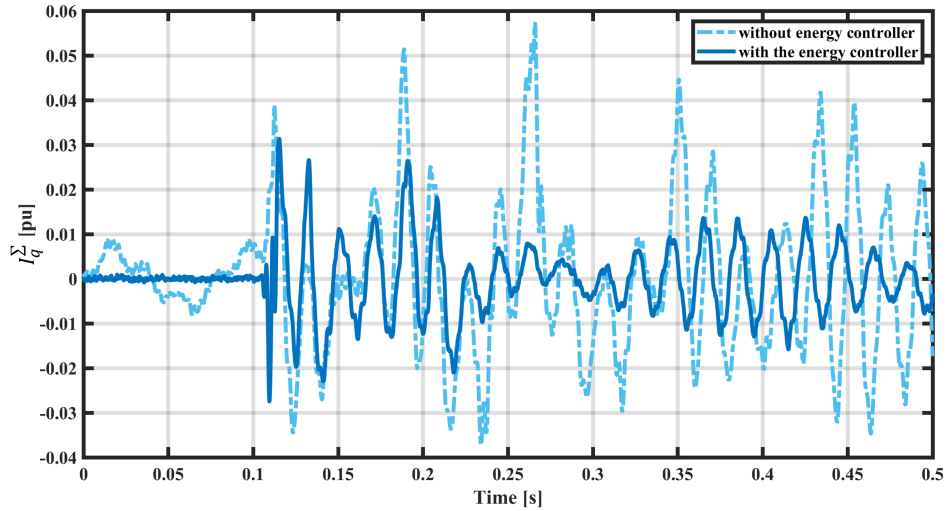

Figure 5.6: q-component of the circulating current.

function. Similar observations are made in the Figures for the SM capacitor voltages 5.8 and 5.9. Testing the effectiveness of energy control against variations in SCR may not be necessary in certain cases. For instance, further testing may yield little insights when there is an apparent discrepancy in the waveforms with and without the energy controller at a specific SCR value 45.

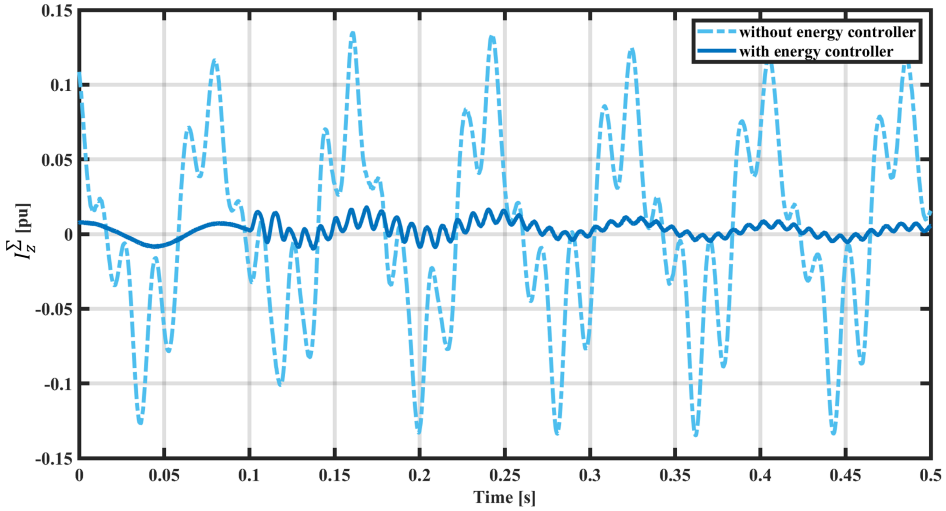

Figure 5.7: 0-component of the circulating current.

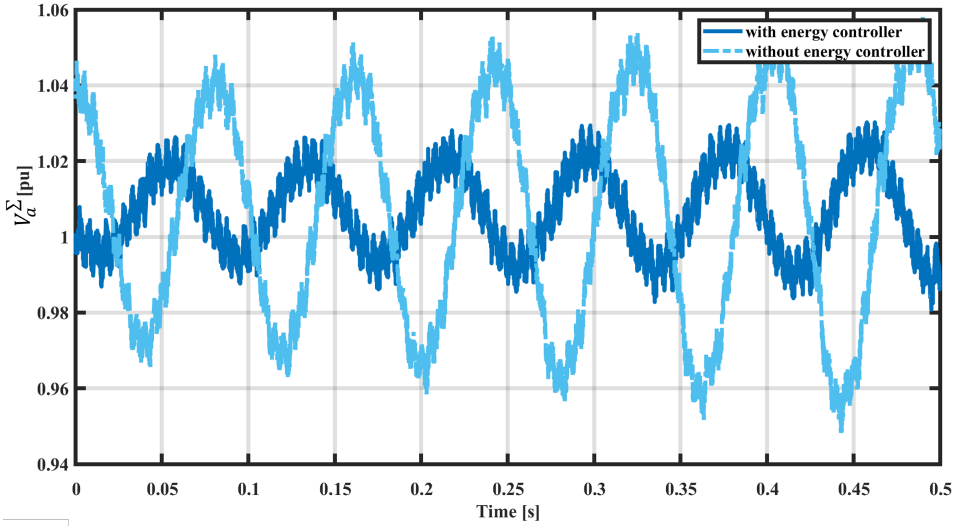

Figure 5.8: single phase SM capacitor voltage.

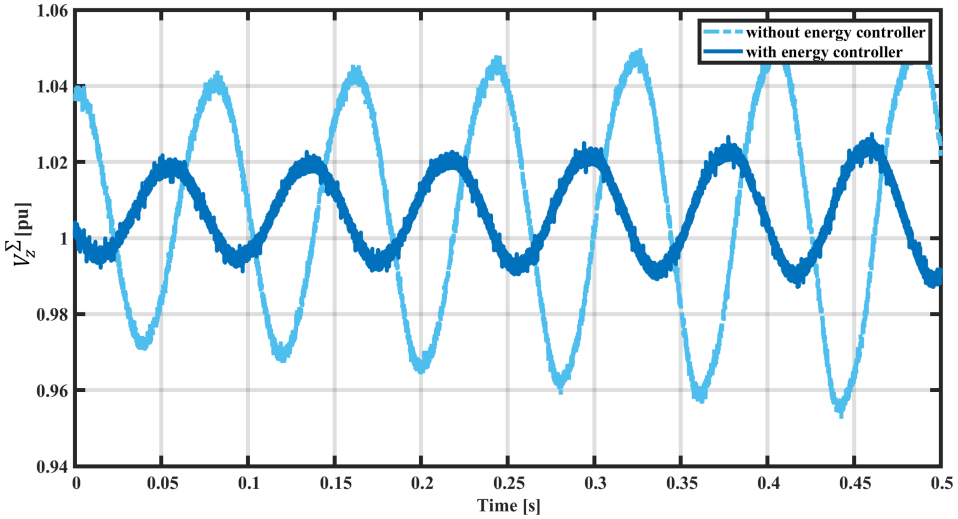

Figure 5.9: 0-component of the SM capacitor voltage.

6
Controllers

The traditional MMC control strategy mainly utilises the PI controller principle. The parameter setting is convoluted, and the control process is complicated. The model predictive control strategy is the optimal control method based on the model in the existing time domain [37]. Conventional controllers are typically analogue hardware, whereas modern industrial applications rely on digital control platforms such as DSP/FPGA for their higher computational power and lower cost over long runs, avoiding ageing and parameter changes. Modern digital controllers offer programming flexibility (software and hardware solutions) compared to analogue controllers, which rely solely on hardware. Digital control is suitable and efficient for meeting grid code regulations and requirements, which cannot be achieved using hardware-only solutions. Model Predictive Control (MPC) has a faster and smoother response than conventional systems, with less control complexity. Traditional control approaches require modelling the physical system and determining its transfer function to design and tune control parameters. In contrast, MPC has a sound theoretical basis and well-understood stability, optimality, and robustness properties. Despite being simple to design and implement, MPC algorithms can control large-scale systems with many control variables and provide a systematic technique for dealing with constraints on inputs and states. The nonlinear behavior of the system can be incorporated into MPC control. MPC offers lower rising time, settling time, and overshoots than PID controllers. Additionally, digital controllers eliminate dangerous oscillations and provide smooth operation during transient periods [26]. Below are some of the Specific advantages MPC has over PI-based controllers making it ideal for real-time testing:

- MPC is a model-based controller design procedure that can easily handle multi-input multi-output processes with large time delays, non-minimum phase processes, and unstable processes.
- It is an easy-to-tune method: in principle, only three parameters must be tuned.
- MPC can handle constraints on the inputs and the outputs of the process due to, e.g., limited capacity of buffers, actuator saturation, output quality specifications, etc., in a systematic way during the design and the implementation of the controller.
- MPC can handle structural changes, such as sensor or actuator failures, and changes in system parameters or system structure, by adapting the model and by using a moving horizon approach, in which the model and the control strategy are regularly updated [11]

6.1. Controllers for the MMC in the network

PI-based and MPC-based controllers are utilised to implement the control strategies discussed in detail in Chapter 4. The control strategy used for the MMCs involves two control loops: the outer loop and the inner loop.
The outer loop sets the control quantities to their reference value. In contrast, the inner loop takes the output from the outer loop to control the dq currents and produce the modulation voltage signals.

6.1.1. Formulation of PI-based controller

Due to its simplicity and effectiveness, PI-based controllers are a widely accepted technique for regulating the performance of MMCs. These controllers are designed to maintain desired setpoints for critical variables like circulating current, AC voltage (V_{ac}), DC voltage (V_{dc}), or Active power(P) or Reactive Power(Q) to ensure stable and accurate operation of the network. The Proportional term of the PI controller provides a control action that is proportional to the error between the desired setpoint and the actual value of the controlled variable. This allows for a suitable response to system changes, which aids

in reducing steady-state errors [31]. Meanwhile, the Integral term helps to account for the accumulated error over time, ensuring that any long-term steady-state errors are corrected by continuously modifying the control action. By integrating the error, the controller can eliminate residual offsets and enhance the system's stability and accuracy. Properly tuning the proportional and integral gains of the controller provides a reliable and robust control mechanism for MMC HVDC networks, enabling precise regulation of variables, effective rejection of disturbances, and improved system performance [75]. The physical definitions that govern the PI-based control loops are,

$$\Delta i_d^{ref} = \frac{1}{V_{DC}} (P^* - P) \tag{6.1}$$

$$\Delta i_d^{ref} = 6C_{arm} \frac{dV_{dc}}{dt} \tag{6.2}$$

$$\Delta i_q^{ref} = \frac{1}{V_{AC}} (Q^* - Q) \tag{6.3}$$

$$\Delta i_q^{ref} = \frac{\Delta V_{AC}}{\omega L_{eq}^{ac}} \tag{6.4}$$

and the PI-based formulations are as follows:

$$i_d^{ref} = \frac{1}{v_{DC}} \left(\frac{k_{i_p}}{s} + k_{pi} \right) (P^* - P) \tag{6.5}$$

$$i_d^{ref} = \left(\frac{k_{i_p}}{s} + k_{pi} \right) \left(V_{DC}^* - V_{DC} \right) \tag{6.6}$$

$$i_q^{ref} = \frac{1}{v_{AC}} \left(\frac{k_{i_q}}{s} + k_{pq} \right) (Q^* - Q) \tag{6.7}$$

$$i_q^{ref} = \left(\frac{k_{i_q}}{s} + k_{pq} \right) \left(V_{AC}^* - V_{AC} \right) \tag{6.8}$$

The inner loops of the converter control strategies have been discussed in detail in the previous chapters (Chapter 4). Therefore, here is a brief recap:

$$\frac{d}{dt} \left(\vec{i}_{dq}^{\Delta} \right) = \frac{\vec{v}_{Mdq}^{\Delta} - \left(\omega L_{eq}^{ac} J_2 + R_{eq}^{ac} I_2 \right) \vec{i}_{dq}^{\Delta} - \vec{v}_{dq}^{G}}{L_{eq}^{ac}} \tag{6.9}$$

and its PI-based formulation is,

$$\vec{v}_{Mdq}^{\Delta} = \left(\frac{k_{i_i}}{s} + k_{pi} \right) \vec{i}_{dq}^{\Delta} + \left(\omega L_{eq}^{ac} J_2 + R_{eq}^{ac} I_2 \right) \vec{i}_{dq}^{\Delta} + \vec{v}_{dq}^{G} \tag{6.10}$$

In all the above equations, $\frac{k_i}{s}$ is the integral component of the PI controller, and the k_p is the proportional component.

6.1.2. Formulation of MPC

Classical control methods are simple to implement in digital controllers, but their dynamic response is constrained by various factors such as the gains of the PI-regulator, current controller bandwidth, converter switching frequency, and the type of PWM scheme used. As an alternative, the predictive control approach, also known as model predictive control, is gaining popularity and widely used to control power converters[58, 15, 50].In model predictive control (MPC), a plant model is utilized to forecast the control inputs. This model acts as a mathematical replica, where the model outputs are used as inputs for the plant, and the plant outputs are then fed back as inputs to the model. In the context of MMC, MPC is implemented for the inner loop, one of the two cascaded controllers, to regulate the MMC's currents.

In MPC, we consider the system's future evolution over a given prediction period $[k+1, k+N_p]$, which

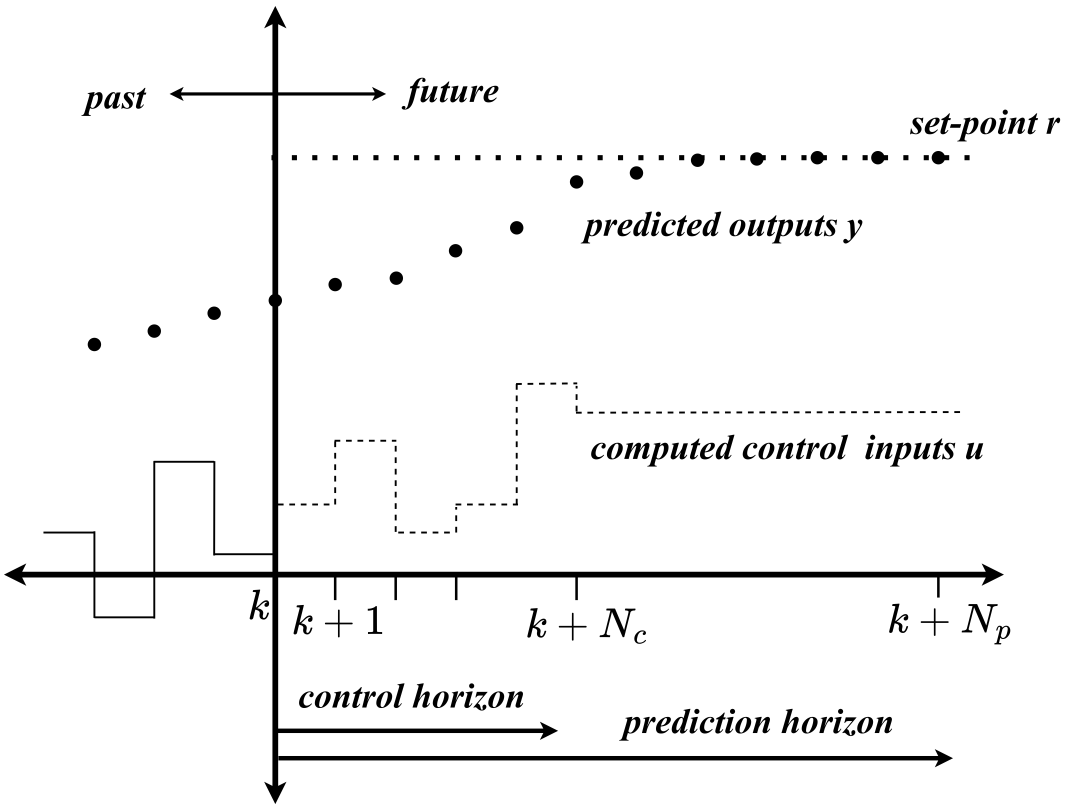

Figure 6.1: Model Predictive Control (MPC) scheme

is characterised by the prediction horizon N_p, and N_c is the control horizon, where k is the current sample step (Fig. 6.1). For the plant model (Eq. (6.11)), we can make an estimate $\tilde{Y}(k)$ of the output at sample step k based on the states $\vec{x}(k)$ at step k and the future input sequence $\vec{u}(k), \vec{u}(k+1), ..., \vec{u}(k+i-1)$ [11].

Model predictive control (MPC) algorithms are used on digital control platforms like DSP, FPGA, and computers with real-time interface cards. These platforms are designed to handle sample-based continuous-time systems, also known as discrete-time systems. Hence, to use MPC on MMC, the continuous-time model equation(Eq. (6.9)) must be transformed into a discrete-time state-space model model[15](Eq.(6.11), shows the discrete state-space equations).

$$\begin{aligned} \vec{x}(k+1) &= A\vec{x}(k) + B\vec{u}(k) \\ \vec{y}(k) &= C\vec{x}(k) + D\vec{u}(k) \end{aligned} \tag{6.11}$$

In this case, the D matrix of Eq.(6.11) is 0 since there is no feed-forward loop.The $\vec{x}(k)$ (state space variables) and $\vec{u}(k)$(input variables), Eq. (6.12); A, B and C matrices are given in Eq. (6.13),

$$\vec{x}(k) = \begin{bmatrix} \vec{i}_d^{\Delta} \\ \vec{i}_q^{\Delta} \\ \vec{i}_{dB}^{\Delta} \\ \vec{i}_{qB}^{\Delta} \end{bmatrix} \text{ and } \vec{u}(k) = \begin{bmatrix} \vec{v}_{Md}^{\Delta} - \vec{v}_d^{G} \\ \vec{v}_{Mq}^{\Delta} - \vec{v}_q^{G} \\ \vec{v}_{MdB}^{\Delta} - \vec{v}_{dB}^{G} \\ \vec{v}_{MqB}^{\Delta} - \vec{v}_{qB}^{G} \end{bmatrix} \tag{6.12}$$

where the subscript B in Eq. (6.12) stands for the negative or lower MMC in the bipolar configuration.

$$A = \begin{bmatrix} -\frac{R_{eq}^{ac}}{L_{eq}^{ac}} & -\omega & 0 & 0 \\ \omega & -\frac{R_{eq}^{ac}}{L_{eq}^{ac}} & 0 & 0 \\ 0 & 0 & -\frac{R_{eq}^{ac}}{L_{eq}^{ac}} & -\omega \\ 0 & 0 & \omega & -\frac{R_{eq}^{ac}}{L_{eq}^{ac}} \end{bmatrix}, B = \begin{bmatrix} \frac{1}{L_{eq}^{ac}} & 0 & 0 & 0 \\ 0 & \frac{1}{L_{eq}^{ac}} & 0 & 0 \\ 0 & 0 & \frac{1}{L_{eq}^{ac}} & 0 \\ 0 & 0 & 0 & \frac{1}{L_{eq}^{ac}} \end{bmatrix}, \text{and } C = A. \tag{6.13}$$

The MMC's AC side and DC side equations are discretized using the zero-order hold discretization method and augmented in the rate-based state space equations [66] using the solutions of the differential equations. Upon discretization of said differential equations, the system is defined with difference equations,

$$\begin{bmatrix} \Delta\vec{x}(k+1) \\ \vec{y}(k+1) \end{bmatrix} = \overbrace{\begin{bmatrix} F(T_s) & o^T \\ H(T_s)F(T_s) & 1 \end{bmatrix}}^{A_d} \overbrace{\begin{bmatrix} \Delta\vec{x}(k) \\ \vec{y}(k) \end{bmatrix}}^{\vec{x_m}(k)} + \overbrace{\begin{bmatrix} G(T_s) \\ H(T_s)G(T_s) \end{bmatrix}}^{B_d} \Delta\vec{u}(k) \tag{6.14}$$

$$\vec{y}_m(k) = \overbrace{\begin{bmatrix} 0 & I \end{bmatrix}}^{C_d} \vec{x}_m(k), \tag{6.15}$$

where $H(T_s)$ is an identity matrix, whereas $F(T_s) = e^{AT_s}$ and $G(Ts) = A^{-1}\left(e^{AT_s} - I\right)B$. $_s$ is the sampling time. Furthermore, the augmented state is defined as $\Delta\overrightarrow{x}(k) = \overrightarrow{x}(k) - \overrightarrow{x}(k-1)$, where $\overrightarrow{x}(k)$ indicates the system state vector at k^th instant and $\overrightarrow{x}(k-1)$ indicates vector of past states. Similarly, the augmented input is defined as $\Delta\overrightarrow{u}(k) = \overrightarrow{u}(k) - \overrightarrow{u}(k-1)$, where $\overrightarrow{u}(k)$ represent the system inputs at k^{th} instant and $\overrightarrow{x}(k-1)$ indicates the past inputs.

$$\overrightarrow{x_m}(k+1) = A\overrightarrow{x_m}(k) + B\Delta\vec{u}(k), \tag{6.16}$$

With A and B as state space matrix coefficients and $\overrightarrow{x_m}(k)$ are the state variables, and the $\Delta\vec{u}(k)$ are the inputs for the k^{th} instance.

Cost function for MPC

The cost function consists of multiple control objectives optimized for weighting factors to reach the desired system behavior. The resulting switching state is then applied to the converter[46, 86].The value of $\Delta\vec{u}(k)$ is calculated by minimizing the objective (cost) function, subjected to equality and inequality constraints. The cost function is formulated with LQR as a base.

$$\min J = \sum_{i=1}^{N_p} \overrightarrow{x_m}(k+i \mid k)^T Q \overrightarrow{x_m}(k+i \mid k) + \Delta\vec{u}(k)^T R \Delta\vec{u}(k), \tag{6.17}$$

where,

$$\overrightarrow{x_m}(k+i \mid k) = \overrightarrow{y_m^*}(k) - \overrightarrow{y_m}(k \mid k)$$

Here, $Q \succeq 0$ and $R \succ 0$ are weighting matrices, and N_p is the prediction horizon. For the state variables $\overrightarrow{x_m}(k)$, $\overrightarrow{y_m^*}(k)$ is a reference signal ($\overrightarrow{r}(k)$ in Fig. 6.1) and $\overrightarrow{y_m}(k)$ is the output variable of the plant.

$$V(\vec{x_m}(k), k) = \sum_{i=1}^{N_p} \vec{x_m}(k+i \mid k)^T Q \vec{x_m}(k+i \mid k) + \sum_{i=1}^{N_p-1} \Delta\vec{u}(k+i)^T R \Delta\vec{u}(k+i). \tag{6.18}$$

Constraints for MPC
The MPC block created with the cost function takes into account the following control input constraints:

$$\begin{aligned} -1.1 \text{ p.u.} &< I_d < 1.1 \text{ p.u.} \\ -1.1 \text{ p.u.} &< I_q < 1.1 \text{ p.u.} \end{aligned} \tag{6.19}$$

These constraints are the ones used in the Pi-based controller to limit the i_{dq} currents based on the IGBT current limits in the submodules of the MMCs. With the cost function and the constraints above, a new equality function is realised called the Multi-predictive equation.

$$\tilde{Y}(k) = F\vec{x_m}(k) + \phi\Delta\vec{u}(k) \tag{6.20}$$

$$F = \begin{bmatrix} C \\ CA^2 \\ \vdots \\ CA^{N_p} \end{bmatrix} \tag{6.21}$$

$$\phi = \begin{bmatrix} CB & 0 & . & . & . & . \\ CAB & CB & 0 & . & . & . \\ CA^2B & CAB & CB & 0 & . & . \\ . & . & . & . & . & . \\ . & . & . & . & . & . \\ CA^{N_p-1}B & CA^{N_p-2} & . & . & . & CA^{N_p-N_c}B \end{bmatrix} \tag{6.22}$$

An MPC block for the inner control loop can be created with the multi-prediction equation, the cost function, and the constraints provided.

6.2. Validation of MPC

In this chapter section, the controllers are compared for the same scenarios, and the results are presented as follows. The scenarios are:

- three phase ac fault on the PCC between the ac grid and the converter station (AC fault)
- positive pole to ground fault on cable H2 (cable connecting the DC Hub to MMC2)(DC fault)
- phase jump of 20° in the AC voltage to exhibit the anomalous behavior of the AC voltage. (phase jump)

6.2.1. Three-Phase AC fault

Table 6.1: Controller performance for three-phase AC fault, based on the ac grid voltage waveforms of MMC4, with GFL control strategy

SCR	Sag (pu)		settling time(s)		settled value (pu)	
	MPC	PI	MPC	PI	MPC	PI
45	-0.85212	-0.8523	0.3736	0.3768	1.00124	1.00134
35	-0.8809	-0.882	0.3752	0.39	1.00161	1.00148
20	-0.92678	-0.927	0.378	0.3914	1.0024	1.0026
10	-0.9591	-0.959	0.38411	0.4184	1.005	1.01509
9	-0.96211	-0.9626	0.387891	0.4271	1.006	1.01552
8	-0.9644	-0.9645	0.391419	0.4322	1.00741	1.01669
7	-0.9676	-0.968	0.39877	0.4373	1.00775	1.01885
6	-0.97104	-0.975	0.402	0.4453	1.00978	1.02239
5	-0.9743	-0.9765	0.411	0.4471	1.011	1.025
4	-0.9774	-0.979	0.419	0.4512	1.012	1.032

Fig. 6.2, illustrates the ac voltage behavior for the converter in the grid following control strategy with a PI-based and MPC-based controller.No significant difference is noticeable in Fig. 6.2a and Fig. 6.2b. The difference is only noticeable when the SCR is reduced to values below 10. When the loss

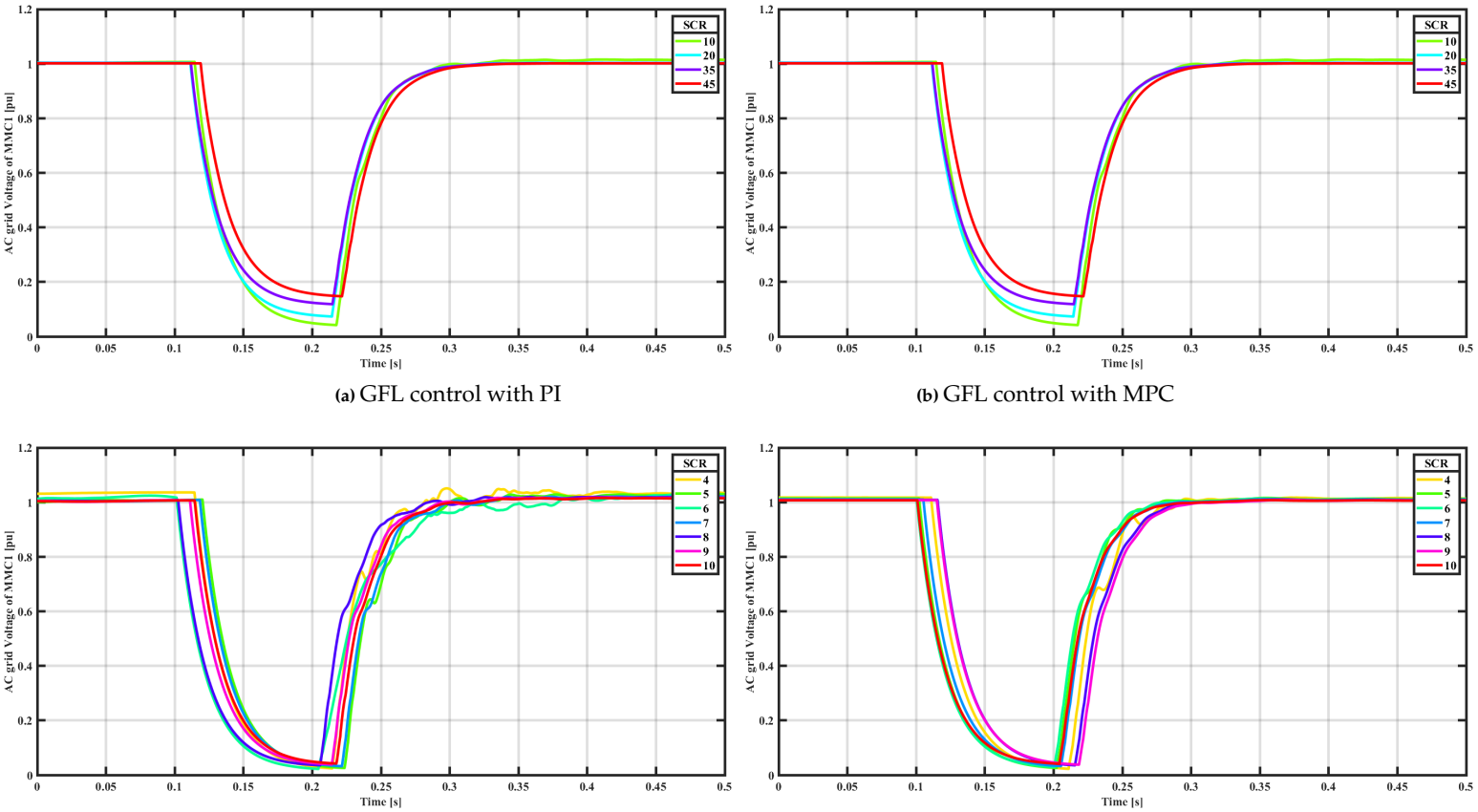

(a) GFL control with PI

(b) GFL control with MPC

(c) GFL control with PI, for low SCRs

(d) GFL control with MPC, for low SCRs

Figure 6.2: AC voltage behavior during a three-phase AC fault. (a) GFL with PI for average SCRs, (b) GFL with MPC for average SCRs, (c) GFL with PI for low SCRs, (d) GFL with MPC for low SCRs.

of synchronicity becomes more noticeable, the grid following converter with the PI-based controller performs poorly, Fig.6.2c. Whereas in Fig. 6.2, it is seen that even for low SCRs, the control performs almost as expected due to a faster response time of the MPC. Due to the MPC, the grid following control strategy is able to perform according to expectation until and including SCR 4. Table 6.1 corroborates the information discussed, providing a visual representation that reinforces the previously mentioned points.

Fig. 6.3 and Table 6.2 illustrate the ac voltage behavior for the converter in the grid forming control strategy with a PI-based and MPC-based controller.No significant difference is observed for SCRs higher than 10 in Fig. 6.3a and Fig. 6.3b. For SCRs below 10, the AC voltage becomes unpredictable due to the loss of synchronicity and the increase in grid impedance, but there is not much observed as the grid-forming converter forms its own Voltage and frequency for the converter. The only drawback is the minor oscillations in Fig. 6.3d for SCR, 2. In almost all the cases in this transient scenario, the MPC reacts faster and is able to have a faster response time, except for the case of SCR, 2, where the controller tends to be $0.03s$ slower than PI due to the oscillations. Table 6.2 corroborates the information discussed, providing a visual representation that reinforces the previously mentioned points; the settling times (s) for the MPC are indicated in green, which show that the MPC reacts faster than the Pi-based controller.

6.2.2. Positive pole-to-ground, DC fault

Fig. 6.4, illustrates the ac voltage behavior for the converter in the grid following control strategy with a PI-based and MPC-based controller. No significant difference is noticeable in Fig. 6.2a and Fig. 6.2b for SCRs higher than 10. The difference is only noticeable when the SCR is reduced to values 10 and lower. When the loss of synchronicity becomes more noticeable, the grid following converter with the PI-based controller performs poorly, Fig. 6.4c. Whereas in Fig. 6.4d it is seen that even for low SCRs, the control performs almost as expected due to a faster response time of the MPC. It can also be observed that

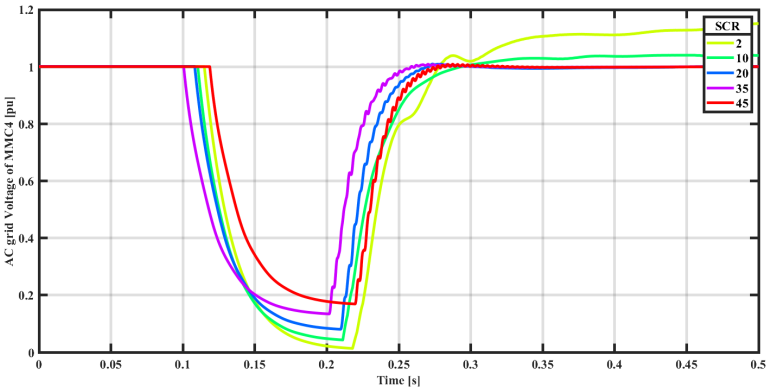

(a) GFM control with PI

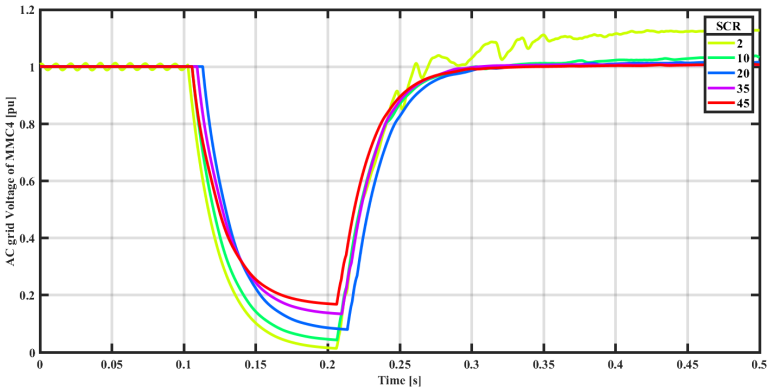

(b) GFM control with MPC

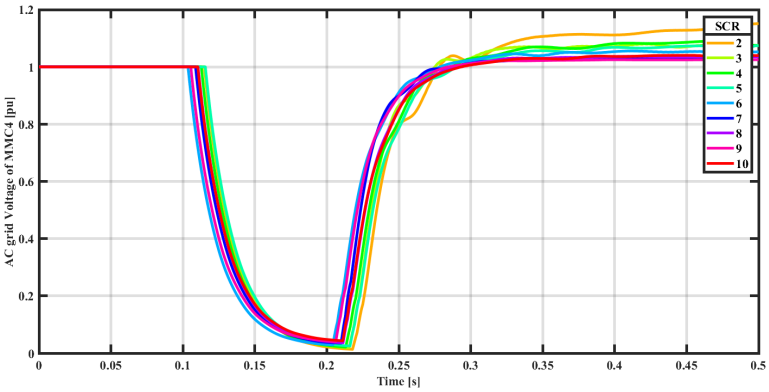

(c) GFM control with PI, for low SCRs

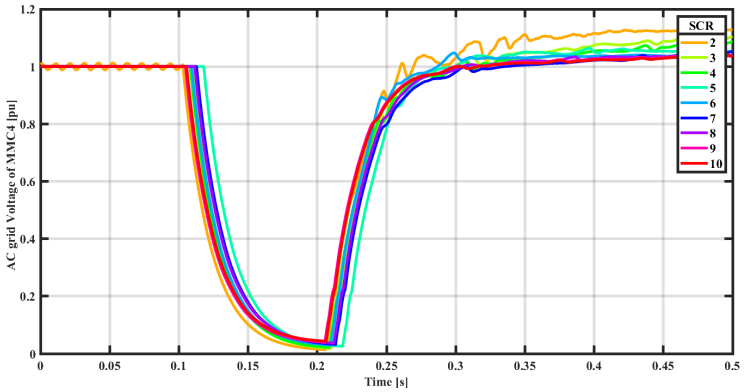

(d) GFM control with MPC, for low SCRs

Figure 6.3: AC voltage behavior during a three-phase AC fault. (a) GFM with PI for average SCRs, (b) GFM with MPC for average SCRs, (c) GFM with PI for low SCRs, (d) GFM with MPC for low SCRs.

Table 6.2: Controller performance for three-phase AC fault, based on the ac grid voltage waveforms of MMC4, with GFM control strategy

SCR	Sag (pu)		settling time(s)		settled value (pu)	
	MPC	PI	MPC	PI	MPC	PI
45	-0.8006	-0.81	0.3227	0.339	0.9999	0.99
35	-0.842	-0.85	0.3309	0.34	1.0004	0.994
20	-0.913	-0.915	0.3337	0.35	1.001	0.99
10	-0.947	-0.948	0.359	0.38	1.01	1.03
9	-0.951	-0.953	0.3679	0.384	1.017	1.023
8	-0.9542	-0.958	0.3684	0.384	1.0179	1.029
7	-0.9621	-0.963	0.3797	0.385	1.0125	1.033
6	-0.961	-0.965	0.3878	0.387	1.0355	1.05
5	-0.975	-0.9721	0.3897	0.387	1.053	1.056
4	-0.976	-0.973	0.3948	0.39	1.049	1.064
3	-0.979	-0.977	0.3979	0.39	1.07	1.067
2	-0.981	-0.98	0.42	0.39	1.127	1.11

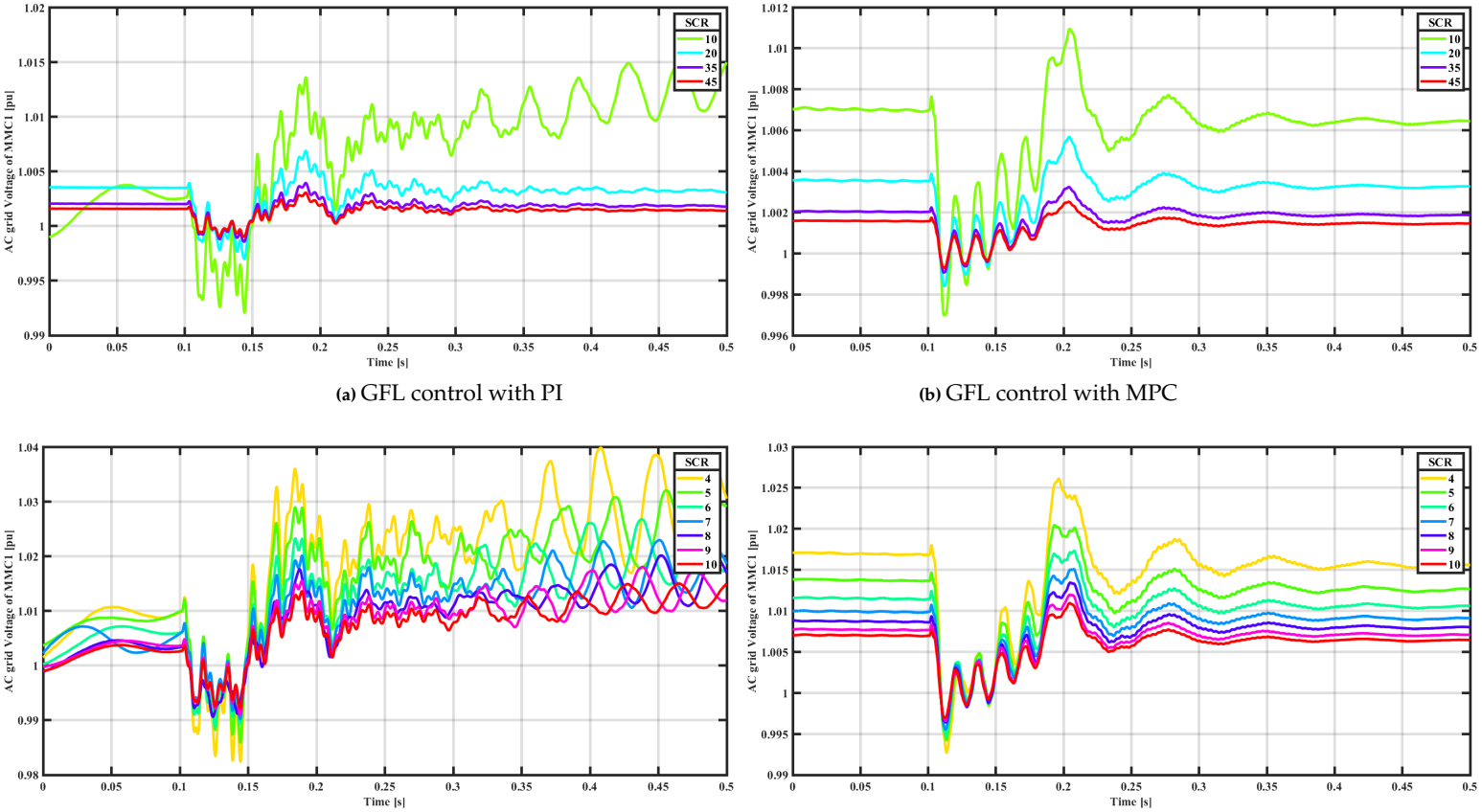

(a) GFL control with PI

(b) GFL control with MPC

(c) GFL control with PI, for low SCRs

(d) GFL control with MPC, for low SCRs

Figure 6.4: AC voltage behavior during a pole-to-ground DC fault. (a) GFL with PI for average SCRs, (b) GFL with MPC for average SCRs, (c) GFL with PI for low SCRs, (d) GFL with MPC for low SCRs.

post clearance of the fault, the PI-based controller suffers some oscillations, whereas the MPC-based controller is able to reach a steady state value faster than the PI-based controller. Due to the MPC, the grid following control strategy is able to perform according to expectation until and including SCR 4. Table 6.3 corroborates the information discussed, providing a visual representation that reinforces the previously mentioned points. Furthermore, the inconsistencies in the table for the PI-based controller for SCRs below 10 (indicated in red and orange) are due to the higher grid impedance and the unstable PLL synchronicity.

Fig. 6.4 and Table 6.4 illustrate the ac voltage behavior for the converter in the grid forming control strategy with a PI-based and MPC-based controller.No significant difference is observed for SCRs higher than 10 in Fig. 6.5a and Fig. 6.5b. For SCRs below 10, the AC voltage becomes unpredictable due to the loss of synchronicity and increased grid impedance. Still, not much is observed as the grid-forming converter forms its Voltage and frequency for the converter. The only drawback is the minor oscillations in Fig. 6.5d for SCR, 2, which can be attributed to the fact that a filter was introduced and hence caused this strange behavior. In almost all the cases in this transient scenario, the MPC reacts faster and can have a faster response time; it is also important to note that though the introduction of the filter caused some abnormal behavior leading to a delayed second peak, MPC based controller was still faster than the than PI in returning to its set points. Table 6.4 corroborates the information discussed, providing a visual representation that reinforces the previously mentioned points; the settling times (s) for the MPC are indicated in green, which shows that the MPC reacts faster than the Pi-based controller.

6.2.3. Phase jump in AC voltage angle

Fig. 6.6, illustrates the ac voltage behavior for the converter in the grid following control strategy with a PI-based and MPC-based controller. No significant difference is noticeable in Fig. 6.6a and Fig. 6.6b for SCRs higher than 10. The difference is only noticeable when the SCR is reduced to values 10 and

Table 6.3: Controller performance for a pole-to-ground DC fault, based on the ac grid voltage waveforms of MMC4, with GFL control strategy

SCR	peak Over/under shoot (pu)		settling time(s)		settled value (pu)	
	MPC	PI	MPC	PI	MPC	PI
45	0.00168	0.00175	0.303345	0.3157	1.00139	1.00162
35	0.00219	0.00225	0.328167	0.332	1.00187	1.00178
20	0.00376	0.00376	0.340893	0.3579	1.0034	1.00336
10	0.00756	0.00552	0.350154	0.3699	1.00684	1.01109
9	0.00835	0.003	0.358596	0.3894	1.00736	1.01475
8	0.00932	0.00405	0.367479	0.39068	1.00815	1.01521
7	0.01032	0.00753	0.373401	0.4048	1.00908	1.02148
6	0.01229	0.00931	0.380583	0.4086	1.01035	1.02596
5	0.01453	0.01179	0.394065	0.4106	1.01241	1.03265
4	0.01797	0.01249	0.398223	0.4243	1.0153	1.03445

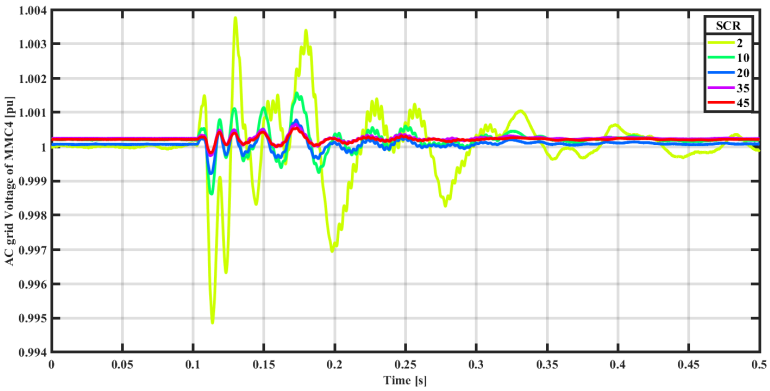

(a) GFM control with PI

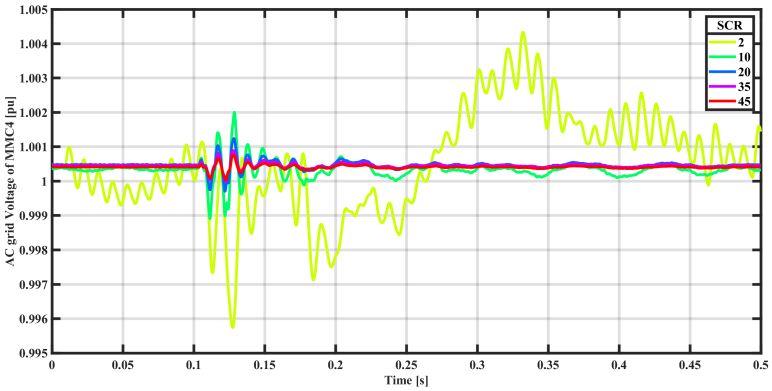

(b) GFM control with MPC

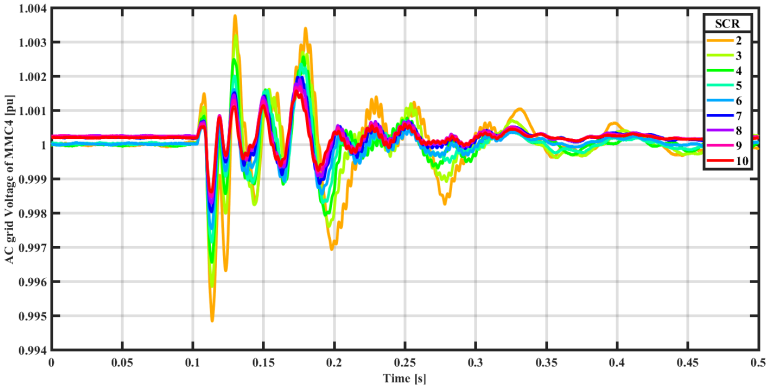

(c) GFM control with PI, for low SCRs

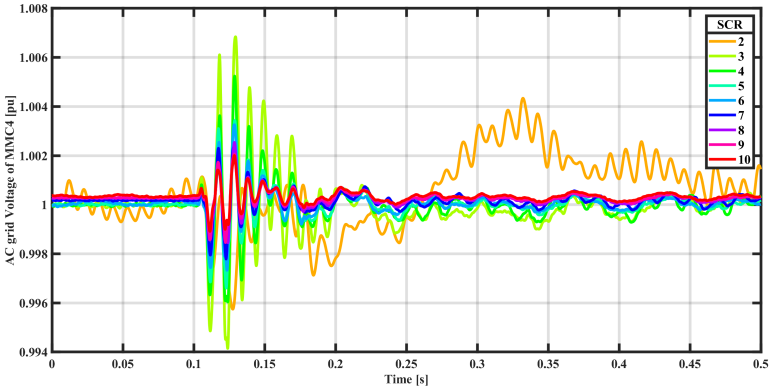

(d) GFM control with MPC, for low SCRs

Figure 6.5: AC voltage behavior during a pole-to-ground DC fault. (a) GFM with PI for average SCRs, (b) GFM with MPC for average SCRs, (c) GFM with PI for low SCRs, (d) GFM with MPC for low SCRs.

Table 6.4: Controller performance for a pole-to-ground DC fault, based on the ac grid voltage waveforms of MMC4, with GFM control strategy

SCR	peak Over/under shoot (pu)		settling time(s)		settled value (pu)	
	MPC	PI	MPC	PI	MPC	PI
45	0.00048	0.00012	0.1495	0.245	1.00052	1.00026
35	0.00055	0.0002	0.1599	0.25	1.00052	1.00072
20	0.00062	0.0003	0.1681	0.253	1.00052	1.0002
10	0.00067	0.00039	0.2053	0.26	1.0006	1.0001
9	0.00067	0.00056	0.2199	0.2706	1.00058	1.0006
8	0.0007	0.0006	0.222	0.2777	1.00057	1.0004
7	0.00075	0.00066	0.2226	0.284	1.00061	1.0008
6	0.00078	0.00068	0.2566	0.296	1.00017	0.999
5	0.00079	0.00072	0.2848	0.303	1.00022	0.9999
4	0.00081	0.00082	0.3061	0.31	1.000616	1.00019
3	0.00607	0.001	0.3969	0.431	0.999	0.999
2	0.00617	0.0012	0.442	0.482	1.003	1

Table 6.5: Controller performance for phase jump in AC grid voltage, based on the ac grid voltage waveforms of MMC4, with GFL control strategy

SCR	peak Over/under shoot (pu)		settling time(s)		settled value (pu)	
	MPC	PI	MPC	PI	MPC	PI
45	0.00201	0.0031	0.2174	0.2235	1.00156	1.0053
35	0.0026	0.00387	0.2343	0.2401	1.00195	1.0021
20	0.00457	0.00646	0.2379	0.2476	1.00336	1.00385
10	0.01236	0.01249	0.2404	0.25012	1.006	1.0071
9	0.013	0.009	0.2584	0.4284	1.00764	1.0167
8	0.015	0.00548	0.2697	0.439	1.00833	1.01744
7	0.01715	0.013	0.2859	0.4471	1.00946	1.02117
6	0.01962	0.0148	0.3016	0.4458	1.01109	1.02426
5	0.02328	0.017	0.3117	0.4528	1.01335	1.02858
4	0.02796	0.02149	0.3211	0.4914	1.01628	1.02858

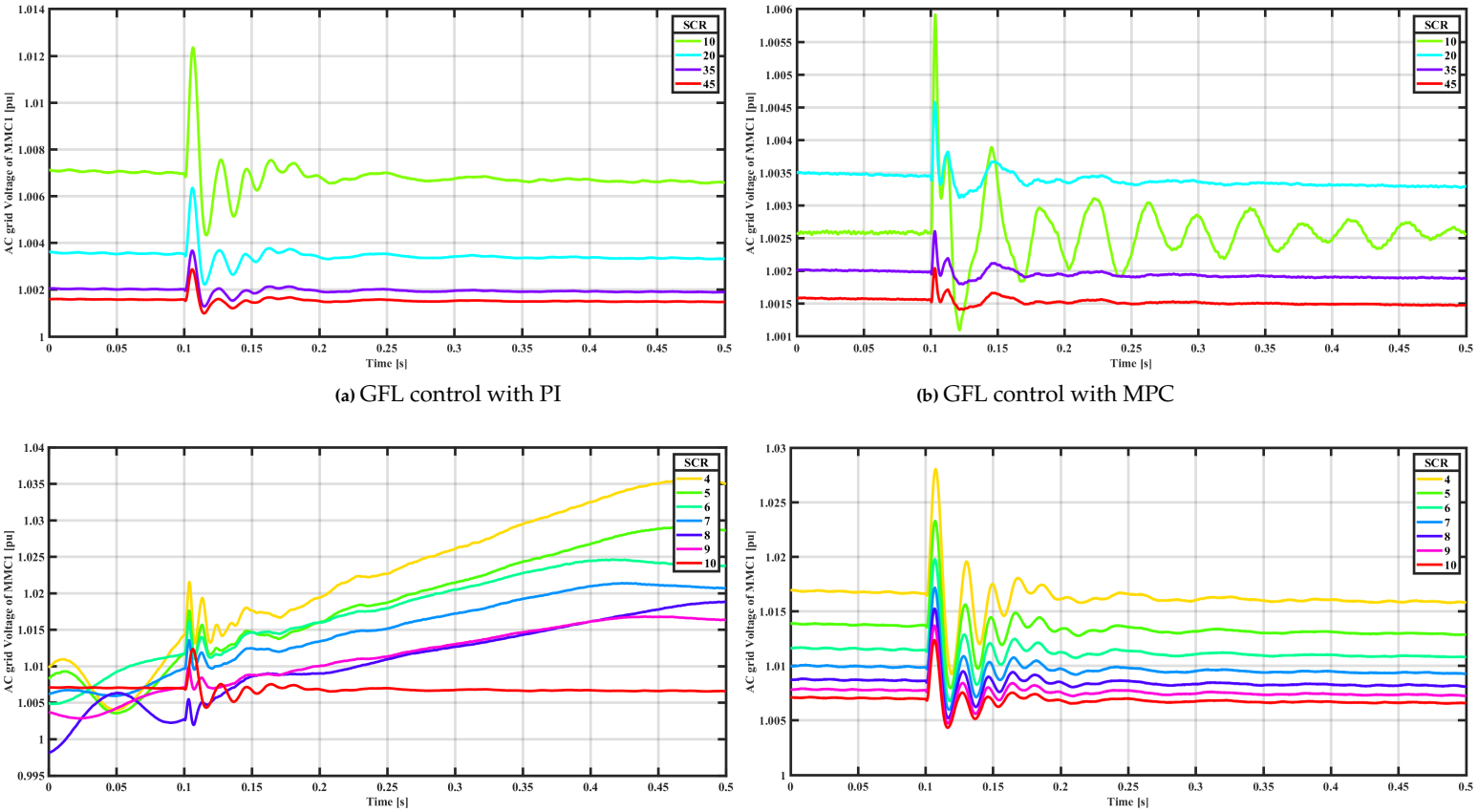

(a) GFL control with PI

(b) GFL control with MPC

(c) GFL control with PI, for low SCRs

(d) GFL control with MPC, for low SCRs

Figure 6.6: AC voltage behavior during a phase jump in the AC grid Voltage. (a) GFL with PI for average SCRs, (b) GFL with MPC for average SCRs, (c) GFL with PI for low SCRs, (d) GFL with MPC for low SCRs.

lower. When the loss of synchronicity becomes more noticeable, the grid following converter with the PI-based controller performs poorly, Fig. 6.6c. Whereas in Fig. 6.6d, it is seen that even for low SCRs, the control performs almost as expected due to a faster response time of the MPC. It can also be observed that post clearance of the fault, the PI-based controller suffers from a ramp increase in its steady state set points, whereas the MPC-based controller is able to reach steady state value faster than the PI-based controller. Due to the MPC, the grid following control strategy is able to perform according to expectation until and including SCR 4. Table 6.5 corroborates the information discussed, providing a visual representation that reinforces the previously mentioned points. Furthermore, the inconsistencies in the table for the PI-based controller for SCRs below 10 (indicated in red and orange) are due to the higher grid impedance and the unstable PLL synchronicity.

Fig. 6.7 and Table 6.6illustrate the ac voltage behavior for the converter in the grid forming control strategy with a PI-based and MPC-based controller. No significant difference is observed for SCRs higher than 10 in Fig. 6.7a and Fig. 6.7b. For SCRs below 10, the AC voltage becomes unpredictable due to the loss of synchronicity and increased grid impedance. Still, not much is observed as the grid-forming converter forms its Voltage and frequency for the converter. The only drawback is the minor oscillations in Fig. 6.7d for SCR, 2, which can be attributed to the fact that a filter was introduced and hence caused this anomalous behavior. In all the cases in this transient scenario, the MPC reacts faster and can have a faster response time; it is also important to note that even with a higher transient peak for SCR 2, MPC based controller was still quicker than the PI in returning to its set points. Table 6.6 corroborates the information discussed, providing a visual representation that reinforces the previously mentioned points; the settling times (s) for the MPC are indicated in green, which shows that the MPC reacts faster than the PI-based controller.

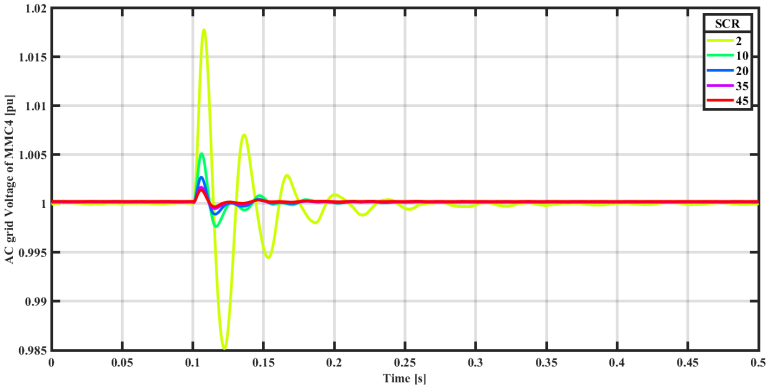

(a) GFM control with PI

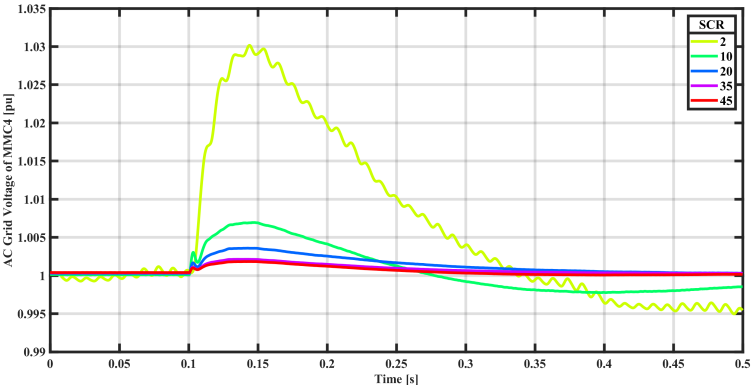

(b) GFM control with MPC

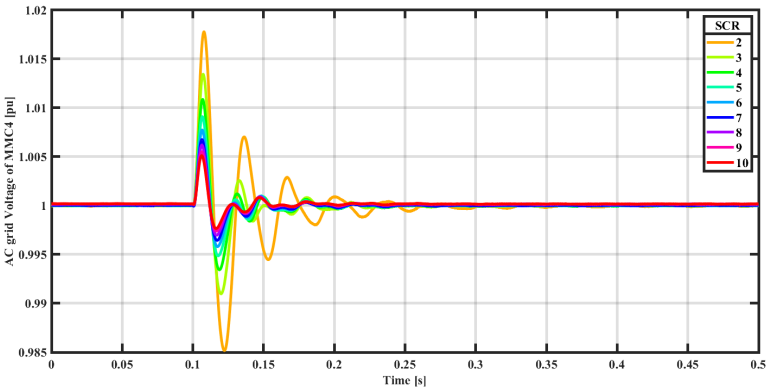

(c) GFM control with PI, for low SCRs

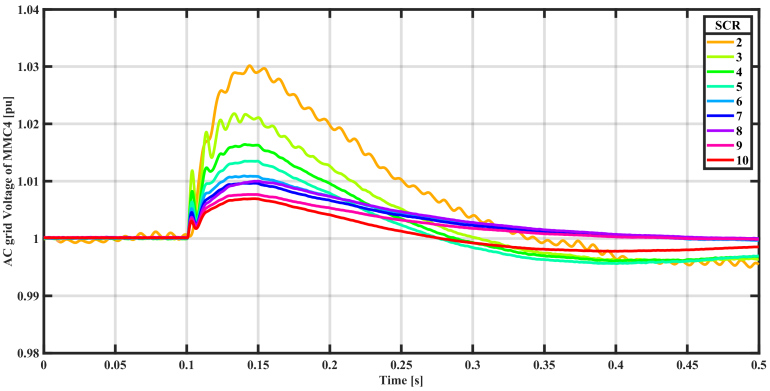

(d) GFM control with MPC, for low SCRs

Figure 6.7: AC voltage behavior during a phase jump in the AC grid Voltage. (a) GFM with PI for average SCRs, (b) GFM with MPC for average SCRs, (c) GFM with PI for low SCRs, (d) GFM with MPC for low SCRs.

Table 6.6: Controller performance for phase jump in AC grid voltage, based on the ac grid voltage waveforms of MMC4, with GFM control strategy.

SCR	peak Over/under shoot		settling time(s)		settled value (pu)	
	MPC	PI	MPC	PI	MPC	PI
45	0.00098	0.00137	0.1706	0.212	1.00182	1.00022
35	0.00108	0.00165	0.183	0.2158	1.00166	1.00021
20	0.00167	0.00263	0.2342	0.243	1.00192	1.0012
10	0.00303	0.005	0.24	0.2457	1.00182	1.00017
9	0.00334	0.00549	0.241	0.2509	1.00262	1.0016
8	0.00357	0.0061	0.2477	0.2568	1.00475	1.0006
7	0.00451	0.00672	0.2526	0.279	1.00393	1.00002
6	0.00517	0.0077	0.284	0.292	1.003	1.0002
5	0.00634	0.009	0.289	0.2949	0.999	0.9999
4	0.00822	0.0108	0.2962	0.3069	0.998	0.9999
3	0.01175	0.01339	0.3112	0.323	0.998	0.9999
2	0.02947	0.0177	0.335	0.415	1.006	0.9999

6.2.4. Harmonic analysis for low SCRs (1 and 2)

In this section, FFT(Fast Fourier Transform) is performed to extract the frequencies of the harmonics present at SCRs of 2 and 1. Wherever feasible, a filter was introduced to remove or minimize the oscillations. This addition of filters was examined for the impact on the behavior and speed of the MPC.

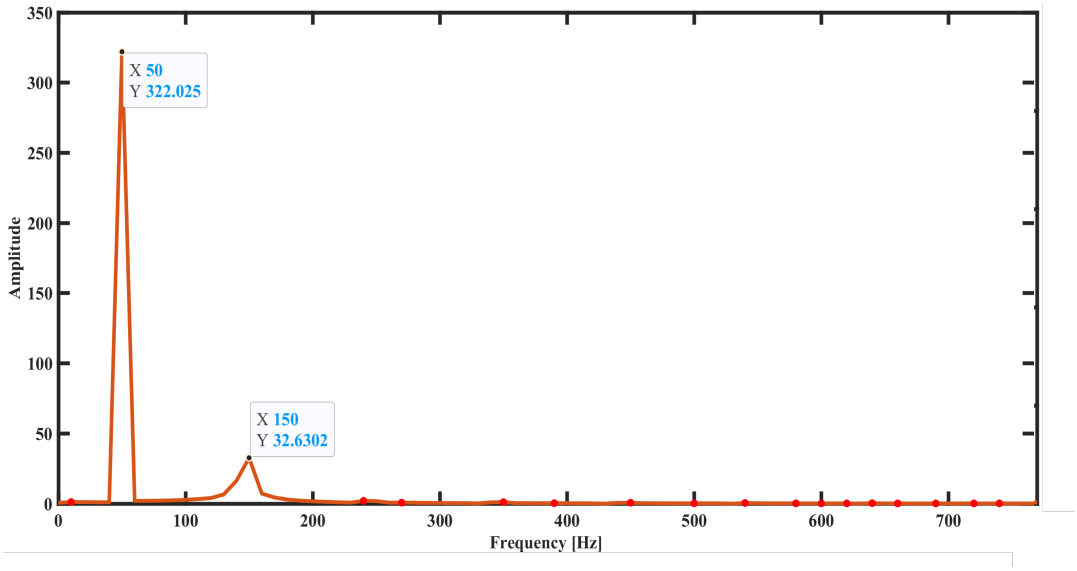

Figure 6.8: FFT analysis for SCR 2.

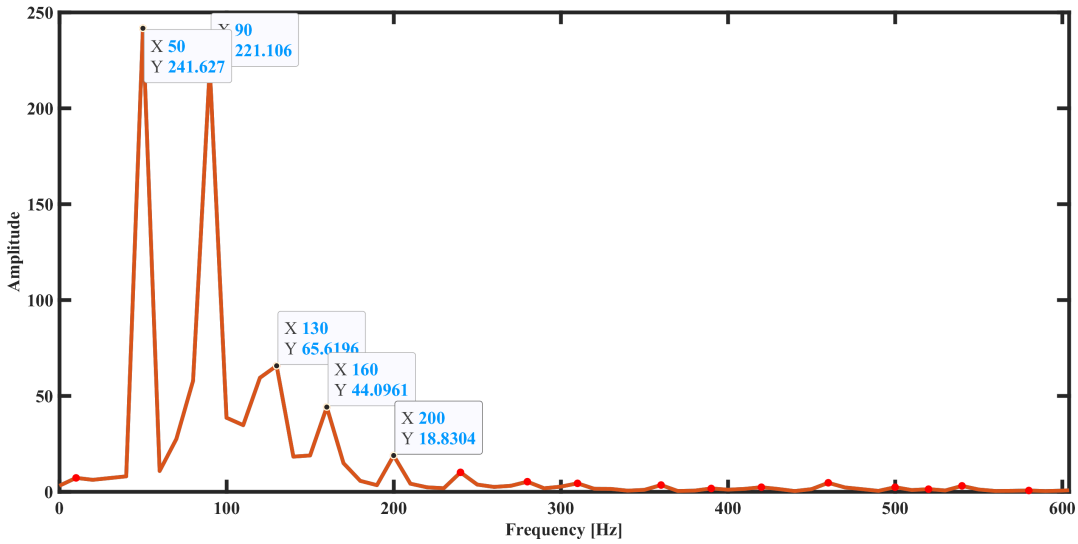

Figure 6.9: FFT analysis for SCR 1.

Adding a filter for SCR 1 was impossible, as the harmonics comprise many frequencies of varying amplitudes, Fig 6.9. But since for SCR 2, Fig 6.8, only one harmonic frequency was present in the FFT analysis apart from the Fundamental frequency ($50Hz$), the realization of the filter was feasible.

7
Large Signal Stability Analysis

Stability analysis of power system networks is critical to ensure their reliability. Stability analysis can be categorised into various types depending on the scenarios tested and the duration of the studies. Steady-state and small-signal studies are crucial when integrating a high penetration of power electronics into a power system. However, the proliferation of sizeable converter-based generation has made large-signal analysis the most limiting aspect [9]. Transient analysis is a type of large-signal analysis used when the event's duration is brief, typically in microseconds. The Direct Lyapunov function is the most commonly used metric to analyse transient stability, and it can be further enhanced using the concept of the Region of Attraction. The Direct Lyapunov function analysis with the Region of Attraction provides valuable insights into the network's behavior during large signal disturbances, making it an essential tool for power system stability analysis.

In power systems, rotor angle stability is a crucial aspect that ensures synchronicity with the rest of the grid in the event of a disturbance [76]. However, this stability analysis is mainly used for networks with generators. In the case of the network discussed in this paper, which involves Voltage Source Converters (VSCs), rotor angle stability analysis is not applicable due to the absence of conventional generators [7]. Moreover, the network implements a grid-forming control strategy for three out of four converters, each with its own angle. Therefore, maintaining synchronicity with the grid is not necessary. Instead, voltage stability is a more relevant stability analysis for this network, as it deals with maintaining a steady and acceptable voltage during a disturbance [30].

The existing literature on power system stability analysis has primarily focused on single Voltage Source Converter (VSC) stations connected to an infinite bus, where the power injected into the VSC station is ideal with no harmonics [82]. However, this paper proposes a network that injects power from an aggregated model of an offshore wind farm, which contains harmonics and realistically represents the power injected into an HVDC transmission network. The aggregated model amplifies the injected harmonics, making it the worst-case scenario to test and analyse. Additionally, while the literature models are point-to-point with a maximum of two VSC stations connected to an infinite bus, the model discussed in this paper is a $\pm 525kV$ four-terminal network with a DC Hub, a modified version of the point-to-point model. According to existing literature, a comparison between grid-following control strategies and grid-forming strategies in the form of the direct Lyapunov stability method has yet to be conducted. Moreover, there needs to be more research on comparing different controllers, such as PI-based and MPC-based, in terms of large signal stability for transient events using the Direct Lyapunov method. The stability analysis of VSC stations connected to AC grids with varying Short Circuit Ratios (SCR) is typically performed using small signal stability analysis in the form of eigenvalue analysis [10, 21, 53]. However, this analysis is only valid around the stable operating point and is inaccurate under large disturbances [33]. Therefore, a time-dependent analysis like transient large signal stability is required when dealing with transient events such as faults and other fast-acting phenomena [69]. This paper discusses the behavior of the network for Short Circuit Ratio variation during transient events with the help of Region of Attraction plots. It is worth noting that previous studies in the literature have only considered LCCs, two or three-level VSCs and not Modular Multilevel Converters (MMCs) [34, 43, 82, 72]. This paper discusses the network stability of a Bipolar MMC with a metallic return. Moreover, this paper also considers frequency-dependent phase cables to study a more realistic behavior of the network. This study contributes to understanding power system stability analysis under realistic and challenging scenarios.

7.1. Direct Lyapunov function (Region of Attraction) formulation

$$\frac{d}{dt}\left(\vec{i}_{dq}\right) = \frac{\vec{v}_{dq}^{M} - \left(\omega L_{eq}^{ac} J_2 + R_{eq}^{ac} I_2\right)\vec{i}_{dq} - \vec{v}_{dq}^{G}}{L_{eq}^{ac}} \tag{7.1}$$

$$\frac{d}{dt}\left(\vec{v}_{dq}\right) = \omega J_2 \vec{v}_{dq} + \frac{N_{SM}}{C_{SM}}\vec{i}_{dq} \tag{7.2}$$

where,

$$L_{eq}^{ac} = L_r + \frac{L_{arm}}{2}, R_{eq}^{ac} = R_r + \frac{R_{arm}}{2},$$
$$J_2 = \begin{bmatrix} 0 & 1 \\ -1 & 0 \end{bmatrix} \& \; I_2 = \begin{bmatrix} 1 & 0 \\ 0 & 1 \end{bmatrix},$$

C_{SM} is the submodule capacitance and N is the number of submodules in the MMC arm.
These equations are recapitulated from Chapter 2, section 2.4.

Prior to addressing the focus of this section, formulation of the stability boundary (Region of attraction) using the Direct Lyapunov method, it is crucial to point out the fact that there is an outer or secondary stability boundary set by considering the impacts of the dq-current limiters and the threshold current values [36].

$$\begin{aligned} i_{\mathrm{d}} &= \min\left\{i_d^{ref}, i_d^{max}\right\} \\ iq &= \min\left\{i_q^{ref}, i_q^{max}\right\} \end{aligned} \tag{7.3}$$

The Lyapunov function is based on the errors of the state variables; this assumption also, by default, defines the origin as a stable operating point, which is,

$$E = \begin{bmatrix} e_1 \\ e_2 \\ e_3 \\ e_4 \\ e_5 \\ e_6 \\ e_7 \\ e_8 \end{bmatrix} = \begin{bmatrix} \vec{i}_d - \vec{i}_d^{*} \\ \vec{i}_q - \vec{i}_q^{*} \\ \vec{i}_{dB} - \vec{i}_{dB}^{*} \\ \vec{i}_{qB} - \vec{i}_{qB}^{*} \\ \vec{v}_d - \vec{v}_d^{*} \\ \vec{v}_q - \vec{v}_q^{*} \\ \vec{v}_{dB} - \vec{v}_{dB}^{*} \\ \vec{v}_{qB} - \vec{v}_{qB}^{*} \end{bmatrix}, f = \begin{bmatrix} \vec{v}_q - \vec{v}_q^{*} \\ \vec{v}_d - \vec{v}_d^{*} \\ \vec{v}_{qB} - \vec{v}_{qB}^{*} \\ \vec{v}_{dB} - \vec{v}_{dB}^{*} \end{bmatrix} \tag{7.4}$$

On substituting the error terms from Eq.(7.4) in Eq.(7.1) and Eq.(7.2), the equations obtained are,

$$\frac{d}{dt}\left(e_i\right) = \frac{\vec{v}_{dq}^{M} - \left(\omega L_{eq}^{ac} J_2 + R_{eq}^{ac} I_2\right) e_i - e_{i+4}^{G}}{L_{eq}^{ac}} \tag{7.5}$$

and,

$$\frac{d}{dt}\left(e_{i+4}\right) = \omega J_2 f_i + \frac{N_{SM}}{C_{SM}} e_i \tag{7.6}$$

Where the subscript i, in Eq. (7.5) and Eq. (7.6) are the indices that range from $1-4$, corresponding to the elements in the matrix E in Eq. (7.4). Direct Lyapunov method in the form of an energy function Eq.(5.4) is utilised to achieve the stability analysis of the transient components of the control strategies. Eq.(7.7) illustrates the conditions for the energy function to be stable using the Direct Lyapunov method.

$$\begin{aligned} W(0) &= 0 \\ W(\tilde{e}) &> 0 \quad \forall \tilde{\boldsymbol{e}} \neq 0 \\ W(\tilde{\boldsymbol{e}}) &\to \infty \text{ as } \|\tilde{\boldsymbol{e}}\| \to \infty \\ \dot{W}(\tilde{\boldsymbol{e}}) &< 0 \quad \forall \tilde{\boldsymbol{e}} \neq 0 \end{aligned} \tag{7.7}$$

The Energy function selected for this analysis is the cost function that was used for the Model Predictive Control, which is given as,

$$W(e) = E^T ME \tag{7.8}$$

where,

$$M = \begin{bmatrix} \frac{1}{2}L_{eq}^{ac} & 0 & 0 & 0 & 0 & 0 & 0 & 0 \\ 0 & \frac{1}{2}L_{eq}^{ac} & 0 & 0 & 0 & 0 & 0 & 0 \\ 0 & 0 & \frac{1}{2}L_{eq}^{ac} & 0 & 0 & 0 & 0 & 0 \\ 0 & 0 & 0 & \frac{1}{2}L_{eq}^{ac} & 0 & 0 & 0 & 0 \\ 0 & 0 & 0 & 0 & \frac{1}{2}C_{SM} & 0 & 0 & 0 \\ 0 & 0 & 0 & 0 & 0 & \frac{1}{2}C_{SM} & 0 & 0 \\ 0 & 0 & 0 & 0 & 0 & 0 & \frac{1}{2}C_{SM} & 0 \\ 0 & 0 & 0 & 0 & 0 & 0 & 0 & \frac{1}{2}C_{SM} \end{bmatrix} \tag{7.9}$$

In this case ((7.9)), M is a positive definite matrix, and its values are dependent on the MMC L_{eq}^{ac} and C_{SM} values. Eq. (7.8), when simplified, gives the Direct Lyapunov energy function [30] for the MTDC system under study, which is illustrated as

$$\begin{aligned} W(\tilde{e}) = 0.5L_{eq}^{ac}e_1^2 + 0.5L_{eq}^{ac}e_2^2 + 0.5L_{eq}^{ac}e_3^2 + 0.5L_{eq}^{ac}e_4^2 \\ +0.5C_{SM}e_5^2 + 0.5C_{SM}e_6^2 + +0.5C_{SM}e_7^2 + 0.5C_{SM}e_8^2 \end{aligned} \tag{7.10}$$

The derivative of Eq. (7.10), the Direct Lyapunov function, is as follows:

$$\begin{aligned} \frac{dW(\tilde{e})}{dt} = L_{eq}^{ac}e_1\frac{de_1}{dt} + L_{eq}^{ac}e_2\frac{de_2}{dt} + L_{eq}^{ac}e_3\frac{de_3}{dt} + L_{eq}^{ac}e_4\frac{de_4}{dt} \\ +C_{SM}e_5\frac{de_5}{dt} + C_{SM}e_6\frac{de_6}{dt} + C_{SM}e_7\frac{de_7}{dt} + C_{SM}e_8\frac{de_8}{dt} \end{aligned} \tag{7.11}$$

With the purpose of eliminating the derivative terms on the right-hand side of Eq.(7.11), Eq.(7.5) and Eq.(7.6) are substituted in Eq.(7.11), to obtain Eq. (7.12),

$$\begin{aligned} \frac{dW(\tilde{e})}{dt} = -R_{eq}^{ac}e_1^2 - R_{eq}^{ac}e_2^2 - R_{eq}^{ac}e_3^2 - R_{eq}^{ac}e_4^2 \\ + \left(-e_5 + Ne_5 + v_d^M\right)e_1 + \left(-e_6 + Ne_6 + v_q^M\right)e_2 + \left(-e_7 + Ne_7 + v_{dB}^M\right)e_3 + \left(-e_8 + Ne_8 + v_{qB}^M\right)e_4 \end{aligned} \tag{7.12}$$

$$\begin{aligned} -R_{eq}^{ac}e_1^2 < 0 \\ -R_{eq}^{ac}e_2^2 < 0 \\ -R_{eq}^{ac}e_3^2 < 0 \\ -R_{eq}^{ac}e_4^2 < 0 \end{aligned} \tag{7.13}$$

$$\begin{aligned} \left((N-1)e_5 + v_d^M\right)e_1 = \alpha_1 e_1^2 \\ \left((N-1)6_4 + v_q^M\right)e_2 = \alpha_2 e_2^2 \\ \left((N-1)e_7 + v_{dB}^M\right)e_1 = \alpha_3 e_3^2 \\ \left((N-1)e_8 + v_{qB}^M\right)e_2 = \alpha_4 e_4^2 \end{aligned} \tag{7.14}$$

Values of α_1,α_2, α_3 and α_4 were selected based on the control strategy used by an imperative iterative process, such that the derivative of the Lyapunov function is negative, creating a boundary in the shape of a circle with radius (r) of 0.3.For these conditions, the resulting Lyapunov function is semi-definite within the boundaries of the circle. The region between the circle and the boundary formed by the limiters causes sustained oscillations causing the system to be in a limit cycle [25].
Fig. 7.1, shows the stability boundary formed by the Direct Lyapunov method and the control strategy limiter boundary.

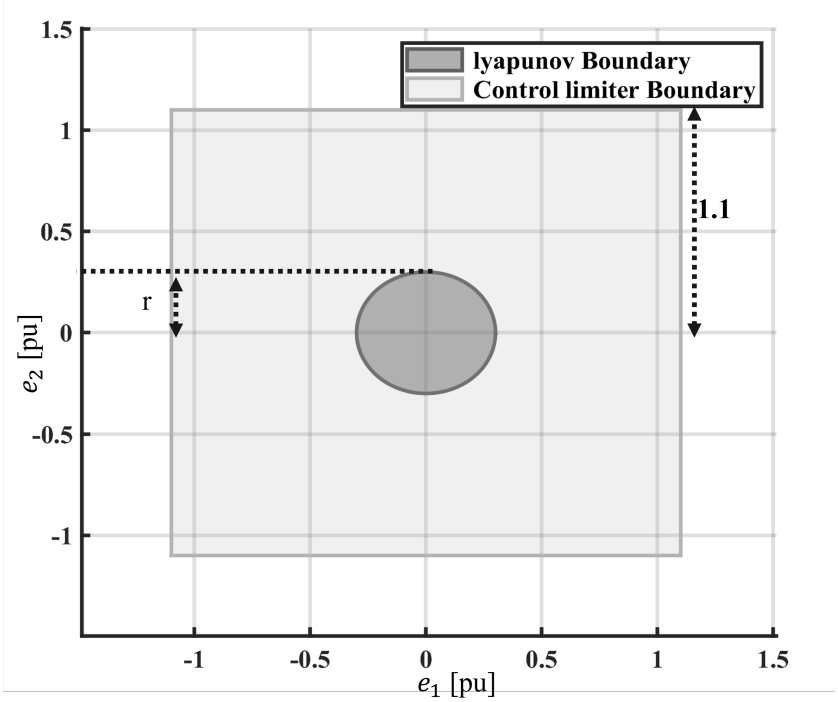

Figure 7.1: Boundary formed by the Direct Lyapunov function and the control limiter

7.2. Stability analysis

For stability analysis of the network, a transient event in the form of a phase jump in the grid AC voltage is used for the analysis. The steady-state set point of the active power is set to +0.67pu, which denotes that the MMC injects 0.67pu of active power into the AC grid under steady-state conditions. In this section, a comparison of the controllers,i.e., PI and MPC, is conducted. Both the controllers were implemented for grid-forming converters, and the analysis is presented hence.

Fig. 7.2 shows the stability analysis for a grid-forming converter with a PI-based controller. Furthermore, Fig. 7.2a, depicts the AC voltage behavior during the transient event for different SCRs. Fig. 7.2c, shows the active power behavior during the said transient event. Fig. 7.2b and Fig. 7.2d, illustrate the trajectory of the e_1 and e_2 during the transient event in three and two-dimensional depictions, respectively. In Fig. 7.2b, $SEP1$ and $SEP2$ are the initial and final Stable Equilibrium Points before and after the transient.$SEP1$ is the origin as at steady state, the errors computed in Eq. (7.4) are 0. An important observation is that the closer the point gets to the circle's boundary, the control strategies' damping capabilities decrease, and more oscillations are observed. This phenomenon will be seen more clearly in Fig. 7.3.

Fig. 7.3 shows the stability analysis for a grid-forming converter with an MPC-based controller. Furthermore, Fig. 7.3a, depicts the AC voltage behavior during the transient event for different SCRs. Fig. 7.3c shows the active power behavior during the said transient event. Fig. 7.3b and Fig. 7.3d, illustrate the trajectory of the e_1 and e_2 during the transient event in three and two-dimensional depictions, respectively. In Fig. 7.3b, $SEP1$ and $SEP2$ are the initial and final Stable Equilibrium Points before and after the transient.$SEP1$ is the origin as at steady state, the errors computed in Eq. (7.4) are 0. An important observation is that the closer the point gets to the boundary of the circle, the damping capabilities of the control strategies decrease, and more oscillations are observed, as seen in Fig. 7.3.

In Fig. 7.4, for lower SCRs, the limit cycle phenomenon becomes more clear as the trajectories formed by e_1 and e_2 go beyond the circle for the majority part of its course as seen from Fig. 7.4b and Fig. 7.4d. This can also be seen in Fig. 7.4a, in the form of the V_{rms} voltage waveform. Furthermore, it can also be seen from Fig. 7.4c that the converter cannot match its active power set point after the clearance of the transient event. This strengthens the observation of the damping effect getting reduced as the trajectories of e_1 and e_2 get further from the boundary of the circle. It is also observed that for SCR 2 in Fig. 7.4b and Fig. 7.4d that the system becomes momentarily unstable as the trajectory goes beyond

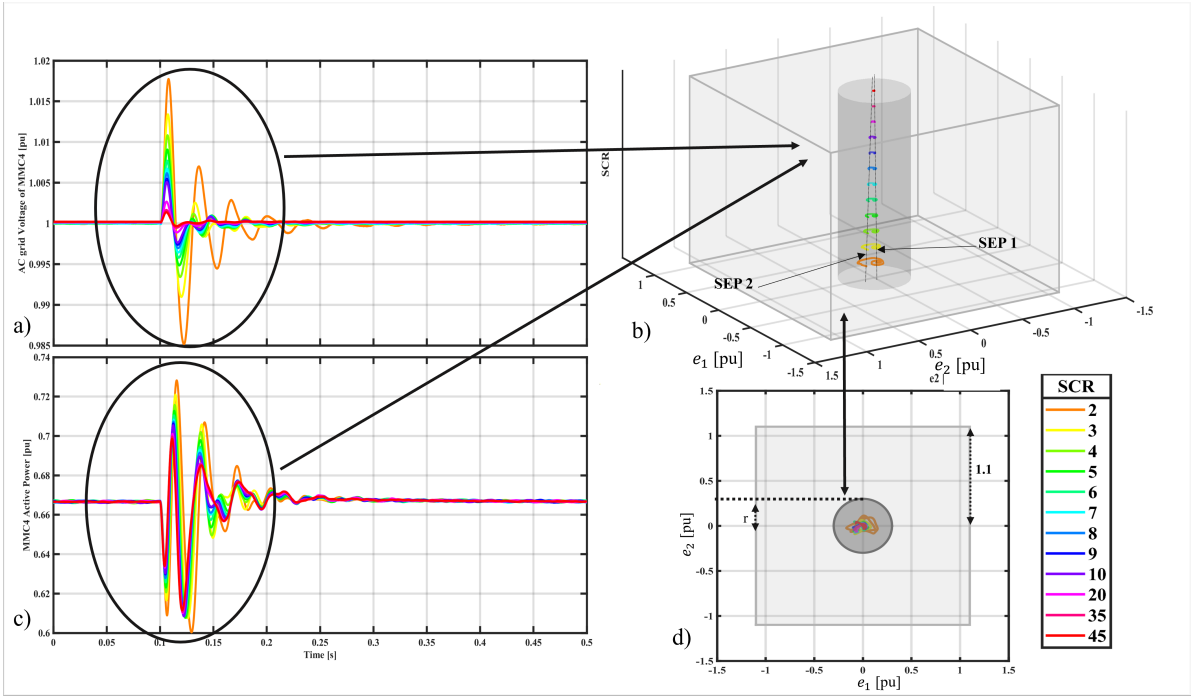

Figure 7.2: Large Signal stability analysis for the PI-based Grid forming converter. (a) shows the AC voltage behavior, (b) shows the 3-dimensional trajectory of e_1 and e_2, (c) shows the Active Power waveforms, (d) shows the 2-dimensional trajectory of e_1 and e_2

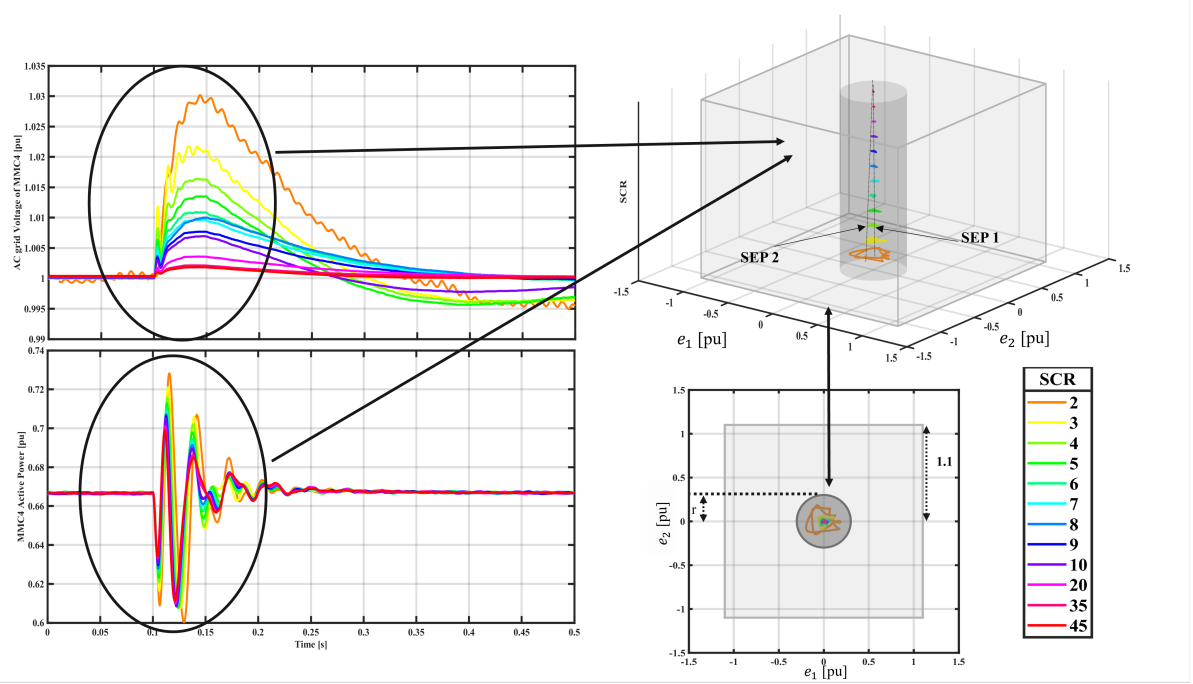

Figure 7.3: Large Signal stability analysis for the MPC-based Grid forming converter. (a) shows the AC voltage behavior, (b) shows the 3-dimensional trajectory of e_1 and e_2, (c) shows the Active Power waveforms, (d) shows the 2-dimensional trajectory of e_1 and e_2

the boundary of the control limiters. In this case, there is an Unstable Point ($UP2$), as the endpoint is beyond the boundary of the circle.

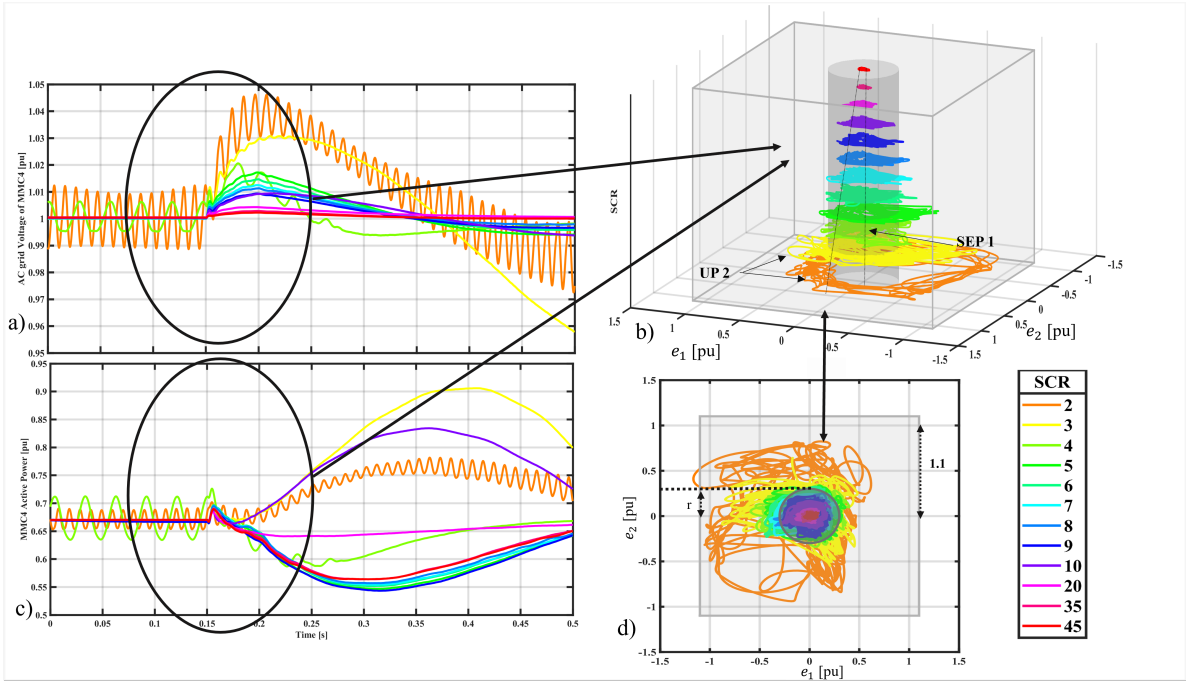

Figure 7.4: Large Signal stability analysis for Unstable case. (a) shows the AC voltage behavior, (b) shows the 3-dimensional trajectory of e_1 and e_2, (c) shows the Active Power waveforms, (d) shows the 2-dimensional trajectory of e_1 and e_2

8
Conclusion

8.1. Thesis Summary

This thesis aimed to enhance the robustness of the HVDC network by implementing grid-forming control strategies and Model Predictive Control (MPC) techniques. The successful implementation of these strategies has the potential to advance the HVDC transmission system control and protection field. The research objectives outlined in Chapter 1 were accomplished, leading to the successful completion of this thesis. The implementation of grid-forming control strategies, as opposed to conventional grid-following control strategies, has proven to be effective in increasing the response speed of the control system. Furthermore, using MPC instead of traditional PI-based controllers has improved the system's response speed while maintaining stability. These advancements in control strategies have generated the potential for further research and development in the HVDC transmission system control and protection field. Overall, this thesis has contributed to advancing HVDC technology and its potential for future applications.

The development of a ±525kV four-terminal HVDC network with MMCs in Bipolar configuration and metallic return was completed, and it was discovered that there was an imbalance in the cable currents after the fault was cleared. To address this issue, a novel controller was developed for the metallic return, successfully controlling the current in the metallic return during normal operating conditions to zero. This was the first controller of its kind, as the metallic return is typically left uncontrolled.

Next, grid-forming control strategies were implemented to replace the existing grid following topologies to enhance the network's robustness and resilience. Two grid-forming strategies, grid-forming droop and the Virtual Synchronous Machine (VSM), were implemented and tested to compare their capabilities. The VSM was found to be best suited for the network due to its artificial inertia characteristic, which helped dampen the oscillations. A modified version of the VSM was also used with a cascaded current control algorithm, allowing the onshore grid-forming converter to have current limiting capabilities.

To balance the internal currents of the MMC stations and minimise internal losses, the conventional Circulating Current Suppression Control was replaced with an Energy-based CCSC. The new control effectively addressed the circulating current and balanced the arm currents.

Both the VSM grid-forming control and the Energy-based CCSC were implemented and tested under various grid impedances by varying the SCR of the grid to replicate scenarios in which the AC grid would become weak. To increase the response speed of the control strategies, a Model Predictive Controller (MPC) was used to replace the conventional PI-based controllers. The MPC block was formulated by selecting a suitable cost function and forming constraints appropriate for the application in this network. Upon implementation of the MPC, it was observed that the control strategies reacted faster than the ones with PI-based controllers, with some oscillations within the TSOs' set threshold.

A large stability analysis was conducted on the MMC station using a Lyapunov Energy function based on the cost function of the MPC block. A direct Lyapunov method was used to assess the transient stability of the converters. Overall, the successful implementation of these control strategies and controllers has the potential to advance the HVDC transmission system control and protection field.

Considering the information discussed thus far, it can be concluded that Model Predictive Control for Grid forming control strategies implemented in an MMC-based Multi-terminal DC network improves the network's response speed.

8.2. Future Work or Future Research Direction

The CCSC implemented in this thesis couples the current and voltage variables of the MMC. An energy control based on the decoupled current and voltage would perform much better than the control that was implemented in this thesis.
Fine-tuning the MPC is required to remove the oscillations observed upon conducting a Fast Fourier Transform for lower SCRs 1 and 2.

References

[1] WG B4.57. *Guide for the Development of Models for HVDC Converters in a HVDC Grid*. Brochure. 2014. URL: https://e-cigre.org/publication/804-dc-grid-benchmark-models-for-system-studies.

[2] WG B4.70. *Guide for electromagnetic transient studies involving VSC converters*. Brochure. 2021. URL: https://e-cigre.org/publication/832-guide-for-electromagnetic-transient-studies-involving-vsc-converters.

[3] WG B4.72. *DC grid benchmark models for system studies*. Brochure. 2020. URL: https://e-cigre.org/publication/604-guide-for-the-development-of-models-for-hvdc-converters-in-a-hvdc-grid.

[4] Gilbert Bergna-Diaz et al. "Generalized voltage-based state-space modeling of modular multilevel converters with constant equilibrium in steady state". In: *IEEE Journal of Emerging and Selected Topics in Power Electronics* 6.2 (2018), pp. 707–725.

[5] L. Cai, U. Karaagac, and J. Mahseredjian. "Simulation of Startup Sequence of an Offshore Wind Farm With MMC-HVDC Grid Connection". In: *IEEE Transactions on Power Delivery* 32.2 (2017), pp. 638–646. DOI: 10.1109/TPWRD.2016.2517184.

[6] Rashid Hussain Chandio et al. "Control and protection of MMC-based HVDC systems: A review". In: *Energy Reports* 9 (2023), pp. 1571–1588. ISSN: 2352-4847. DOI: https://doi.org/10.1016/j.egyr.2022.12.056. URL: https://www.sciencedirect.com/science/article/pii/S2352484722026567.

[7] Huijie Cheng et al. "Transient Angle Stability of Paralleled Synchronous and Virtual Synchronous Generators in Islanded Microgrids". In: *IEEE Transactions on Power Electronics* 35.8 (Aug. 2020), pp. 8751–8765. ISSN: 0885-8993, 1941-0107. DOI: 10.1109/TPEL.2020.2965152. URL: https://ieeexplore.ieee.org/document/8954818/ (visited on 05/22/2023).

[8] Hanspeter Fassler Claudio Facchin. *ABB Review: Special Report 60 years of HVDC*. Review brochure. 2006. URL: https://library.e.abb.com/public/aff841e25d8986b5c1257d380045703f/140818/%5C%20ABB%5C%20SR%5C%2060%5C%20years%5C%20of%5C%20HVDC_72dpi.pdf.

[9] Carlos Collados-Rodriguez et al. "Integration of an MMC-HVDC Link to the Existing LCC-HVDC Link in Balearic Islands Based on Grid-Following and Grid-Forming Operation". In: *IEEE Transactions on Power Delivery* 37.6 (2022), pp. 5278–5288.

[10] Salvatore D'Arco, Jon Are Suul, and Olav B. Fosso. "Small-signal modeling and parametric sensitivity of a virtual synchronous machine in islanded operation". In: *International Journal of Electrical Power & Energy Systems* 72 (Nov. 2015), pp. 3–15. ISSN: 01420615. DOI: 10.1016/j.ijepes.2015.02.005. URL: https://linkinghub.elsevier.com/retrieve/pii/S0142061515000885 (visited on 06/07/2023).

[11] B De Schutter and T Van Den Boom. "Model predictive control for discrete-event and hybrid systems". In: *Proceedings of the 42nd IEEE Conference on Decision and Control*. 2003.

[12] Apparao Dekka et al. "Model Predictive Control of High-Power Modular Multilevel Converters - An Overview". In: *IEEE Journal of Emerging and Selected Topics in Power Electronics* 7 (1 Mar. 2019), pp. 168–183. ISSN: 21686785. DOI: 10.1109/JESTPE.2018.2880137.

[13] Fujin Deng et al. "Circulating Current Suppression for MMC-HVDC Systems with Asymmetric Arm Impedance". In: *CSEE Journal of Power and Energy Systems* 7.3 (2020), pp. 530–540.

[14] Fujin Deng et al. "Circulating current suppression for MMC-HVDC systems with asymmetric arm impedance". In: *CSEE Journal of Power and Energy Systems* 7 (3 May 2021), pp. 530–540. ISSN: 20960042. DOI: 10.17775/CSEEJPES.2019.02690.

[15] Sixing Du et al. *Modular multilevel converters: analysis, control, and applications*. John Wiley & Sons, 2018.

[16] ENTSO-E. *HVDC Links in System Operators*. Technical Paper. 2019.

[17] Muhammad Hassan Fidai et al. "Real-time implementation of optimal power flow calculator for hvdc grids". In: *Cigre Lund* 2015 (2015).

[18] Julian Freytes. *Small-signal stability analysis of Modular Multilevel Converters and application to MMC–based Multi-Terminal DC grids*. PhDthesis. 2017. URL: https://tel.archives-ouvertes.fr/tel-01806049v2/file/Freytes_Julian_DLE.pdf.

[19] Julian Freytes et al. "Dynamic impact of MMC controllers on DC voltage droop controlled MTDC grids". In: *2016 18th European Conference on Power Electronics and Applications (EPE'16 ECCE Europe)*. IEEE. 2016, pp. 1–10.

[20] Julian Freytes et al. "Grid-Forming Control with Current Limitation for MMC under Unbalanced Fault Ride-Through". In: *IEEE Transactions on Power Delivery* 36 (3 June 2021), pp. 1914–1916. ISSN: 19374208. DOI: 10.1109/TPWRD.2021.3053148.

[21] Julian Freytes et al. "Improving Small-Signal Stability of an MMC With CCSC by Control of the Internally Stored Energy". In: *IEEE Transactions on Power Delivery* 33.1 (Feb. 2018), pp. 429–439. ISSN: 0885-8977, 1937-4208. DOI: 10.1109/TPWRD.2017.2725579. URL: http://ieeexplore.ieee.org/document/7973100/ (visited on 06/07/2023).

[22] Guige Gao et al. "Circulating Current Suppression Strategy of Modular Multilevel Converter Based on Model Predictive Control". In: *E3S Web of Conferences*. Vol. 261. EDP Sciences. 2021, p. 01035.

[23] Temesgen Haileselassie and Kjetil Uhlen. "Power system security in a meshed north sea HVDC grid". In: *Proceedings of the IEEE* 101 (Apr. 2013), pp. 978–990. DOI: 10.1109/JPROC.2013.2241375.

[24] Lennart Harnefors et al. "Dynamic analysis of modular multilevel converters". In: *IEEE Transactions on Industrial Electronics* 60.7 (2012), pp. 2526–2537.

[25] Karina Hellevik and Ove Tobias Gudmestad. "Limit cycle oscillations at resonances". In: *IOP Conference Series: Materials Science and Engineering*. Vol. 276. 1. IOP Publishing. 2017, p. 012020.

[26] Michiel Houwing, Rudy R Negenborn, and Bart De Schutter. "Economic advantages of applying model predictive control to distributed energy resources: The case of micro-CHP systems". In: *2008 16th Mediterranean Conference on Control and Automation*. IEEE. 2008, pp. 1550–1555.

[27] Ying Huang et al. "Research on Startup Circuit Parameter Selection and Startup Control Strategy for Multi-Terminal VSC HVDC System". In: (2019), pp. 1–7. DOI: 10.1049/cp.2019.0309.

[28] S. H. S. Ibrahim. *The case for a strong grid: How grid strength would be essential in planning for a Carbon Free Future*. LinkedIn article. 2021. URL: https://www.linkedin.com/pulse/case-%20strong-grid-how-strength-would-essential-carbon-syed-ibrahim/..

[29] Distribution Committee of the IEEE Power and Energy Society. *IEEE Recommended Practice and Requirements for Harmonic Control in Electric Power Systems Sponsored by the Transmission and Distribution Committee IEEE Power and Energy Society*. 2014.

[30] Reza Janbazi Ghadi et al. "Lyapunov theory-based control strategy for multi-terminal MMC-HVDC systems". In: *International Journal of Electrical Power & Energy Systems* 129 (July 2021), p. 106778. ISSN: 01420615. DOI: 10.1016/j.ijepes.2021.106778. URL: https://linkinghub.elsevier.com/retrieve/pii/S0142061521000181 (visited on 05/14/2023).

[31] C.B. Kadu and C.Y. Patil. "Design and Implementation of Stable PID Controller for Interacting Level Control System". In: *Procedia Computer Science* 79 (2016). Proceedings of International Conference on Communication, Computing and Virtualization (ICCCV) 2016, pp. 737–746. ISSN: 1877-0509. DOI: https://doi.org/10.1016/j.procs.2016.03.097. URL: https://www.sciencedirect.com/science/article/pii/S1877050916002283.

[32] Prabha Kundur et al. "Definition and classification of power system stability IEEE/CIGRE joint task force on stability terms and definitions". In: *IEEE transactions on Power Systems* 19.3 (2004), pp. 1387–1401.

[33] Meiyi Li et al. "Lyapunov-Based Large Signal Stability Assessment for VSG Controlled Inverter-Interfaced Distributed Generators". In: *Energies* 11.9 (Aug. 29, 2018), p. 2273. ISSN: 1996-1073. DOI: 10.3390/en11092273. URL: http://www.mdpi.com/1996-1073/11/9/2273 (visited on 05/26/2023).

[34] Xilin Li et al. "An Iterative Equal Area Criterion for Transient Stability Analysis of Grid-tied Converter Systems with Varying Damping". In: *IEEE Transactions on Power Systems* (2023), pp. 1–13. ISSN: 0885-8950, 1558-0679. DOI: 10.1109/TPWRS.2023.3241079. URL: https://ieeexplore.ieee.org/document/10032630/ (visited on 05/22/2023).

[35] Xinwei Li, Chongru Liu, and YuanYuan Lou. "Start-up and recovery method with LCC-HVDC systems participation during AC/DC system black-starts". In: *IET Generation, Transmission & Distribution* 14.3 (2020), pp. 362–367.

[36] Yingbiao Li et al. "PLL synchronization stability analysis of MMC-connected wind farms under high-impedance AC faults". In: *IEEE Transactions on Power Systems* 36.3 (2020), pp. 2251–2261.

[37] Kang Liu and Guige Gao. "Circulating Current Suppression Strategy of Modular Multilevel Converter Based on Model Predictive Control". In: vol. 261. EDP Sciences, May 2021. DOI: 10.1051/e3sconf/202126101035.

[38] Le Liu, Ajay Shetgaonkar, and Aleksandra Lekić. "Interoperability of classical and advanced controllers in MMC based MTDC power system". In: *International Journal of Electrical Power and Energy Systems* 148 (June 2023). ISSN: 01420615. DOI: 10.1016/j.ijepes.2023.108980.

[39] Siyuan Liu, Ajay Shetgaonkar, and Marjan Popov. "Coordinative performance of HVDC circuit breakers in MTDC grids". In: *2020 IEEE Power & Energy Society General Meeting (PESGM)*. 2020, pp. 1–5. DOI: 10.1109/PESGM41954.2020.9281921.

[40] Siyuan Liu et al. "Modeling, experimental validation, and application of VARC HVDC circuit breakers". In: *IEEE Transactions on Power Delivery* 35.3 (2019), pp. 1515–1526.

[41] Wenxia Liu et al. "Reliability assessment of power systems with photovoltaic power stations based on intelligent state space reduction and pseudo-sequential Monte Carlo simulation". In: *Energies* 11.6 (2018), p. 1431.

[42] Luís FN Lourenço et al. "Stability analysis of grid-forming MMC-HVDC transmission connected to legacy power systems". In: *Energies* 14.23 (2021), p. 8017.

[43] Rui Ma et al. "Generalized Swing Equation and Transient Synchronous Stability With PLL-Based VSC". In: *IEEE Transactions on Energy Conversion* 37.2 (June 2022), pp. 1428–1441. ISSN: 0885-8969, 1558-0059. DOI: 10.1109/TEC.2021.3137806. URL: https://ieeexplore.ieee.org/document/9662209/ (visited on 05/22/2023).

[44] Jan Machowski et al. *Power system dynamics: stability and control*. John Wiley & Sons, 2020.

[45] T Maguire et al. "Efficient techniques for real time simulation of MMC systems". In: *Proc. Int. Conf. Power Syst. Transients (IPST)*. 2013, pp. 1–7.

[46] Paul McNamara and Federico Milano. "Model predictive control-based AGC for multi-terminal HVDC-connected AC grids". In: *IEEE Transactions on Power Systems* 33.1 (2017), pp. 1036–1048.

[47] Nabil Mohammed, Weihua Zhou, and Behrooz Bahrani. "Comparison of PLL-Based and PLL-Less Control Strategies for Grid-Following Inverters Considering Time and Frequency Domain Analysis". In: *IEEE Access* 10 (2022), pp. 80518–80538. DOI: 10.1109/ACCESS.2022.3195494.

[48] Nabil Mohammed, Weihua Zhou, and Behrooz Bahrani. "Comparison of PLL-Based and PLL-Less Control Strategies for Grid-Following Inverters Considering Time and Frequency Domain Analysis". In: *IEEE Access* 10 (2022), pp. 80518–80538. ISSN: 21693536. DOI: 10.1109/ACCESS.2022.3195494.

[49] Ji Woo Moon et al. "Circulating current control in MMC under the unbalanced voltage". In: *IEEE Transactions on Power Delivery* 28 (3 2013), pp. 1952–1959. ISSN: 08858977. DOI: 10.1109/TPWRD.2013.2264496.

[50] Rayane Mourouvin et al. "Real-time Hierarchical MPC Applied to an MMC in Grid-Forming Mode: Implementation and Validation in Power Hardware-in-the-Loop". In: *IEEE Transactions on Power Delivery* (2023).

[51] Mario Ndreko et al. “On grid code compliance of offshore mtdc grids: modeling and analysis”. In: *2015 IEEE Eindhoven PowerTech*. 2015, pp. 1–6. DOI: 10.1109/PTC.2015.7232398.

[52] *PROMOTiON D7.4 Economic Framework for a Meshed Offshore Grid*. Brochure. 2019. URL: https://www.promotion-offshore.net/results/deliverables/.

[53] Taoufik Qoria et al. “Direct AC voltage control for grid-forming inverters”. In: *Journal of Power Electronics* 20.1 (Jan. 2020), pp. 198–211. ISSN: 1598-2092, 2093-4718. DOI: 10.1007/s43236-019-00015-4. URL: http://link.springer.com/10.1007/s43236-019-00015-4 (visited on 06/07/2023).

[54] Taoufik Qoria et al. “Grid-Forming Control With Decoupled Functionalities for High-Power Transmission System Applications”. In: *IEEE Access* 8 (2020), pp. 197363–197378. DOI: 10.1109/access.2020.3034149Ãŕ. URL: https://hal.archives-ouvertes.fr/hal-03703440.

[55] Pierre Rault et al. “Coordinated control for multi terminal DC grids connected to offshore wind farms”. In: *2016 IEEE 17th Workshop on Control and Modeling for Power Electronics (COMPEL)*. IEEE. 2016, pp. 1–8.

[56] Ali Raza et al. “HVDC Circuit Breakers: Prospects and Challenges”. In: *Applied Sciences* 11.11 (2021), p. 5047.

[57] Joan Rocabert et al. “Control of power converters in AC microgrids”. In: *IEEE transactions on power electronics* 27.11 (2012), pp. 4734–4749.

[58] Jose Rodriguez and Patricio Cortes. *Predictive control of power converters and electrical drives*. John Wiley & Sons, 2012.

[59] P. Rodriguez and N. B. Lai. *Grid-following and grid-forming PV and wind turbines*. Jan. 2021. DOI: 10.1016/B978-0-12-819432-4.00022-6.

[60] Ebrahim Rokrok. “Grid-forming control strategies of power electronic converters in transmission grids: application to HVDC link”. PhD thesis. Aug. 2022.

[61] Ebrahim Rokrok et al. *Effect of Using PLL-Based Grid-Forming Control on Active Power Dynamics Under Various SCR*.

[62] Hani Saad et al. “MMC capacitor voltage decoupling and balancing controls”. In: *IEEE Transactions on Power Delivery* 30.2 (2014), pp. 704–712.

[63] Hani Aziz Saad. “Modélisation et simulation d’une liaison HVDc de type VSC-MMC”. PhD thesis. École Polytechnique de Montréal, 2015.

[64] Ajay Shetgaonkar. *Technical performance of different DC CB technologies for future HVDC Grids*. PhDthesis. 2020. URL: https://repository.tudelft.nl/islandora/object/uuid:4ee00c88-3f7d-4bb0-9433-b237b813e0d3?collection=education.

[65] Ajay Shetgaonkar et al. “Microsecond Enhanced Indirect Model Predictive Control for Dynamic Power Management in MMC Units”. In: *Energies* 14.11 (2021). ISSN: 1996-1073. DOI: 10.3390/en14113318.

[66] Ajay Shetgaonkar et al. “Microsecond enhanced indirect model predictive control for dynamic power management in MMC units”. In: *Energies* 14.11 (2021), p. 3318.

[67] Ajay Shetgaonkar et al. “Model predictive control and protection of MMC-based MTDC power systems”. In: *International Journal of Electrical Power & Energy Systems* 146 (2023), p. 108710.

[68] Ajay Shetgaonkar et al. *Zero-current Suppression Control for Fault Current Damper based on Model Predictive Control*.

[69] Ali Reza Sobbouhi and Abolfazl Vahedi. “Transient stability prediction of power system; a review on methods, classification and considerations”. In: *Electric Power Systems Research* 190 (Jan. 2021), p. 106853. ISSN: 03787796. DOI: 10.1016/j.epsr.2020.106853. URL: https://linkinghub.elsevier.com/retrieve/pii/S0378779620306520 (visited on 06/07/2023).

[70] C. E. Spallarossa et al. “A DC voltage control strategy for MMC MTDC grids incorporating multiple master stations”. In: *2014 IEEE PES T&D Conference and Exposition*. 2014, pp. 1–5. DOI: 10.1109/TDC.2014.6863534.

[71] Georgios Stamatiou. "Techno-Economical Analysis of DC Collection Grid for Offshore Wind Parks". PhD thesis. Sept. 2010. DOI: 10.13140/RG.2.1.1902.6649.

[72] Yingjie Tang et al. "An Improved Equal Area Criterion for Transient Stability Analysis of Converter-Based Microgrid Considering Nonlinear Damping Effect". In: *IEEE Transactions on Power Electronics* 37.9 (Sept. 2022), pp. 11272–11284. ISSN: 0885-8993, 1941-0107. DOI: 10.1109/TPEL.2022.3164687. URL: https://ieeexplore.ieee.org/document/9749883/ (visited on 05/22/2023).

[73] Qoria Taoufik et al. "Direct AC Voltage Control for Grid-Forming Inverters". In: *Journal of power electronics* (Dec. 2019). DOI: 10.1007/s43236-019-00015-4.

[74] Kamran Sharifabadi; Lennart Harnefors; Hans-Peter Nee; Staffan Norrga; Remus Teodorescu. *Design, Control, and Application of Modular Multilevel Converters for HVDC Transmission Systems | IEEE eBooks | IEEE Xplore*. 2016. ISBN: 9781118851555. URL: https://ieeexplore.ieee.org/book/7601527.

[75] Sönke Thomsen, Nils Hoffmann, and Friedrich Wilhelm Fuchs. "PI Control, PI-Based State Space Control, and Model-Based Predictive Control for Drive Systems With Elastically Coupled Loads—A Comparative Study". In: *IEEE Transactions on Industrial Electronics* 58.8 (2011), pp. 3647–3657. DOI: 10.1109/TIE.2010.2089950.

[76] Giuseppe Marco Tina et al. "Comparative Technical-Economical Analysis of Transient Stability Improvements in a Power System". In: *Applied Sciences* 11.23 (Dec. 1, 2021), p. 11359. ISSN: 2076-3417. DOI: 10.3390/app112311359. URL: https://www.mdpi.com/2076-3417/11/23/11359 (visited on 06/08/2023).

[77] Qingrui Tu et al. "Suppressing DC voltage ripples of MMC-HVDC under unbalanced grid conditions". In: *IEEE Transactions on Power delivery* 27.3 (2012), pp. 1332–1338.

[78] Ahmad Usman, Mahir Kutay, and Tuncay Ercan. "MATLAB/SIMULINK Model For HVDC Fault Calculations". In: Sept. 2019. DOI: 10.1109/ACEMP-OPTIM44294.2019.9007154.

[79] Jinyu Wang et al. "Circulating Current Suppression for MMC-HVDC under Unbalanced Grid Conditions". In: *IEEE Transactions on Industry Applications* 53.4 (Mar. 2017), pp. 1–1. DOI: 10.1109/TIA.2017.2675992.

[80] Puyu Wang et al. "Start-up Control of an Offshore Integrated MMC Multi-Terminal HVDC System with reduced DC Voltage". In: *IEEE Transactions on Power Systems* 31.4 (2015), pp. 2740–2751.

[81] Xiongfei Wang et al. "Grid-synchronization stability of converter-based resources— An overview". In: *IEEE Open Journal of Industry Applications* 1 (2020), pp. 115–134.

[82] Yiming Wang et al. "Transient Stability Analysis and Improvement for the Grid-Connected VSC System with Multi-Limiters". In: *IEEE Transactions on Power Systems* (2023), pp. 1–16. ISSN: 0885-8950, 1558-0679. DOI: 10.1109/TPWRS.2023.3245806. URL: https://ieeexplore.ieee.org/document/10045813/ (visited on 05/14/2023).

[83] Martin Westman and Ellen Nordén. *Modeling and comparative analysis of different grid-forming converter control concepts for very low inertia systems*. 2020.

[84] Huaitian Zhang et al. "Circulating Current Control scheme of Modular Multilevel Converters supplying passive networks under Unbalanced Load conditions". In: *Electric Power Systems Research* 171 (2019), pp. 36–46.

[85] Mingguang Zhang et al. "MMC-HVDC circulating current suppression method based on improved proportional resonance control". In: *Energy Reports* 6 (Dec. 2020), pp. 863–871. ISSN: 23524847. DOI: 10.1016/j.egyr.2020.11.120. URL: https://linkinghub.elsevier.com/retrieve/pii/S2352484720315456 (visited on 06/21/2023).

[86] Guanyu Zhou and Wenzhong Ma. "Model predictive control-based coordinated control strategy for VSC-MTDC systems". In: *2019 22nd International Conference on Electrical Machines and Systems (ICEMS)*. IEEE. 2019, pp. 1–5.

A
Supplementary Information

A.1. SubModule Capacitance Formula

The formula to calculate the Submodule Capacitance of the MMCs in-order to reduce the ripple voltage is given as:

$$C = \frac{2SE}{6N_{sm}v_c^2}$$

where, S, is the power rating of the MMC or transformer.
E, or E_{MMC} is the energy of the capacitor is each MMC.
N_{sm}, is the number of submodules in each leg of the MMC.
V_c, is the voltage across the capacitor, given by:

$$V_C = \frac{V_{dc}}{N_{sm}}$$

From the CIGRE models produced by **WG B4.57 in TB 604**, the SM capacitor is selected to try to keep the ripple for the SM voltage within 10%. It is decided that the energy for each SM would be $30kJ/MVA$.

A.2. ABC-dq transformation

The Direct-quadrature (dqz) transforms are also known as the Clarke-park transforms. They transform the three-phase Voltage and Current from ABC domain to dqz such that they become DC quantities making the control logic and the analysis easier. This is done by imposing the three-phase quantities into a Synchronous Rotating Reference Frame, which rotates at the nominal frequency, removing the rotating aspect of the signals and making it easy to apply. The transforms are given as,

$$\begin{bmatrix} v_{\mathrm{d}} \\ v_{\mathrm{q}} \\ v_{\mathrm{z}} \end{bmatrix} = \sqrt{\frac{2}{3}} \begin{bmatrix} \cos\theta & \cos\left(\theta - \frac{2\pi}{3}\right) & \cos\left(\theta + \frac{2\pi}{3}\right) \\ -\sin\theta & -\sin\left(\theta - \frac{2\pi}{3}\right) & -\sin\left(\theta + \frac{2\pi}{3}\right) \\ \frac{1}{\sqrt{2}} & \frac{1}{\sqrt{2}} & \frac{1}{\sqrt{2}} \end{bmatrix} \begin{bmatrix} v_a \\ v_{\mathrm{b}} \\ v_{\mathrm{c}} \end{bmatrix} \tag{A.1}$$

B
Additional figures

B.1. Chapter 3

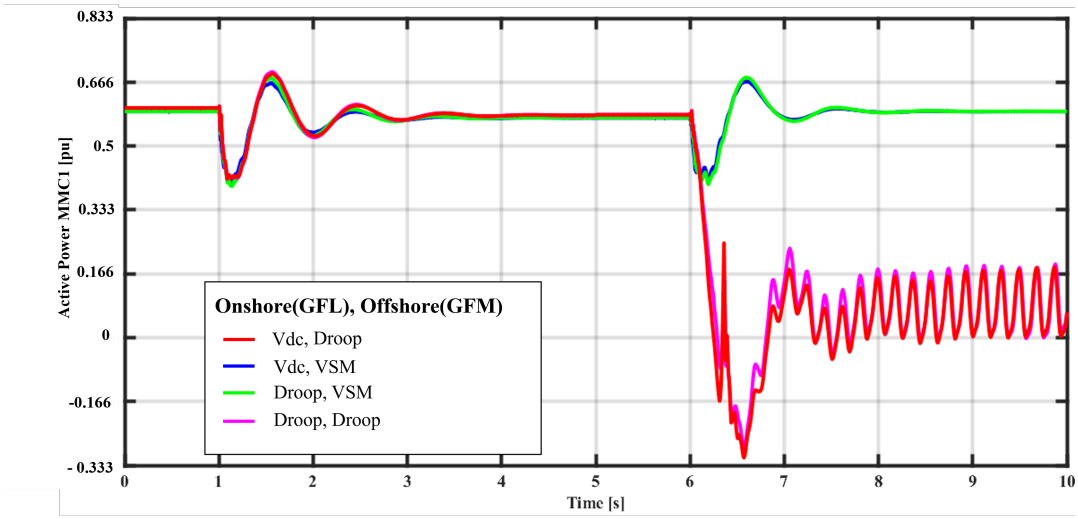

Figure B.1: Active power MMC1

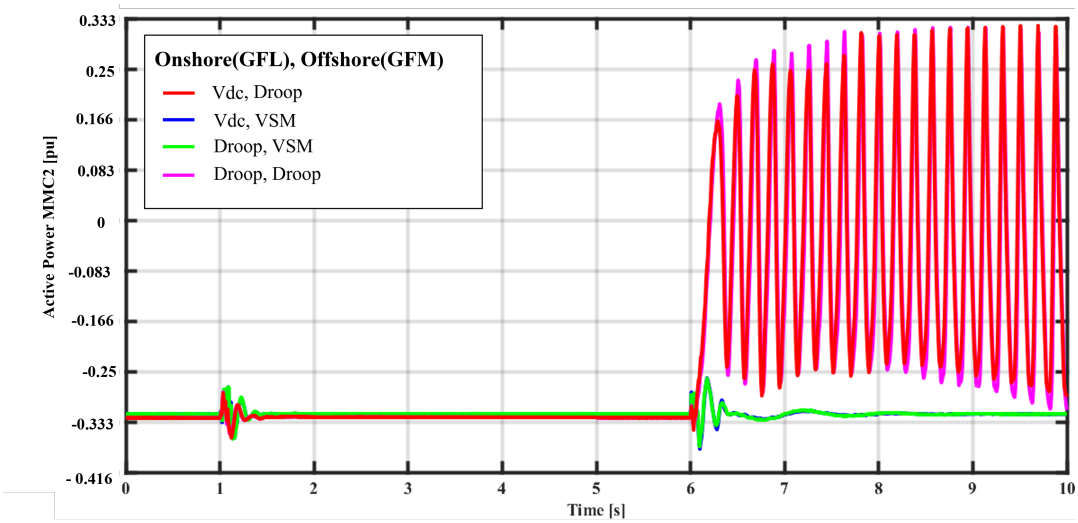

Figure B.2: Active power MMC2

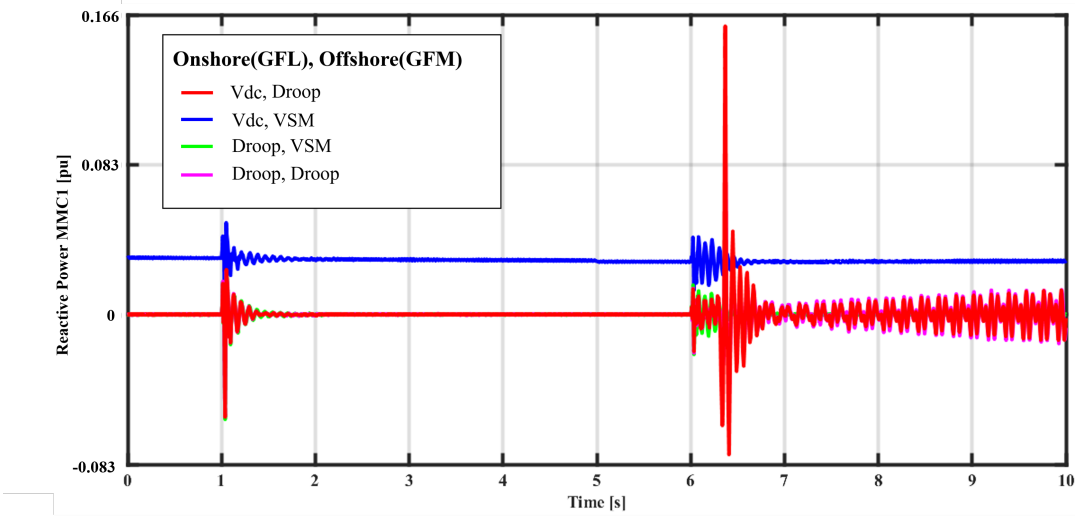

Figure B.3: Reactive power MMC1

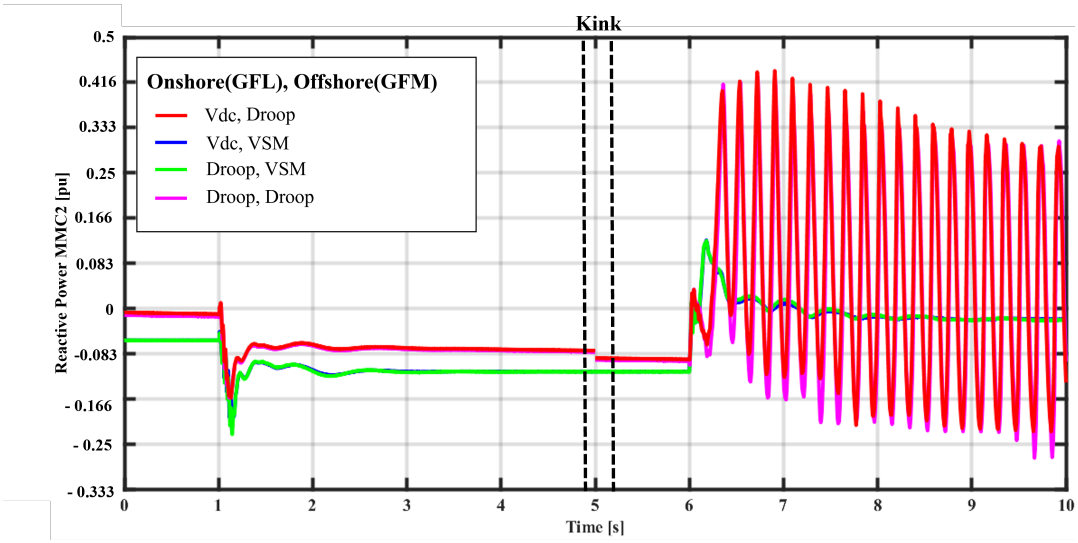

Figure B.4: Reactive power MMC2

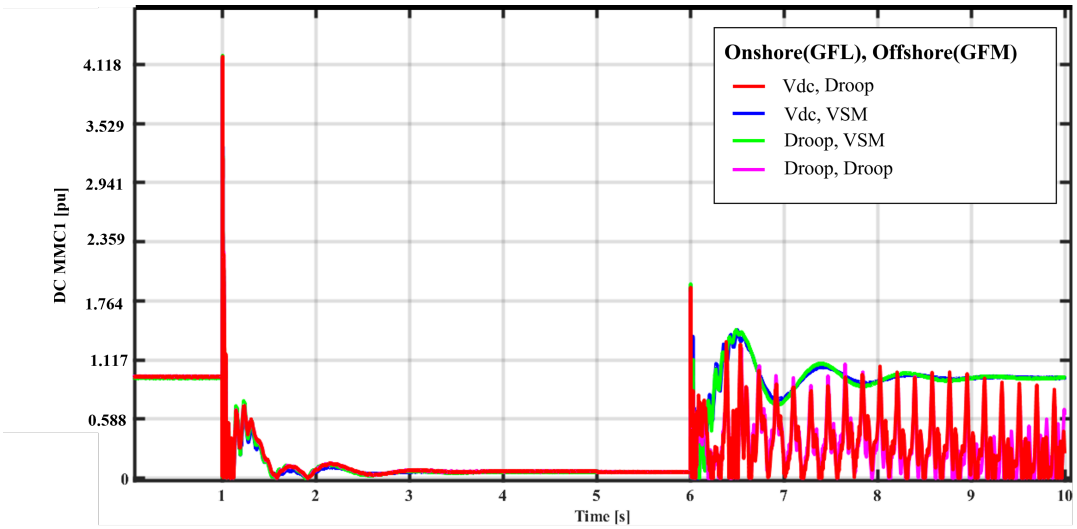

Figure B.5: Direct Current MMC1

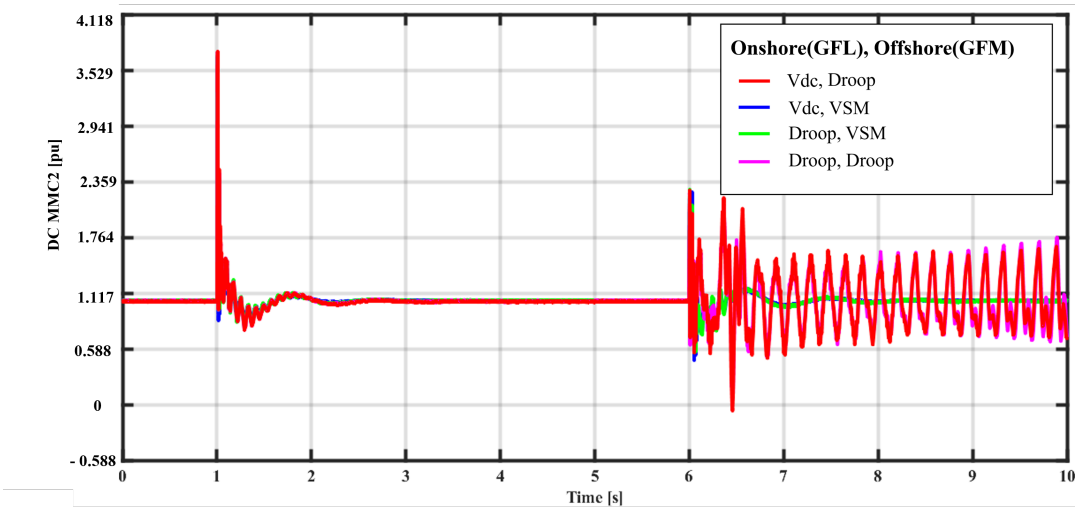

Figure B.6: Direct Current MMC2

C

Supplementary details regarding modelling in RTDS

C.1. Time steps in RSCAD/RTDS

C.1.1. General Operations

Based on the calculation time-step and network details, the following categories have been used in modelling this HVDC network in the RTDS® software.

1. Main step (default)
2. Small time step (small dt)
3. Sub step
4. Super step

Main step

The default RSCAD simulation environment is in mainstep. The simulation time-step typically ranges from $30 - 60\mu s$. But, the simulation time-step could go upto $80\mu s$ but the results are subject to the outcomes if a slower simulation time-step.

Small Time step

Typical time steps for EMTP-type simulations are on the order of 50 microseconds. Such time steps, however, are not sufficiently small enough to allow for the accurate simulation of high-frequency switching circuits such as those used in many Power electronic schemes. In order to model such schemes, a feature known as small time-step simulation was introduced into RSCAD. Small time-step (small dt) simulation uses several 'shortcuts' to reduce the timestep to somewhere in the neighbourhood of 1.5 to 3.75 microseconds. Each small dt circuit is solved as a sub-network that can be interfaced to the main network solution. The small dt tab in the RSCAD master library contains the small dt components.

Sub step

With the vast increase in processing power introduced with the POWER8 processor cores used by the RTDS® NovaCor simulator, it is possible that networks of a certain size can have their Nodal Admittance Matrix (NAM) decomposed in real time with much smaller timesteps than the main time-step (main step). The Substep feature enables the user to model part of a network with a time-step much smaller than mainstep to get higher resolution results. Substep simulation executes the contents of a hierarchy box multiple times every main step. Substep supports the use of resistive switching to model power electronic switches as opposed to the LC Associated Discrete Circuit (LC-ADC) method used in the small time-step simulation. Resistive switching allows efficient modelling of power electronics circuits and helps to accurately study higher frequency electromagnetic transient phenomena.

Super step

The superstep feature enables the user to model portions of a large network with a time-step that is larger than the traditional time-step of 50us or 60us. The larger time step must be an integer multiple of the main time step. This means that the components in the super step block only run once every n time steps the main step runs. This is usually useful for control loops which, if convoluted, need more time to compute. The superstep network is solved with a time-step as follows:

$$Superstep\_timestep = N * main\_timestep$$

C.1.2. Concept of Subsystems

The concept of a subsystem is an extremely important one in relation to the RTDS. A subsystem is defined as a portion of a power system model which is mathematically isolated from other portions of the system. A subsystem is linked to other subsystems by travelling wave transmission lines whose travel time is greater than or equal to a time-step. These specific portions of the network are said to be decoupled and may be solved independently and hence in parallel. Subsystems are important because the time required to solve a network grows exponentially with the number of nodes. By splitting one system into two, the total number of calculations is significantly reduced. In addition, the multiple subsystems may be solved in parallel. It is not required to split a system network into subsystems if the network model is within the core node limits. If the node limit is exceeded, the network can be split into two subsystems based on core availability. Depending on chassis/rack availability, the network can be further split into draft pages with multiple subsystems depending on chassis/rack availability. Multiple draft pages require multiple chassis/rack. Each chassis/rack can contain one draft page and two subsystems only.

C.1.3. Time-steps used in the HVDC Network Model

Subsystem 1: The windfarm: Since the windfarms are modelled as an average model, the time-steps the windfarms operate at is the **main time-step:** $60\mu s$.
Subsystem 2: The Offshore DC network contains small time-step calculation blocks or VSC type blocks.

- MMC2 : small time-step running = $3.7\mu s$
- MMC3 : small time-step running = $3.6\mu s$
- VARCDCCB : small time-step running = $2\mu s$

Subsystem 3: The AC network and the DC HUB, this subsystem has a combination of small time-step and substep.

- MMC1 : substep running : **9** times every time-step.
- MMC4 : substep running : **9** times every time-step.
- VARCDCCBh3: small time-step running = $3\mu s$
- VARCDCCB5: small time-step running =$2\mu s$
- VARCDCCB2: small time-step running = $2.5\mu s$

D

Power & Energy Society General Meeting, Conference Paper

Post DC Fault Circulating Current Suppression Control

Rohan Kamat Tarcar, Ajay Shetgaonkar (*Student Member, IEEE*), Marjan Popov (*Fellow, IEEE*), Mart van der Meijden, Wilhelm Winter, Mario Ndreko, Robert Dimitrovski, Matthias Burkhardt, and Aleksandra Lekić (*Senior Member, IEEE*)

***Abstract*—The radial topology of the Multi-terminal High Voltage Direct Current (MTDC) power system is a preferred connection for the gigawatt- renewable power due to its scalability and reliability. However, a radial topology with a metallic return bipolar converter configuration MTDC network possesses technical challenges regarding DC fault current interruption and grid expansion. Furthermore, such HVDC networks are energized in a specific manner, usually involving a separate energizing controller. This paper proposes a design of DC Hubs with direct current circuit breakers (DCCBs) along with a network energization sequence without requiring a separate controller. Additionally, a PI-based controller for post-DC fault circulating current in MTDC's metallic return is proposed. This control operates after DCCB recloses, removing any offset in the metallic cable by regulating the power setpoint in the converters. The proposed control is investigated under a pole-to-ground fault occurrence in the DC Hub. The proposed solution is validated by RSCAD/RTDS$^{@}$ simulation by applying detailed and average equivalent models of turbines, DCCBs and converters. The results of this simulation show a successful suppression of the DC circulating current, which results in a balanced operation of the MMCs in the post fault steady state conditions.**

***Index Terms*—MTDC, Bipolar MMC, Metallic return, Startup Sequence, Current Suppression Control, RTDS, VARC DCCB**

I. Introduction

Modular multilevel converter (MMC) based transmission is preferred for large offshore renewable power generation due to its scalability, controllability and reliability [1]. In recent years, numerous point-to-point (P2P) MMC-based high-power direct current (HVDC) transmission links are either built or planned in Europe. The P2P topology is the simplest HVDC network, but one of the major disadvantages is that adding new terminals to the existing network is not possible without building a new network [2]. To meet European Union (EU) goals, Mesh Offshore Grid (MOG) is a proposed concept in European research projects [3].

Among different MOG topologies, the radial topology is selected because of its improved onshore grid reliability and resiliency [4], along with the better utilization of generation and transmission infrastructures [5]. A bipolar metallic return configuration is proposed for the terminal implementations of this radial topology due to $N-1$ contingency. Furthermore, an offshore Hub is planned at the Bornholm island, CleanStream energy Hub, which would increase system reliability. The design of the offshore Hub is challenging due to its large footprint and costs [6]. Thus, the onshore DC Hub is proposed instead. DC Hub comprises a DC bus bar and a direct current circuit breaker (DCCB). The DCCB protects the MTDC against DC faults by interrupting the faulty interconnection. Over decades of research on DCCB, different DCCB topologies have been proposed. Voltage source converter assisted resonant current (VARC) DCCB is selected in this study due to its fast fault interruption capabilities, low conduction loss, and cost-effectiveness. [7]–[10]. However, the energization of the radial grid with DCCBs is not sufficiently explored. Therefore, this paper proposes a missing solution for the energization and post-fault circulating current suppression.

The start-up sequence proposed in [11], requires a separate control to ensure a safe energization of the networks as the network does not contain DCCBs. The sequence described in [12] involves the insertion of resistors with associated bypass breakers. Implementing the DC-Hub and DCCBs makes it possible to realize an energization sequence without needing a separate black start control. This start-up sequence is addressed in this paper. Furthermore, these start-up sequences apply only to specific scenarios with rigid bipoles or only monopolar configuration of the MMCs in the network or with LCC rather than VSC in the converter stations, in which the zero current or zero voltage modes of start up are used, the latter being in which the DC voltage is initially limited to 0.5 pu till the DC reaches its rated value and, vice versa [13].

Another contribution of this paper is the circulating current suppression on the DC side of the bipolar MMC-based system after a DC fault interruption. The circulating current in MMCs is usually controlled inside the MMCs by applying a circulating current suppression control (CCSC) [14]–[16]. A few more current suppression controllers that use proportional resonant control only work well when the number of submodules is high [17], [18], contrary to the controller discussed in this paper, which is not dependent on the number of submodules. Upon DC fault current interruption in a bipolar metallic configuration, the nominal current flows through the metallic return. Furthermore, after the re-close of the DCCB, a circulating current leaks into the metallic return path of the cable. As a result, there is a power imbalance in the network during the post-fault period. To our knowledge, evidence has yet to be reported in the literature explaining the mentioned phenomena. Hence, the circulating current is generally left uncontrolled [19]. In this paper, the aforementioned circulating current on the DC side is referred to as the residual metallic return current.

This paper discusses a new energization/startup sequence

R. K. Tarcar, A. Shetgaonkar, M. Popov, and A. Lekić are with the Faculty of Electrical Engineering, Mathematics and Computer Science, Delft University of Technology, Delft, The Netherlands (correspondence e-mails: {M.Popov, A.Lekic}@tudelft.nl)

M. vd Meijden is with TenneT TSO B.V., Arhnem, The Netherlands(e-mail: Mart.vander.Meijden@tennet.eu)

W. Winter, M. Ndreko, R. Dimitrovski and M. Burkhardt are with TenneT GmbH, Bayreuth, Germany (e-mails: {Wilhelm.Winter, Mario.Ndreko, Robert.Dimitrovski, Matthiassebastian.Burkhardt}@tennet.eu).

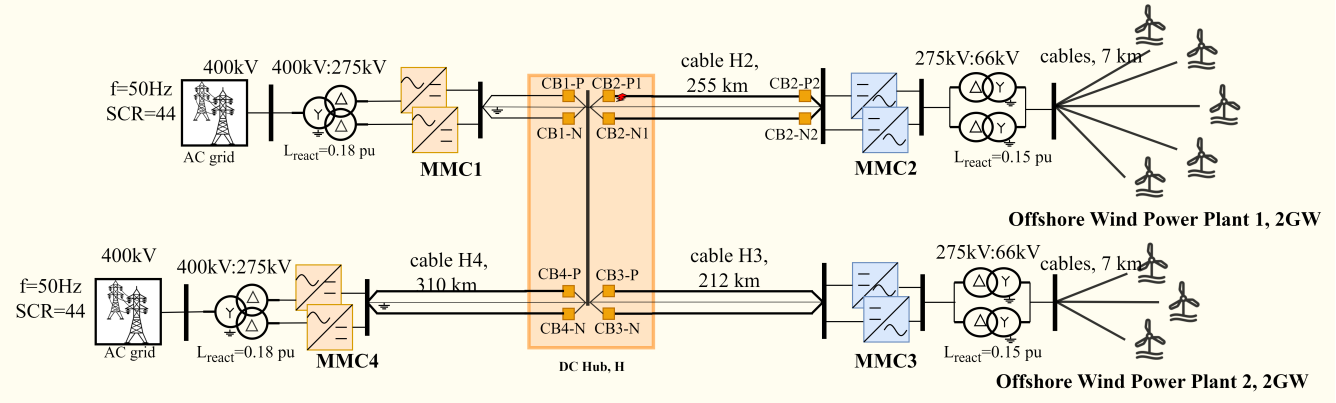

Fig. 1: A four-terminal ±525 kV bipolar half-bridge MMC-based HVDC system with a metallic return, and a DC Hub.

and a DC circulating current suppression controller for the dedicated metallic return. Furthermore, the implementation of a DC Hub and VARC DCCBs makes the use of an energization sequence without a separate startup controller possible, and they are tested for a pole-to-ground (PG) fault condition on a Real Time Digital Simulator (RTDS@). Both the startup sequence and the suppression controller can be easily implemented in bipolar MMC-based HVDC networks with DCCBs, which are installed for the system's protection.

Section II deals with the description of the MTDC network/model. The starting sequence of the network is stated in Section III. The effect of the post-fault circulating current and the mitigation effect of the zero current controller is presented in Section IV. The results are presented and discussed in Section V, and finally, the paper ends with meaningful conclusions presented in Section VI.

II. Network Description

The studied system is an offshore ±525 kV bipolar metallic return four-terminal HVDC network with a DC Hub, as shown in Fig.1. The network studied in Cigre B4.72 was taken as a basis for the development of the studied system [19]. It consists of two onshore stations, an onshore DC Hub, and two offshore stations. The onshore stations are connected to the AC grid, whereas the offshore converter stations are connected to the wind power plants (WPPs). The topology of this network is a radial, with the Hub being the central node. All MMCs (i.e. converter stations) makes use of half-bridge submodules with a bipolar connection. The MMCs denoted as MMC4, the negative pole of MMC1 and the negative pole of MMC2 are modelled as average value models in RSCAD/RTDS (known as type 5). All other MMCs in the network are modelled as GTFPGA-based detailed equivalent RSCAD/RTDS models (known as type 2) [20]. The onshore stations are connected to the Thevenin's equivalent circuit of a strong grid ($SCR = 44$), and the offshore stations are connected to the average value-based wind turbines.

The DC Hub (switchyard) enables installation of VSC-assisted resonant current direct current circuit-breakers (VARC DCCBs) on the cables connecting the Hub to the converter stations. The cable connecting the DC Hub with MMC2 (cable H2) is 255 km long, the cable from the Hub to MMC3 (cable H3) is 212 km long, and the cable joining the Hub with MMC4 (cable H4) is 310 km long. MMC1 is directly connected to the Hub through the DCCBs. The cables are modelled as frequency dependent (phase) model. Furthermore, due to metallic return topology, the cable link consists of 3 cables (i.e., a positive, a negative, and a metallic return cable in one cable connection). The network topology is designed in such a way to have one set of VARC DCCBs on cable H3. There are no DCCBs at the offshore end of the cables due to technical and economic factors. To investigate the impact of offshore DCCB on the network during pre and post-transient disturbance, we placed a DCCB at the end of cable H3 (the end that is far away from the MMC).

The offshore converters are connected to the WPPs by 7 km AC cables. The plant that is connected to MMC2 uses 5 wind turbines, and the other one connected to MMC3 has 3 wind turbines. The onshore capacity of each converter station is 6 GW, whereas that of offshore is 4 GW. The capacity of the wind turbine is 5 MW. However, the total capacity of each WPP is scaled to 2 GW using a scaling transformer to have WPPs with practical capacities. Table I shows additional network specifications. The network is designed to have $N-1$ security as each MMC in the offshore converter station is designed to handle 2 GW of power, ensuring full power flow even during faults in one of the cables connected to the MMCs. The control strategies implemented for each converter stations are listed in Table II.

It should be noted that following assumptions are made during the modelling:

- When the positive pole of MMC is mentioned, it refers to the upper MMC of the bipolar MMC configuration connected to the positive pole of the cable. Similarly, the negative pole of the MMC refers to the lower MMC of the same bipolar configuration, connected to the negative pole of the DC cable.
- When the power is consumed, the sign of active power (P) and reactive power (Q) is positive ($+ve$), and if the power is generated the sign if active power (P) and reactive power (Q) is negative ($-ve$).
- During the startup sequence, the protection protocols in place are temporarily disabled to avoid the spikes in the active power during pole closure. This is caused by the DC control strategy of MMC1.

III. Starting Sequence

The energization of the MTDC requires a startup sequence to ensure that the system will operate nominally [21]. This

TABLE I: Network specifications

Parameter	Onshore	Offshore
Transformer capacity	6 GW	4 GW
Rated grid line-line voltage	400 kV	66 kV
Transformer voltage ratio	400/275 kV	275/66 kV
Transformer leakage reactance	0.18 pu	0.15 pu
Transformer configuration	Yn-D, 1P3W	D-Yn, 3P2W
DC line inductances	80 mH	80 mH
No. of MMC Submodules	240	240
Submodule capacitance	25 mF	16 mF
Converter Inductance	50 mH	50 mH

TABLE II: Control strategy specifications of the converters in the network

Converter	Control mode	Added Description
MMC1	V_{dc}, V_{ac}	$V_{dc,ref} = 525$ kV, $V_{ac,ref} = 400$ kV
MMC2	V_{ac}, f	$V_{ac,ref} = 66$ kV, $f_{ref} = 50$ Hz
MMC3	V_{ac}, f	$V_{ac,ref} = 66$ kV, $f_{ref} = 50$ Hz
MMC4	P, Q	$P_{ref} = 2000$ MW, $Q_{ref} = 0$ MW

sequence is also crucial for the precharging of the MMCs' submodule capacitors [11]. The proposed startup sequence considers the control strategies implemented for the network converter stations and the control strategies' settling times. The sequence proposed is as follows:

- Deblocking of the MMCs in MMC1 and closure of the VARC DCCBs (CB1-P and CB1-N) occurs simultaneously, thereby the DC voltage to ± 525 kV on the terminals. MMC1 sets the reference voltage for the DC Hub and then the Hub charges all the cables.
- Deblocking of the MMCs in MMC2 and closing VARC DCCBs (CB2-P1,2 and CB2-N1,2) is only done after the terminal DC voltage is stabilized at ± 525 kV. This ensures a stable rise in the voltage of MMC2 with minimal disturbances. WPP 1 is then started and deblocked to increase the terminal voltage of MMC2 to 530 kV.
- The energization of MMC3 is the same as that of MMC2, as the control strategy and the power capacities of the MMCs, as well as the WPP connected, are the same.
- Since the MMCs in the MMC4 are controlled in *P,Q* control strategy, the active power of the MMCs is set to consume 2 GW. Therefore, this converter is deblocked, and the VARC DCCBs (CB4-P and CB4-N) are closed, only after the total production of active power is more than 2 GW. Hence, MMC4 is deblocked after the total production is 4 GW. This ensures that MMC4 gets 2 GW of active power, so that the controls can operate as expected.

Table III also lists the events that occur during the startup sequence in chronological order.

Fig. 2 shows the variation of the DC voltage and the active power during the start-up sequence of the network. Since the rated DC voltage of the network is ± 525 kV, the measured DC pole-to-pole voltage is 1050 kV which is used for the per-unit conversion of the DC voltages. Furthermore, according to the CIGRE and ENTSO-E standards, the over- and under-shoot of the voltages should be within the $\pm 10\%$ margin [22], which can be seen as valid in Fig.2. Since the onshore converters (MMC1 and MMC4) are connected to the onshore strong AC grid, the total blocking voltage of the MMCs in the rectifier

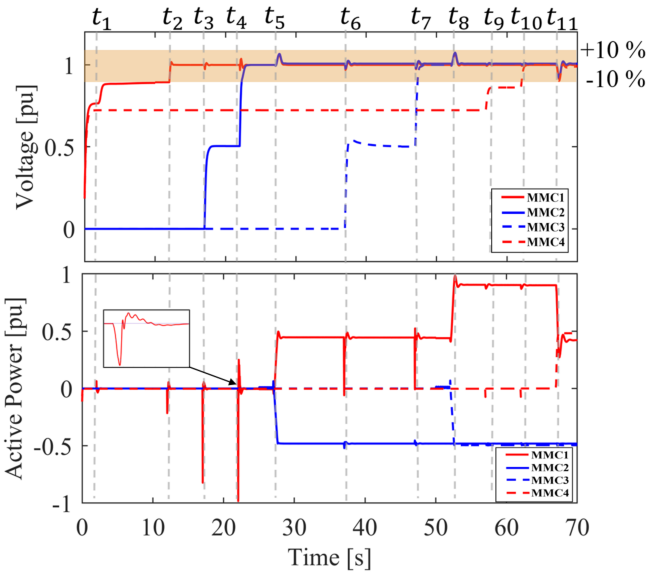

Fig. 2: Behavior of DC voltages and active power during the system's startup.

TABLE III: Sequence of events with their time instants during the startup

Time-step	Events
$\mathbf{t_1}$	MMC1 positive pole is deblocked and CB1-P is closed
$\mathbf{t_2}$	MMC1 negative pole is deblocked and CB1-N is closed
$\mathbf{t_3}$	MMC2 positive pole is deblocked; CB2-P1 and CB2-P2 is closed
$\mathbf{t_4}$	MMC2 negative pole is deblocked; CB2-N1 and CB2-N2 is closed
$\mathbf{t_5}$	Offshore WPP 1 is started and deblocked
$\mathbf{t_6}$	MMC3 positive pole is deblocked and CB3-P is closed
$\mathbf{t_7}$	MMC3 negative pole is deblocked and CB3-N is closed
$\mathbf{t_8}$	Offshore WPP 2 is started and deblocked
$\mathbf{t_9}$	CB4-P is closed
$\mathbf{t_{10}}$	CB4-N is closed
$\mathbf{t_{11}}$	MMC4 is deblocked

mode is about $0.6pu$ (this is before the DCCBs of the onshore converters are closed and the converters are deblocked). This starting sequence also considers the voltage surges that occur when the VARC DCCBs are closed. Therefore, the breakers on the positive pole are closed first, and only after the positive pole voltage has reached its specified value of $+525$ kV, the DCCB on the negative pole is closed.

Additionally, the spikes observed in the active power curve of MMC1 from Fig. 2 are caused by the sudden voltage fluctuation when DCCBs close. Namely, the DC voltage control of MMC1 tries to reach its set point, which causes an unconventional spike in the active power at those time instances. The voltage and active power spikes are observed to be in proportion to the distance of the DC cable, i.e. the longer the cable, the bigger the fluctuation spikes. The final dip of the voltages and the active power at t_{11} is caused by deblocking of the MMC4, which is governed by *P,Q* control.

This unique sequence is only possible because of the presence of VARC DCCBs in the DC Hub, which allows rapid connection and disconnection of the cables in the network.

IV. Post Fault DC Circulating Current Suppression Control

A. Post fault DC circulating current imbalance

The metallic ground return implemented with the bipolar configuration of the MMCs, provides a return path for the current during and after fault current interruption. A temporary PG fault was implemented on the positive pole of the cable H2, at the point of contact between the DC Hub, and the positive pole cable termination. This fault, in reality, could resemble a faulty contact and therefore have real-life inferences. Since this fault is between the DC Hub and MMC2, some major observations were made in MMC2. It was observed that the rapid de-energization and energization of the MMC during and after the fault, and the closure of the DCCB pole led to a residual current in the metallic return. This residual circulating DC current causes an imbalance in the DC currents in the poles of the cables. This imbalance further created a magnitude difference in the DC voltages, and the active and reactive powers of the MMC2 and the power transferred through the cable H2, as seen in Table IV. The metallic return current is also depicted in Fig. 4.

Fig. 4 shows the current through the dedicated metallic return of cable H2. Before the fault is imposed, the current through the metallic return is observed to be 0 kA, which is in line with the nominal operating conditions. At the time instance t_f, the PG fault is imposed and the transient current rushes through the metallic return. After the fault has cleared, the current through the metallic return is around 3 kA, which is according to the expectation since only one pole (negative) is still in operation. All of the planned 2 GW of power flows through this pole. At t_c, when the CB2-P1 and CB2-P2 are closed, another spike in the metallic return current is observed before reaching a steady state value of 0.32 kA. This residual current is responsible for the imbalance caused in the MMC bipolar converters, the power delivered through cable H2, and the currents in cable H2, as seen in Table IV.

B. DC circulating current suppression control

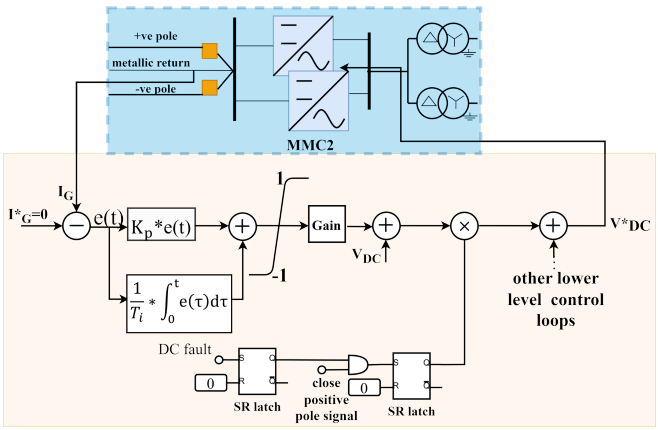

Fig. 3: Block diagram of the zero-current controller.

As a solution for the post-fault metallic return current imbalance, a PI controller was implemented and tuned to counteract the imbalance observed in Fig. 4. Fig. 3, shows the block diagram of the controller. The current from the metallic return is fed into the PI control loop, and the output of this loop is fed to V_{dc}^*, i.e. lower-level control of the MMC. The current from the metallic return is compared against the metallic return reference current I_G^*, which is set to be $0pu$. This facilitated the suppression of metallic return current, resulting in the positive and negative pole DC currents to be nearly equal in magnitude, thereby balancing all the parameters of the bipolar MMC station. The controller is only activated after the fault has been cleared and the DCCBs have been closed after the fault clearance event, as there is no necessity for this controller during the start-up sequence or during the occurrence of a fault. This controller's function is to suppress the residual metallic return current in the cable after the fault. The activation logic is depicted in Fig. 3. For the controller, the integral gain $T_i = 5$ s makes it a slow-type controller, and its proportional gain is $K_p = 1$. The controller is not deactivated as it does not affect the normal operation of the network.

V. Verification of the Proposed Control

As seen in Fig. 4, the controller is added to suppress the residual current in the metallic return. It can be seen that up until time instance $t = t_c$, the current signal with the controller retraces the path of the current without the controller. But, after $t = t_c$, the metallic return current with the controller, is having a steeper slope, and reaches a lower value of current faster than the one without the controller. The zoomed portion of Fig. 4 shows that the second peak of the controlled current (9 A) is much lower than the uncontrolled current (1.2 kA) at the same time instant $t = 13.2$ s. The steady-state amplitude of the metallic return current is found to be 7 A, while the magnitude of the metallic return current without the controller was 320 A. From Fig. 5 and Table IV, it is also observed that

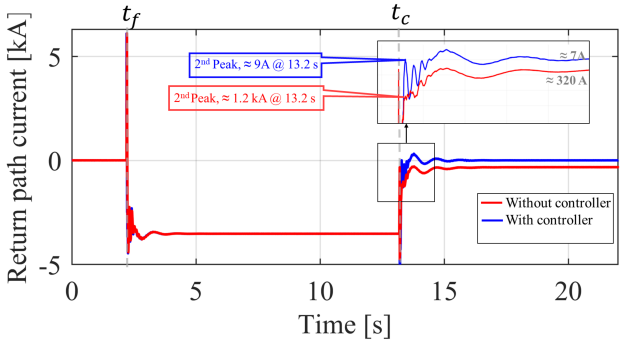

Fig. 4: Metallic return current behaviour with and without the controller.

with the addition of the current suppression controller, the MMC2 operates in the steady-state. Therefore, the imbalance caused in the DC currents of cable H2 previously is removed. Furthermore, this controller was tested under a Positive and Negative PG fault for different locations on cable H2. Likewise, the investigation was extended for a capacitive, inductive, and resistive DC fault. Under these scenarios, the controller suppresses the return path current as it does in the case of a Positive PG fault. Therefore, the return path current plots for these scenarios are similar to Fig. 4.

TABLE IV: Comparison of MMC2's parameters without and with the controller

MMC2	Without controller			With controller		
	Positive pole	Negative pole	Metallic return	Positive pole	Negative pole	Metallic return
DC currents (kA)	1.645	-1.964	**-0.3187**	1.821	-1.814	**- 0.00705**
Power transferred (MW)	871.2	1043	172	960.3	955	5.1
Active Power of MMC (MW)	-1002	-1050	-	-964.4	-960.4	-
Reactive Power of MMC (Mvar)	104.8	-496.8	-	-58.87	-57.74	-
DC voltage (kV)	528.8	-529.5	-	529.1	529.1	-

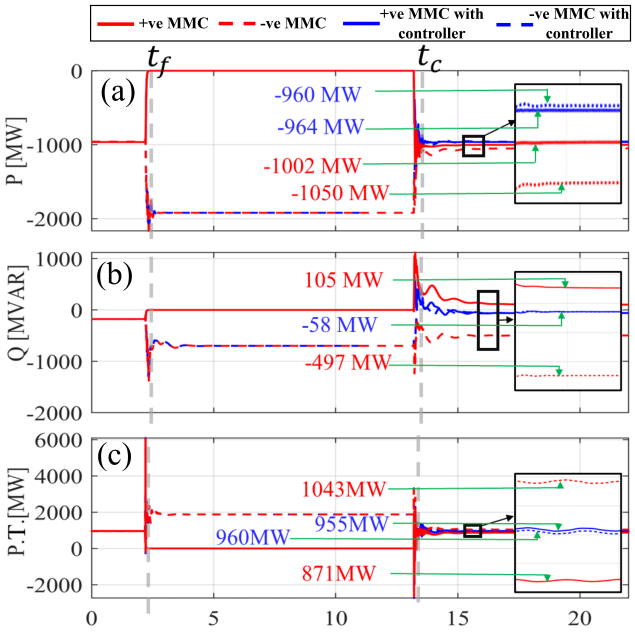

Fig. 5: MMC2 parameters with and without the controller: (a) MMC2 active power, (b) MMC2 reactive power, and (c) power transferred through cable H2.

VI. Conclusion

The paper deals with the development of the startup sequence of the radial MMC-based HVDC network with a metallic return. This sequence is centered around the control strategies implemented for the converters, and the settling times of these strategies rather than devising a separate control for the network energization. This startup sequence is credited to the presence of a DC Hub and the implementation of VARC DCCBs. The paper highlights the mitigation of the DC circulating current observed due to the bipolar configuration. It is established by the controller used for the suppression of the DC circulating current and thereby making the DC currents in the cable equal in magnitude. This controller is a PI controller, that is easy to implement, and provides a viable solution whenever such imbalances in bipolar MMC-based HVDC converters take place. The only trade-off realized during the controller implementations is that the controller can only operate after the fault has been cleared and the circuit breakers are closed. In this work, the current suppression controller is not deactivated as mentioned in IV-B. Therefore, future work will address the deactivation strategy of the current suppression controller.

References

[1] F. Martinez-Rodrigo, S. de Pablo, and L. C. Herrero-de Lucas, "Current Control of a Modular Multilevel Converter for HVDC Applications," *Renewable Energy*, vol. 83, pp. 318–331, 2015.

[2] A. Raza, A. Mustafa, U. Alqasemi, K. Rouzbehi, R. Muzzammel, S. Guobing, and G. Abbas, "HVDC Circuit Breakers: Prospects and Challenges," *Applied Sciences*, vol. 11, no. 11, p. 5047, 2021.

[3] "PROMOTiON D7.4 Economic Framework for a Meshed Offshore Grid," Brochure, 2019. [Online]. Available: https://www.promotion-offshore.net/results/deliverables/

[4] J. P. Pfeifenberger, J. Tsoukalis, and S. A. Newell, "The Benefit and Cost of Preserving the Option to Create a Meshed Offshore Grid for New York," 2021.

[5] T. M. Haileselassie and K. Uhlen, "Power System Security in a Meshed North Sea HVDC Grid," *Proceedings of the IEEE*, vol. 101, no. 4, pp. 978–990, 2013.

[6] J. N. M. Task-12.3, Task lead-TenneT TSO B.V., "PROMOTiON d12.4 Final Deployment Plan," Brochure, 2020. [Online]. Available: https://www.promotion-offshore.net/results/deliverables/

[7] S. S. Mirhosseini, S. Liu, J. C. Muro, Z. Liu, S. Jamali, and M. Popov, "Modeling a Voltage Source Converter Assisted Resonant Current DC Breaker for Real Time Studies," *International Journal of Electrical Power & Energy Systems*, vol. 117, p. 105678, 2020.

[8] S. Liu, A. Shetgaonkar, and M. Popov, "Coordinative Performance of HVDC Circuit Breakers in MTDC Grids," in *2020 IEEE Power & Energy Society General Meeting (PESGM)*. IEEE, 2020, pp. 1–5.

[9] S. Liu, M. Popov, S. S. Mirhosseini, S. Nee, T. Modeer, L. Ängquist, N. Belda, K. Koreman, and M. A. M. M. van der Meijden, "Modeling, Experimental Validation, and Application of VARC HVDC Circuit Breakers," *IEEE Transactions on Power Delivery*, vol. 35, no. 3, pp. 1515–1526, 2020.

[10] A. Shetgaonkar, S. Liu, and M. Popov, "Comparative Analysis of a Detailed and an Average VARC DCCB model in MTDC Systems," in *2022 IEEE Power & Energy Society General Meeting (PESGM)*, 2022, pp. 1–5.

[11] P. Wang, X.-P. Zhang, P. F. Coventry, and R. Zhang, "Start-up Control of an Offshore Integrated MMC Multi-Terminal HVDC System with reduced DC Voltage," *IEEE Transactions on Power Systems*, vol. 31, no. 4, pp. 2740–2751, 2015.

[12] L. Cai, U. Karaagac, and J. Mahseredjian, "Simulation of Startup Sequence of an Offshore Wind Farm with MMC-HVDC Grid Connection," *IEEE Transactions on Power Delivery*, vol. 32, no. 2, pp. 638–646, 2017.

[13] X. Li, C. Liu, and Y. Lou, "Start-up and recovery method with LCC-HVDC systems participation during ac/dc system black-starts," *IET Generation, Transmission & Distribution*, vol. 14, no. 3, pp. 362–367, 2020.

[14] F. Deng, Q. Heng, C. Liu, Y. Lyu, Q. Wang, D. Liu, and R. Zhu, "Circulating Current Suppression for MMC-HVDC Systems with Asymmetric Arm Impedance," *CSEE Journal of Power and Energy Systems*, vol. 7, no. 3, pp. 530–540, 2020.

[15] J. Wang, J. Liang, C. Wang, and D. Xiaoming, "Circulating Current Suppression for MMC-HVDC under Unbalanced Grid Conditions," *IEEE Transactions on Industry Applications*, vol. 53, no. 4, pp. 1–1, 03 2017.

[16] A. Shetgaonkar, A. Lekić, J. L. Rueda Torres, and P. Palensky, "Microsecond Enhanced Indirect Model Predictive Control for Dynamic Power Management in MMC Units," *Energies*, vol. 14, no. 11, 2021.

[17] H. Zhang, H. R. Wickramasinghe, L. Jing, J. Li, J. Pou, and G. Konstantinou, "Circulating Current Control scheme of Modular Multilevel Converters supplying passive networks under Unbalanced Load conditions," *Electric Power Systems Research*, vol. 171, pp. 36–46, 2019.

[18] M. Zhang, Y. Shen, H. Sun, and R. Guo, "MMC-HVDC CirculatingCurrent Suppression method based on improvedProportional Resonance control," *Energy Reports*, vol. 6, pp. 863–871, 2020.

[19] W. B4.72, "DC Grid Benchmark Models for System Studies," Brochure, 2020.

[20] A. Shetgaonkar, L. Liu, A. Lekić, M. Popov, and P. Palensky, "Model Predictive Control and Protection of MMC-based MTDC Power Systems," *International Journal of Electrical Power & Energy Systems*, vol. 146, p. 108710, 2023.

[21] Y. Huang, Y. Ji, Y. Lu, and W. Huang, "Research on Startup Circuit Parameter Selection and Startup Control Strategy for Multi-Terminal VSC HVDC System," pp. 1–7, 2019.

[22] ENTSO-E, "HVDC Links in System Operators," Technical Paper, 2019.